

Exploring how entangled photon correlations can enhance spectroscopy

Thesis by
Bryce Patrick Hickam

In Partial Fulfillment of the Requirements for the
Degree of
Doctor of Philosophy

The logo for the California Institute of Technology (Caltech), featuring the word "Caltech" in a bold, orange, sans-serif font.

CALIFORNIA INSTITUTE OF TECHNOLOGY
Pasadena, California

2024
Defended August 25, 2023

© 2024

Bryce Patrick Hickam
ORCID: 0000-0003-2120-4769

All rights reserved

*"There must be some way out of here"
Said the joker to the thief
"There's too much confusion
I can't get no relief"*

Bob Dylan

ACKNOWLEDGEMENTS

This work would not be possible without the support of a network of friends, family, and acquaintances that have helped me grow and to whom I am deeply appreciative. The following notes contain those individuals who deserve special recognition.

First, I am grateful to my advisor, Scott Cushing, for his mentorship and support over the course of my PhD career. Scott's enthusiasm for science and instrument building is unparalleled and he constantly inspired me and encouraged me to be a better scientist and thinker. His positive, can-do attitude was consistent through both the highs and lows of research. I greatly appreciated the opportunity and freedom to try new things in lab and pursue my own intellectual curiosities.

To the members of my thesis committee, Professors Ryan Hadt, Kim See, and Geoff Blake, thank you for the advice and feedback throughout the years.

My scientific journey owes much to my undergraduate mentors, who introduced me to scientific research and served as excellent role models in my teaching experiences. Professors Linda Lasater, Jeff Cannon, and Eileen Spain, as well as the rest of the Occidental College Chemistry Department, nurtured my early interest in Chemistry. I would also like to thank Professor Geraldine Richmond at the University of Oregon, and her former graduate student, Dr. Andrew Carpenter, for piquing my interest in spectroscopy.

The past and present members of the Cushing group deserve a heartfelt thank you. To my entangled photon subgroup colleagues with whom I have worked closely — Manni He, Nathan Harper, Emily Hwang, Dr. Szilard Szoke — thank you for your camaraderie and for pushing me to be the scientist that I am today. I am especially grateful to Manni He, Jonathan Michelsen, Dr. Isabel Klein, and Danika Nimlos for being invaluable companions as we built Scott's lab together from scratch. I have also greatly appreciated that our friendship has extended outside of lab.

I would also like to thank the Caltech CCE staff that ensure the department runs smoothly on a day-to-day basis. Joe Drew and Alison Ross have been excellent resources. Thanks to Elisha Okawa for ensuring the Cushing group can function day-to-day.

Thank you to my friends at Caltech and in Pasadena who have enriched my life both inside and outside of science, including Griffin Mead, Noah Krim, Kshitij Sadasivan,

Mayukh Sen, Ricky Novaes, Aiva Ievins, Mark Wronkiewicz, Natalie Hills, Gracie Zhang, Anna Overholts, Ross Barber, William Hight, Danika Nimlos, Sadie Dutton, Hamilton Evans. I will remember get-togethers, adventures, barbeques, and game nights with these folks fondly. Griffin, Anna, Kshitij, and Ross have been great climbing partners that have made exploring indoor and outdoor crags a thrill. Aiva and Mark were great neighbors and are even better friends. Special shout out to their dog, Moxie, for her relationship with our dogs Chula and later Shyla. Aubri Juhasz, Brenna Forristall, Julien Reiman, and Linda Gordon also deserve a big thanks for their friendship and for welcoming me into their lives so heartily.

Thanks to my family who have unwaveringly supported me throughout my life, including my parents, Robert Hickam and Leslie Foster, and my sister Clarissa Hickam. My scientific career owes much to my grandfather, Dr. James Foster, who nurtured my passion for science and math from a young age and is partly the inspiration for my pursuit of chemistry at Oxy and Caltech. Thank you also to my relatives, Guy, Julie, Kirk, and Cindy Foster, as well as my cousins, Sarah, Eden, Grace, and Lily Foster, for our adventures in Tahoe and beyond.

Thank you also to the Kleins — Jason, Carrie, Max, and Keelin — for welcoming me so readily into their family and for their support. I have greatly enjoyed exploring North Carolina, Colorado, San Antonio, and Argentina, among other places, with you all. Here's to more good times and good food!

Finally and most importantly, I would like to acknowledge my partner, Dr. Isabel Klein. Isabel's companionship and love have been steadfast and abundant through good times and bad. Isabel, your presence has made my world much happier and richer. I am excited for our life together and future adventures in all corners of the globe.

ABSTRACT

Quantum light sources consisting of highly correlated or "entangled" photon pairs are increasingly becoming popular alternatives to classical light sources to perform microscopy and spectroscopy. Entangled photon pairs can replicate and enhance spectroscopic signals and have practical advantages compared to the pulsed laser systems that are typically utilized to perform these measurements. For instance, entangled photons are inherently low-flux, enabling measurements to be performed without undesired photoeffects, such as sample heating and degradation or nonideal photoinduced sample behavior. In addition, entangled photon sources can be generated and manipulated on much smaller physical footprints than state-of-the-art pulsed laser systems with comparable frequency bandwidths and time resolutions. Together, these capabilities could allow for the development of spectroscopic instruments that do not rely on bulky, expensive pulsed laser systems that necessitate teams of specialists to maintain. In turn, this instrument development could enable more widespread access to exotic forms of atomic and material characterization.

Despite a growing body of theoretical work, the field of experimental entangled photon spectroscopy is still nascent and entangled light-matter interactions have yet to be fully characterized in laboratory settings. Here, we investigate entangled photon light-matter interactions towards the goal of developing entangled spectroscopic techniques. A broadband entangled photon source with femtosecond coherence times is designed and characterized to perform these measurements. Using this source and an entangled photon spectrometer, characterization of the entangled photon enhancement to two-photon absorption are attempted by in studies of two different molecular dyes, Rhodamine 6G and zinc tetraphenylporphyrin. The entangled photon two-photon absorption enhancement is determined to be below previously reported values due to the presence of single photon scattering signals. Finally, entangled photons are utilized to replicate fluorescence lifetime measurements using a continuous wave pump laser and the temporal correlations inherent to entangled photon pairs. As the first experimental demonstration of this technique, the fluorescence lifetimes of indocyanine green in three solvent systems are measured.

PUBLISHED CONTENT AND CONTRIBUTIONS

1. Harper, N., Hickam, B. P., He, M. & Cushing, S. K. Entangled Photon Correlations Allow a Continuous-Wave Laser Diode to Measure Single-Photon, Time-Resolved Fluorescence. *The Journal of Physical Chemistry Letters*, 5805–5811. <https://doi.org/10.1021/acs.jpcllett.3c01266> (2023) (June 2023).
B.P.H. designed and constructed the instrument, collected and analyzed data, and wrote the manuscript.
2. Hickam, B. P., He, M., Harper, N., Szoke, S. & Cushing, S. K. Single-Photon Scattering Can Account for the Discrepancies among Entangled Two-Photon Measurement Techniques. *The Journal of Physical Chemistry Letters*, 4934–4940. <https://pubs.acs.org/doi/10.1021/acs.jpcllett.2c00865> (2022) (May 2022).
B.P.H. designed and constructed the instrument, collected and analyzed data, and wrote the manuscript.
3. Szoke, S., He, M., Hickam, B. P. & Cushing, S. K. Designing high-power, octave spanning entangled photon sources for quantum spectroscopy. *The Journal of Chemical Physics* **154**, 244201. <https://aip.scitation.org/doi/10.1063/5.0053688> (2021) (June 2021).
B.P.H. designed and constructed the experimental configuration for characterization measurements, collected and analyzed data, and helped prepare the manuscript.
4. Szoke, S., Liu, H., Hickam, B. P., He, M. & Cushing, S. K. Entangled light–matter interactions and spectroscopy. *Journal of Materials Chemistry C* **8**, 10732–10741. <http://pubs.rsc.org/en/content/articlelanding/2020/tc/d0tc02300k> (2020) (Aug. 2020).
B.P.H. helped prepare the manuscript.

TABLE OF CONTENTS

Acknowledgements	iv
Abstract	vi
Published Content and Contributions	vii
Table of Contents	vii
List of Illustrations	x
List of Tables	xiii
Nomenclature	xiv
Chapter I: Introduction	1
Chapter II: Entangled light-matter interactions and spectroscopy	5
Abstract	6
2.1 Introduction	7
2.2 Hong–Ou–Mandel interference and biphotons	8
2.3 Generation and detection of entangled photons	11
2.4 Spectroscopy with one entangled photon	14
2.5 Spectroscopy with two or more entangled photons	15
2.6 Current directions in entangled light-matter interactions	18
2.7 New opportunities in materials science	21
2.8 Outlook	23
Chapter III: Designing High-Power, Octave Spanning Entangled Photon Sources for Quantum Spectroscopy	36
Abstract	37
3.1 Introduction	38
3.2 Theory	40
3.3 Experiment and results	49
3.4 Conclusion	57
Chapter IV: Single Photon Scattering Can Account for the Discrepancies Between Entangled Two-Photon Measurement Techniques	64
Abstract	65
4.1 Introduction	66
4.2 Experimental overview	68
4.3 Results: Fourth-order interference measurements	70
4.4 Results: Wavelength-resolved measurements of Rhodamine 6G	72
4.5 Results: Measured entangled photon interaction cross sections	73
4.6 Conclusion	74
4.7 Experimental details	75
Chapter V: Entangled Photon Correlations Allow a Continuous-Wave Laser Diode to Measure Single Photon, Time-Resolved Fluorescence	83
Abstract	84
5.1 Introduction	85

5.2	Experimental overview	87
5.3	Results: TCSPC histograms and lifetimes	91
5.4	Results: Measurement statistics	92
5.5	Conclusion	94
5.6	Experimental details	95
Chapter VI: Conclusions and future directions		102
Appendix A: Supplementary Information for Designing High-Power, Octave Spanning Entangled Photon Sources for Quantum Spectroscopy		
A.1	CLT refractive indices	106
A.2	Quasi-phase-matching	106
A.3	Phase-matching amplitude	108
A.4	Entanglement and purity	109
A.5	Broadband HOM interference	110
Appendix B: Supplementary Information for Single Photon Scattering Can Account for the Discrepancies Between Entangled Two-Photon Measure- ment Techniques		
B.1	Linear absorption measurement	117
B.2	Interferogram simulation	118
B.3	Broadband fourth-order interference	120
B.4	Entangled photon spectra	124
B.5	Absorption spectra of studied compounds	125
B.6	Degenerate entangled photons	126
B.7	Zinc tetraphenylporphyrin	127
B.8	Destruction of entanglement with a quarter-wave plate	128
B.9	Absorbed photon rate vs. input photon rate	129
Appendix C: Supplementary Information for Entangled Photon Correlations Allow a Continuous-Wave Laser Diode to Measure Single Photon, Time- Resolved Fluorescence		
C.1	Select optical properties of ICG	131
C.2	Confirmation of fluorescence	131
C.3	Experimental stability and background	132
C.4	Lifetime fits with residuals	133
C.5	Fitting algorithm	134
Appendix D: Entangled two-photon Michelson interferometer alignment guide		
D.1	Fiber coupling guide	140

LIST OF ILLUSTRATIONS

<i>Number</i>	<i>Page</i>
1.1 Polarization entangled photon pairs generated via Type-II SPDC . . .	2
2.1 Hong–Ou–Mandel interference with photons	9
2.2 Periodically poling and experimental demonstration of broadband entangled photon pairs	13
2.3 Measuring infrared absorption with visible photons	15
2.4 Simulated two-dimensional fluorescence spectra for electronically coupled molecular dimer with classical and entangled light	16
2.5 Spectral resolution in entangled two-photon spectroscopy	18
2.6 The linearity of various entangled two-photon processes as a function of power	19
3.1 Quasi-phase-matching for SPDC	41
3.2 Simulated SPDC emission spectra with transition from degenerate to non-degenerate down conversion	43
3.3 SPDC emission angles from ppCLT at various temperatures	44
3.4 Graphic depiction of chirped periodic crystal poling	45
3.5 Simulated SPDC emission bandwidth	46
3.6 Buildup of SPDC spectrum over chip length	47
3.7 Simulated and measured SPDC spectra for chirped and unchirped gratings	51
3.8 Entangled photon pair Michelson interferometer	52
3.9 Simulated and measured Michelson plots for varying bandwidths of SPDC	54
3.10 Images of SPDC in near and far fields	57
4.1 Reported experimental ETPA cross sections vs. classical TPA cross sections from ETPA studies conducted up to January 2022	67
4.2 Experimental setup used to measure the proposed ETPA and 90- degree signal	70
4.3 Transmitted fourth-order interference and 90-degree signals	71
4.4 Wavelength-resolved 90-degree signals from 5mM R6G	73
4.5 R6G ETPA cross section measured using the field-standard method of attenuating flux	74

5.1	Entangled photon FLIM experimental configuration	88
5.2	Indocyanine green absorption/emission spectra, entangled photon ICG fluorescence emission, and IRF	89
5.3	IRF, TCSPC histogram, and fit of histogram for ICG in three solvents measured with entangled photon pairs	92
5.4	Standard dev. of fit lifetime vs. integration time for ICG/DMSO	93
A.1	Congruent lithium tantalate refractive indices for ordinary and extraordinary polarizations at two different temperatures.	106
A.2	Calculated poling period for 406nm-812nm at 133°C — CLT.	107
A.3	Phase matching amplitude contour plot for a 20 mm long ppCLT grating with a 9.5 μm poling period at 133°C	108
A.4	SPDC emission spectrum as a function of the pump bandwidth	111
A.5	Schematics of a two-photon Michelson or Mach-Zehnder interferometer.	112
A.6	Simulated Michelson interference for Gaussian SPDC spectrum with 10 nm bandpass filter centered at 812 nm	113
A.7	Simulated Michelson interference for Gaussian SPDC spectrum with 125 nm bandpass filter centered at 812 nm	113
A.8	Measured collinear broadband two-photon interference when the arms of the Michelson interferometer are perpendicularly polarized	114
A.9	Measured collinear narrowband two-photon interference when the arms of the Michelson interferometer are perpendicularly polarized	114
A.10	Measured SPAD counts and coincidences vs. pump power for collinear broadband SPDC	115
A.11	Measured SPAD counts and coincidences vs. pump power for collinear narrowband SPDC	116
B.1	Fourier transform of measured entangled photon interferograms	119
B.2	Simulated and experimental photon counts for non-degenerate entangled photons in a two-photon Michelson interferometer	120
B.3	Schematics of a two-photon Michelson or Mach-Zehnder interferometer	121
B.4	Entangled photon spectra at two ppLT crystal temperatures	124
B.5	Absorption spectra of ZnTPP and R6G	125
B.6	Experimental photon counts for degenerate entangled photons in a two-photon Michelson interferometer	126
B.7	90-degree signal from zinc tetraphenylporphyrin	127
B.8	Destruction of entanglement with a quarter-wave plate	128

B.9	Absorbed entangled photon rate vs input entangled photon rate for R6G/water on a log scale	129
C.1	Coincidence histograms of pure methanol and methanol/indocyanine solutions	132
C.2	Count rates vs. experiment time	133
C.3	Coincidence histograms of ICG in solvents on a log scale	134
C.4	Weighted residuals from histogram lifetime fits	134
D.1	Experimental data from a coarse scan of entangled photons in a Michelson interferometer	140

LIST OF TABLES

<i>Number</i>	<i>Page</i>
3.1 Chip parameters	49
3.2 Coherence times of different configurations and bandwidths of SPDC	55
5.1 Summary of relevant experimental timescales from instrument pa- rameters	90
5.2 Fluorescence lifetimes for ICG from literature and as measured with entangled photon pairs	92
C.1 Select optical properties of ICG in methanol, ethanol, and DMSO . .	131
C.2 Count rate means and variances demonstrating nearly shot-noise lim- ited statistics.	133

NOMENCLATURE

BBO. Beta barium borate.

CLT. Congruent lithium tantalate.

CW. Continuous wavelength.

EMICCD. Electron multiplying intensified charge-coupled device.

ETPA. Entangled two-photon absorption.

FLIM. Fluorescence lifetime imaging microscopy.

ICG. Indocyanine green.

IR. Infrared.

KTP. Potassium titanyl phosphate.

MgO. Magnesium oxide.

ppLT. periodically poled lithium tantalate.

R6G. Rhodamine 6G.

SPAD. Single photon avalanche photodiode.

SPDC. Spontaneous parametric down-conversion.

TCSPC. Time-correlated single-photon-counting.

UV. Ultraviolet.

ZnTPP. Zinc tetraphenylporphyrin.

Chapter 1

INTRODUCTION

The rich dynamics of atoms and molecules have long piqued scientific curiosity. From the fusion of heavy elements in the sun to an icy glass of juice that provides a bit of respite from that radiation, these dynamics are responsible for the physical manifestation of the natural world around us. A powerful tool to characterize atoms and molecules is optical spectroscopy, whereby the response of an atomic or molecular system to an electromagnetic field is measured and monitored. A wide range of spectroscopic techniques have been developed to understand the physical behaviors of matter, from the motions of elemental nuclei to the surrounding complex electronic landscapes. Developing new techniques, as well as enhancing existing ones, represents a significant thrust within the field of physical chemistry.

Underlying electromagnetic radiation and atomic and molecular systems are the mechanics of particles. The properties of these quantum objects can be tailored and manipulated to display some truly astonishing behaviors compared to the classical dynamics of massive bodies that we interact with in our daily lives. One such example is the ability of particles to be entangled with each other. Entanglement refers to the phenomenon in which the state of a subsystem of a body of particles cannot simply be described as a product of the independent particle states in that subsystem [1]. Instead, the particles in the subsystem are said to be in an entangled state, or a "superposition" of multiple possible states. Famously, Einstein labeled entanglement as "spooky action at a distance."

The concept of photon entanglement can be tricky to conceptualize in a practical setting. Perhaps one of the more intuitive demonstrations of photon entanglement is that of the polarization entangled photons that can be generated by spontaneous parametric down conversion of a single photon in a nonlinear crystal. Here, the single pump photon interacts with a vacuum state to generate a pair of photons of lower energy. The photons are emitted as cones with opposite polarizations, as shown in Fig. 1.1. At almost every point along each of the cones, the polarization state of each photon is known: either the photons are vertically (V) or horizontally (H) polarized. However, the oppositely-polarized cones overlap at two points. Within the region of overlap, a randomly selected photon can either be vertically or

horizontally polarized. The same is true of its partner photon in the other region of overlap. However, if the polarization state of one of the photons is measured, the polarization state of its partner can also be immediately determined. In other words, the photon pairs within these regions of cone overlap exist in a "superposition" of polarization states, as described by the mathematical formalism:

$$|\Psi\rangle = \frac{1}{\sqrt{2}}(|V_A H_B\rangle + |V_B H_A\rangle) \quad (1.1)$$

where A and B are the photons within an entangled pair and H and V are their respective polarizations. Photon pairs can be entangled in other degrees of freedom, including momentum [2], energy/time [3], angular momentum [4], as well as multiple combinations of these degrees of freedom [5].

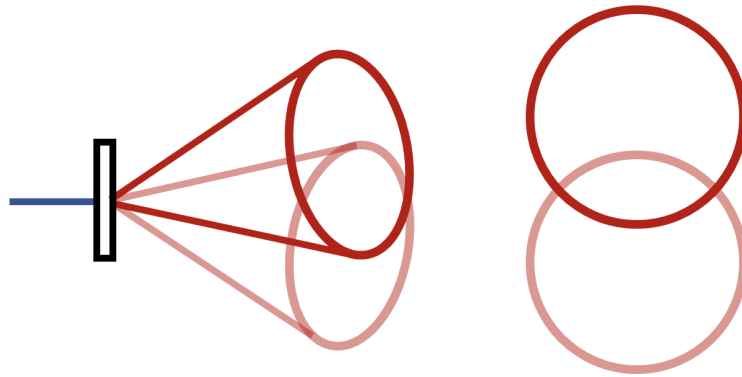


Figure 1.1: Schematic of polarization entangled photon pairs generated by SPDC. Oppositely polarized photons (represented by the dark and light red circles) are generated and emitted as cones. At the points where the cones overlap (right), pairs are entangled in polarization state because it is unknown from which cone they originate.

Typically, spectroscopic techniques utilize the high flux, coherent electromagnetic radiation that is generated by laser sources in order to probe and measure material systems. Recently, entangled photon pairs have attracted research attention within the spectroscopic community due to their enhanced capabilities and practicality relative to classical laser sources. For instance, entangled photon pairs can enhance the signal-to-noise ratio in spectroscopy beyond the shot noise limit [6, 7]. In addition, entangled photons are predicted to enhance nonlinear spectroscopies in which two or more photons interact with a sample. This curious result arises from the single-photon-like behavior of the entangled pair in light-matter interactions,

and has significant implications for spatially and temporally-resolved measurements [8, 9]. From a practical standpoint, entangled photon pairs can be generated and manipulated on much smaller scales and with lower power requirements than the laser systems that are currently used to perform spectroscopic measurements. Entangled photon pairs can be generated using a low-power, inexpensive laser diode and manipulated on a nanophotonic platform [10]. In theory, this miniaturization could enable the development of handheld entangled photon spectrometers and in turn, expand the availability and accessibility of complex spectroscopic techniques to broader populations.

While significant progress has been made in establishing the theoretical background of entangled photon interactions, experimental characterization of entangled light-matter interactions are currently lacking. Experimental demonstrations of these interactions represent a significant step in benchmarking the capabilities of entangled photons relative to classical light sources towards developing quantum spectroscopic instruments and techniques. To this end, this thesis presents progress in characterizing entangled light-matter interactions with a broadband entangled photon source. Chapter 2 provides an overview and perspective on utilizing entangled photon pairs in spectroscopy and elaborates on the fundamental underpinnings of entangled photon behavior. This chapter also contains a discussion of several implementations and flavors of entangled photon spectroscopy as well as outlooks for studies in chemistry and materials science. Chapter 3 presents the design and experimental characterization of the broadband entangled photon source based on a periodically poled crystal that is utilized to perform spectroscopic measurements. Chapter 4 describes attempts to measure the order-of-magnitude enhancement that entangled photon pairs are predicted to provide to the two-photon absorption process and provides an explanation for current discrepancies within the field. This work deploys an entangled photon spectrometer that is capable of monitoring and manipulating the entangled state of the photon pairs during the proposed two-photon absorption event, representing a significant development within the field. Chapter 5 highlights the ability of entangled photon pairs to replicate time-correlated single-photon counting experiments, enabling the measurement of molecular fluorescence lifetimes with a continuous wave laser.

References

1. Horodecki, R., Horodecki, P., Horodecki, M. & Horodecki, K. Quantum entanglement. *Reviews of Modern Physics* **81**, 865–942. <https://link.aps.org/doi/10.1103/RevModPhys.81.865> (2018) (June 2009).
2. Howell, J. C., Bennink, R. S., Bentley, S. J. & Boyd, R. W. Realization of the Einstein-Podolsky-Rosen Paradox Using Momentum- and Position-Entangled Photons from Spontaneous Parametric Down Conversion. *Physical Review Letters* **92**, 210403. <https://link.aps.org/doi/10.1103/PhysRevLett.92.210403> (2019) (May 2004).
3. MacLean, J.-P. W., Donohue, J. M. & Resch, K. J. Direct Characterization of Ultrafast Energy-Time Entangled Photon Pairs. *Physical Review Letters* **120**, 053601. <https://link.aps.org/doi/10.1103/PhysRevLett.120.053601> (2023) (Jan. 2018).
4. Krenn, M., Malik, M., Erhard, M. & Zeilinger, A. Orbital angular momentum of photons and the entanglement of Laguerre–Gaussian modes. *Philosophical Transactions of the Royal Society A: Mathematical, Physical and Engineering Sciences* **375**, 20150442. <https://royalsocietypublishing.org/doi/10.1098/rsta.2015.0442> (2022) (Feb. 2017).
5. Kwiat, P. G. Hyper-entangled states. *Journal of Modern Optics* **44**, 2173–2184. <https://www.tandfonline.com/doi/abs/10.1080/09500349708231877> (2020) (Nov. 1997).
6. Xiao, M., Wu, L.-A. & Kimble, H. J. Precision measurement beyond the shot-noise limit. *Physical Review Letters* **59**, 278–281. <https://link.aps.org/doi/10.1103/PhysRevLett.59.278> (2023) (July 1987).
7. Brida, G., Genovese, M. & Ruo Berchera, I. Experimental realization of sub-shot-noise quantum imaging. *Nature Photonics* **4**, 227–230. <https://www.nature.com/articles/nphoton.2010.29> (2020) (Apr. 2010).
8. Javanainen, J. & Gould, P. L. Linear intensity dependence of a two-photon transition rate. *Physical Review A* **41**, 5088–5091. <https://link.aps.org/doi/10.1103/PhysRevA.41.5088> (2019) (May 1990).
9. Dayan, B. Theory of two-photon interactions with broadband down-converted light and entangled photons. *Physical Review A* **76**, 043813. <https://link.aps.org/doi/10.1103/PhysRevA.76.043813> (2020) (Oct. 2007).
10. Tanzilli, S. *et al.* On the genesis and evolution of Integrated Quantum Optics. *Laser & Photonics Reviews* **6**, 115–143. <https://onlinelibrary.wiley.com/doi/abs/10.1002/lpor.201100010> (2020) (2012).

*Chapter 2*ENTANGLED LIGHT-MATTER INTERACTIONS AND
SPECTROSCOPY

ABSTRACT

Entangled photons exhibit non-classical light-matter interactions that create new opportunities in materials and molecular science. For example, in entangled two-photon absorption, the intensity-dependence scales linearly as if only one photon was present. The entangled two-photon absorption cross section approaches but does not match the one-photon absorption cross section. The entangled two-photon cross section also does not follow classical two-photon molecular design motifs. Questions such as these seed the rich but nascent field of entangled light-matter interactions. In this perspective, we use the experimental developments in entangled photon spectroscopy to outline the current status of the field. Now that the fundamental tools are outlined, it is time to start the exploration of how materials, molecules, and devices can control or utilize interactions with entangled photons.

Most of this chapter has been adapted with permission from:

Szoke, S. *et al.* Entangled light-matter interactions and spectroscopy. *Journal of Materials Chemistry C* **8**. Publisher: The Royal Society of Chemistry, 10732–10741. ISSN: 2050-7534. <http://pubs.rsc.org/en/content/articlelanding/2020/tc/d0tc02300k> (2020) (Aug. 2020).

2.1 Introduction

Entanglement is arguably one of the most nonintuitive and fascinating phenomena in the quantum world. Entanglement refers to a many-body quantum state that cannot be decomposed into the product of each individual particle's state in the system [1]. Entangled states can be generated and measured in systems of particles including photons, electrons, and atoms. When a subset of particles in an entangled system interact with external stimuli, the many-body wavefunction of the whole system undergoes decoherence. This decoherence and the associated wavefunction collapse lie at the foundation of many technologies utilizing entanglement as a resource, such as quantum computation, communication, and information sciences [2].

In addition to these technologies, an emerging trend is to explore how entangled light-matter interactions differ from classical interactions. For example, entangled photons lead to two-photon absorption and sum frequency processes that scale linearly as if they are one-photon processes [3–9]. Two-photon experiments should therefore be possible at over a million times lower fluxes than classical experiments. Theoretical predictions suggest the same will be true for three and higher photon processes, converting nonlinear optical processes into linear processes [10]. Entangled photons have also been proposed for the excitation and control of excited state superpositions for qubits and molecular polaritons [11–13]. However, the origin of entangled light-matter interactions and the structural motifs in material and molecular design remain largely unexplored.

The exploration of entangled light-matter interactions currently resides in spectroscopic studies [14]. The central idea is to use the non-classical interference patterns between entangled photon pairs to measure femtosecond and longer processes. Intriguingly, such measurements can be performed using only few-photon fluxes, allowing access to new intensity scalings and quantum phenomena [14]. Entangled photon spectroscopy also offers new possibilities when applied to more classical phenomena. For example, entangled photons can break classical noise limits [15–19] and are predicted to break Fourier reciprocal spectral and temporal precisions [20–23]. A 500 nm bandwidth of entangled biphoton pairs compressed to a few femtoseconds is predicted to only interact at the wavelength and linewidth specified by the input pump laser, usually <1 MHz for a modern Ti:Sapphire oscillator. A narrow excited state distribution can therefore be created with high temporal resolution, potentially allowing new forms of quantum control [21].

At its heart, entangled photon spectroscopy relies on measuring changes in the quantum correlations of photons. The ability of entangled photons to couple, or not, with multi-particle excitations in materials is an intriguing question, both spectroscopically and from an application point of view. Entanglement has been proposed as fundamental to electron–electron and electron–phonon interactions in processes ranging from many-body correlations to singlet–triplet splitting [24–26]. In addition to the linearization of nonlinear interactions, we believe the potential for quantum correlated photons to create or interact with correlations in materials is why entangled light–matter interactions deserve further investigation in this field.

This chapter will provide a perspective on the current status of entangled light–matter interactions. Spectroscopic developments are used to outline the broader questions of how materials and molecules interact with entangled photons. Experimental exploration to date is limited to a few materials systems, partially due to the nascent development of these spectroscopic techniques. For example, entangled two-photon absorption has only been studied in a handful of molecular fluorophores [6, 27–33]. However, the potential applications of entangled light–matter interactions make exploration and application in the materials field an intriguing possibility.

2.2 Hong–Ou–Mandel interference and biphotons

To better understand entangled photon light–matter interactions, it is insightful to look at the fundamentals of the Hong–Ou–Mandel (HOM) interference [34]. The HOM effect serves as the basis for most entangled spectroscopy methods. A step-by-step guide to constructing an HOM interferometer can be found in Ref. [35]. In general, one pump photon is down-converted to create two lower energy daughter photons through spontaneous parametric down-conversion (SPDC). The daughter photons are collectively termed a biphoton. After temporal and polarization compensation in one arm, the two photons are made to meet and interfere at a 50:50 beamsplitter. Two single photon avalanche detectors (SPADs) then measure whether the photons leave opposite or same sides of the beamsplitter.

Classically, there are four possible outcomes of transmission (T) and reflection (R) for the two photons, as depicted in Fig. 2.1(a): RR, TT, RT, TR. The indistinguishable character of the biphoton leads to the amplitudes of TT and RR destructively interfering in the entangled case [34], leaving the only measurable outcome of both photons leaving the same side of the beamsplitter. If the time delay or relative polarization between the photons is changed, or any other modification is made that

partially distinguishes the biphoton pair, the interference will decrease. The width and amplitude of the interference dip therefore carries a signature of the light–matter interaction that the entangled photons have witnessed [36]. Measuring these variations in the interference dip enable the possibility for spectroscopy. As an example, Fig. 2.1(b) and (c) show the modulation of the interference dip when absorption is introduced in one arm of the HOM interferometer [37].

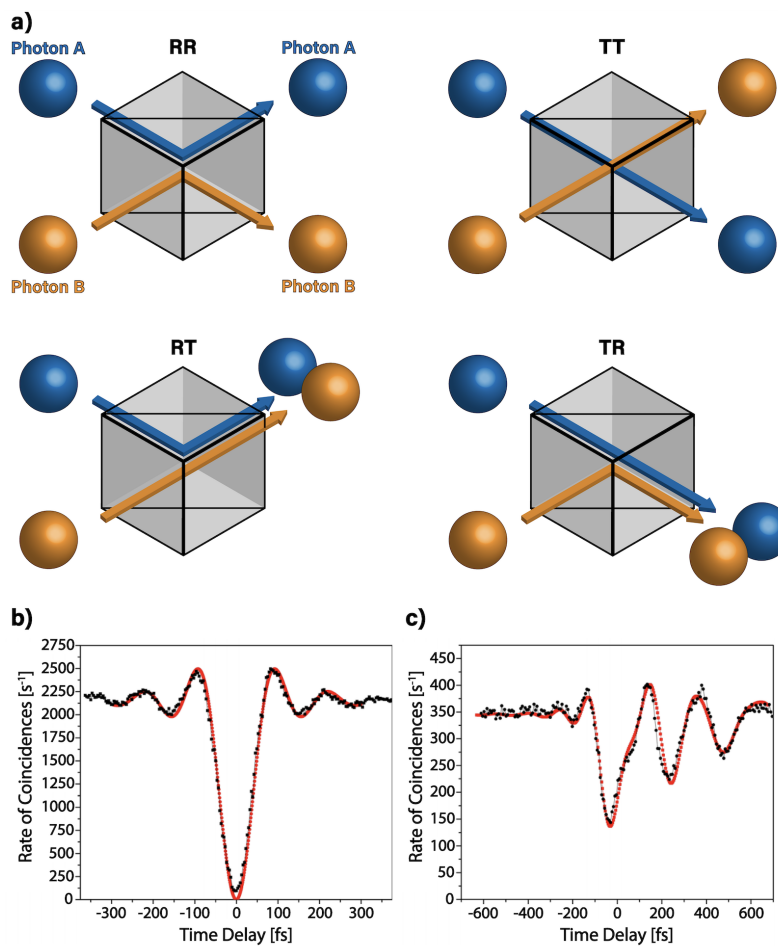


Figure 2.1: Hong–Ou–Mandel interference with photons. (a) Depiction of the four possible outcomes when two photons interact at a beamsplitter. When two entangled photons are present, the TT and RR outcomes cancel, and both photons leave the same side of the beam splitter. (b) This nonclassical interference leads to a dip in the coincidence counts. (c) HOM dip modulation due to a Nd:YAG crystal being placed in one arm of the HOM interferometer causing an entangled photon to interact with a sample with resonant states before the beam splitter. The excited state polarization is imprinted on the interference. Experimental results adapted from Ref. [37].

For a full mathematical derivation of the HOM dip, please refer to Ref. [38]. Briefly, the interference dip is explained mathematically as follows. Beamsplitter operators \hat{B}_a and \hat{B}_b are first defined which act on the bosonic mode operators to give a unitary transformation of an input state in ports a/b to the output in ports c/d.

$$\hat{a}^\dagger \xrightarrow{\hat{B}_a} \frac{1}{\sqrt{2}} (\hat{c}^\dagger + i\hat{d}^\dagger), \hat{b}^\dagger \xrightarrow{\hat{B}_b} \frac{1}{\sqrt{2}} (i\hat{c}^\dagger + \hat{d}^\dagger) \quad (2.1)$$

$$\hat{B}_a |1\rangle_a = \hat{B}_a \hat{a}^\dagger |0\rangle_a = \frac{1}{\sqrt{2}} (|1\rangle_c |0\rangle_d + i |0\rangle_c |1\rangle_d) \quad (2.2)$$

$$\hat{B}_b |1\rangle_b = \hat{B}_b \hat{b}^\dagger |0\rangle_b = \frac{1}{\sqrt{2}} (i |1\rangle_c |0\rangle_d + |0\rangle_c |1\rangle_d) \quad (2.3)$$

with \hat{a}^\dagger , \hat{b}^\dagger , \hat{c}^\dagger , and \hat{d}^\dagger being the creation operators for the photons in ports a, b, c, and d, respectively, acting on the vacuum state $|0\rangle$. It is important to note that the beamsplitter operator introduces a $\pi/2$ phase shift in the reflected photon's output state. Next, assume a pair of entangled photons, each of which is defined by a singly occupied Fock state, is introduced into both input ports a and b:

$$\begin{aligned} \hat{B}_a \hat{B}_b |1\rangle_a |1\rangle_b &= \frac{1}{2} (\hat{c}^\dagger + i\hat{d}^\dagger) (i\hat{c}^\dagger + \hat{d}^\dagger) |0\rangle_c |0\rangle_d \\ &= \frac{1}{2} (i\hat{c}^{\dagger 2} + \hat{c}^\dagger \hat{d}^\dagger - \hat{d}^\dagger \hat{c}^\dagger + i\hat{d}^{\dagger 2}) |0\rangle_c |0\rangle_d. \end{aligned} \quad (2.4)$$

The phase shift leads to the commutator term between the two photon modes in Eqn. 2.4. Given that the photons are indistinguishable, the commutation relation for the creation operators equals zero,

$$[\hat{c}^\dagger, \hat{d}^\dagger] = [\hat{c}^\dagger \hat{d}^\dagger - \hat{d}^\dagger \hat{c}^\dagger] = 0 \quad (2.5)$$

and the only terms left are the RT and TR terms such that both photons must leave the same side, resulting in a NOON state as the output:

$$\frac{1}{2} (i\hat{c}^{\dagger 2} + i\hat{d}^{\dagger 2}) |0\rangle_c |0\rangle_d = \frac{1}{\sqrt{2}} (i |2\rangle_c |0\rangle_d + |0\rangle_c |2\rangle_d). \quad (2.6)$$

Consequently, only one of the two photon counting detectors will register a detection event. This results in the characteristic interference dip in the coincidence counting

scheme (Fig. 2.1(b)). Entangled photon spectroscopy can therefore be thought of as a measure of how light–matter interactions modify the commutator in Eqn. 2.5.

Before a discussion of the practical considerations of SPDC, a few technical points should be clarified. First, HOM interference should be more correctly viewed as ‘biphoton interference’ since it relies on the indistinguishability of the two bosons as well as the underlying entanglement between them. Second, an HOM interference for a two-photon entangled state is only possible if the entangled biphoton wavepacket has a symmetric spectrum about the frequency degenerate diagonal, irrespective of whether the two photons are frequency degenerate or non-degenerate. Without this condition being met, the interference vanishes, and the beamsplitter becomes transparent with respect to the two input photons. In the case of two independent single-photon wavepackets, the condition for HOM interference indeed becomes that the two single-photon wavepackets must be identical. In practice, this means that care must be taken how the two-photon states to be used are generated and how the two independent beam paths are optically treated [39].

2.3 Generation and detection of entangled photons

The two down-converted photons from SPDC display strong correlations in time, energy, and momentum due to the parametric mixing process. The time and energy correlations originate from the individual photons being generated simultaneously with energies that must sum to that of the pump photon. The momentum correlation is dictated by the phase matching condition. Energy-time entangled states can be viewed as the most general type of entangled states. Hyper-entangled photon states, e.g., entangled both in energy-time and in polarization, can lead to significant improvements in the experimental measurement statistics and the robustness of the spectroscopic setup [40, 41].

The simplest experimental approach to SPDC is using birefringent phase matching (BPM) in a χ^2 nonlinear crystal such as β -barium borate or lithium triborate [42, 43]. Generation rates of $\sim 10^3 - 10^4$ counts per s per mW are achieved with pump powers of a few tens of mW. Given that SPADs generally saturate at around $10^6 - 10^7$ counts per s, this generation rate is sufficient for coincidence counting experiments with most pulsed laser systems. However, due to the strict phase matching condition, the generated entangled photons have a narrow bandwidth. Other issues include cross-polarized pump/daughter photon combinations in Type-I and Type-II down-

conversion, beam walk-off issues due to birefringence, a limited wavelength mixing range, and reliance on weaker nonlinear tensor elements.

Quasi-phase matching (QPM) can generate broadband entangled photons more efficiently for spectroscopic applications. In this approach, a spatially periodic modulation of a ferroelectric nonlinear material is used to rectify the phase-mismatch of the three-wave mixing process, as illustrated in Fig. 2.2(a). This is achieved by using the additional momentum contribution from the crystal periodicity in the overall phase matching [44, 45]. The QPM approach makes it possible to take advantage of stronger elements of the nonlinear tensor, as well as to implement Type-0 phase-matching whereby all three waves are co-polarized [46]. The down-converted photon flux can be as high as 10^9 pairs per s per mW of the pump power by spatially confining the pump in chip-integrated photonic waveguides [47]. A particularly salient feature of QPM is that, since the crystal period can be arbitrarily chosen, it can be used to phase-match any desirable wavelength combinations. Further, by utilizing a longitudinally varying period, a collection of phase matching conditions can be used to create broadband SPDC fluxes [48–51]. Temperature controlled lithium niobate, lithium tantalate, and potassium titanyl phosphate are generally used given that they are transparent from the UV to mid-infrared wavelengths [52, 53].

Quasi-phase matching allows for two important advantages in spectroscopy. First, a sufficiently broadband flux of entangled photons can be used to increase average power levels without saturating the single photon per mode limit. As measured in our lab and others, almost microwatt fluxes of entangled photons spanning more than 500 nm can be created using QPM gratings [54]. The broad bandwidth allows for pulse-shaping and few-femtosecond resolutions. Second, the enhanced power levels allow spectrally and temporally resolved detection in reasonable time frames. In practice, this means that even microwatts of pump power would be enough to saturate a SPAD, suggesting that ultrafast entangled photon spectroscopy can be driven by a CW diode laser instead of expensive femtosecond laser amplifiers. Chip-integrated entangled photons are also easily fiber coupled. This provides alignment-free daily operations and an easy way to control and maintain the properties of entangled photons, such as spatial profile, over a broad bandwidth.

Multiplexed photon counting schemes are another area that could yield benefits in the application of entangled spectroscopy in materials science. Both EM-CCDs and SPAD arrays are coming to maturity, allowing spectral multiplexing of the photon counting process [55–58]. With a broadband, higher flux source, even a

simple USB spectrometer can be used to measure spectral changes. Higher fluxes also allow phase-sensitive HOM techniques to be used which measure both 2nd and 3rd order correlations [59]. The difference between an HOM interferometer and a phase-unlocked HOM interferometer is conceptually similar to the difference between an autocorrelator and a frequency resolved optical gating (FROG) setup in ultrafast optics – the former only measures the intensity autocorrelation while the latter contains additional phase information.

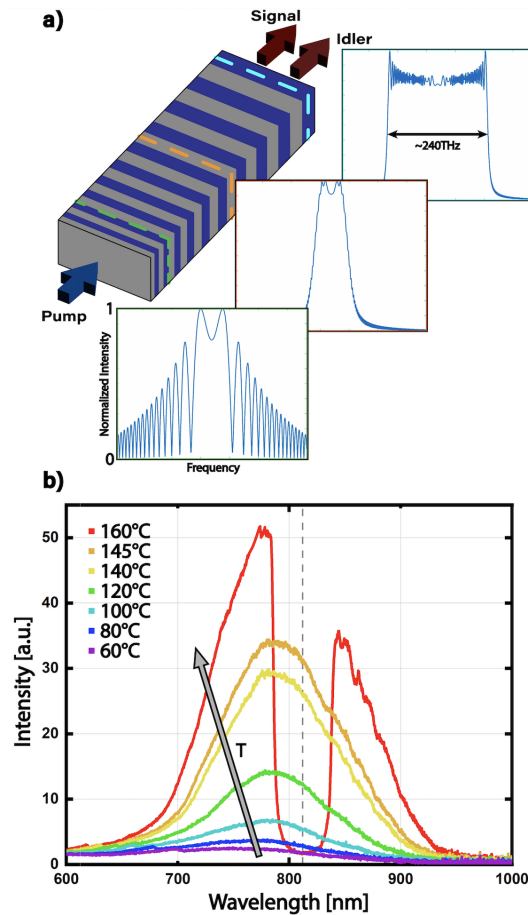


Figure 2.2: Periodic poling for generating broadband entangled photon pairs. (a) Cartoon of a periodically poled waveguide with linear chirp, where purple and gray represent domains of opposing poling. Insets show the simulated downconversion spectrum at three points along the lithium tantalate waveguide; (green)-start, (orange)-center, (cyan)-end. The effect of the chirp is to broaden the output to a bandwidth of ~ 240 THz (~ 510 nm). (b) Experimental spectra of a periodically poled lithium tantalate grating where the working temperature of the crystal is tuned.

2.4 Spectroscopy with one entangled photon

One class of entangled photon spectroscopy utilizes the non-local nature of the entanglement. The general idea is that the interaction between the sample and one photon in the entangled pair can be revealed by measuring its entangled partner, even when it does not interact with the sample directly. Experimentally, one photon interaction can be introduced by placing a sample in one arm of the HOM interferometer shown in Fig. 2.3. The sample imparts phase and amplitude changes on the entangled photon it interacts with, which affects the biphoton indistinguishability and modulates the HOM dip [37].

While it seems trivial to measure absorption profiles with entangled photon interference, the technique allows spectroscopy and microscopy at one wavelength using vastly different wavelengths [60–62]. Spectroscopic signatures, such as absorption spectra are reconstructed by monitoring the changes to the coincidence counts when a sample is inserted into the signal arm of the HOM interferometer and resolving the wavelength of the idler arm [63–65]. For example, if the SPDC process creates an entangled IR and visible photon pair, the absorption of the photon at the IR wavelength can be inferred by measuring its visible partner [66]. This particular case has been demonstrated in CO₂ as shown in Fig. 2.3 [60]. This effect is predicted to work for any range of experiments, such as X-Ray [67, 68], THz, and electron spectroscopies, although practical limitations arise from generating such ultra-broadband SPDC sources.

Entangled one-photon spectroscopy has been applied to applications ranging from remote sensing to ghost imaging. For example, quantum ghost imaging relies on the coherence between the down-converted beams to record the image of an object with photons that do not interact with it directly [62, 69–75]. Quantum optical coherence tomography (QOCT) offers improved resolution and sensitivity by exploiting the dispersion cancelling properties of the entangled wavepacket, as well as the anticorrelation between entangled pairs, to construct quantum interference patterns corresponding to sample depth [76–78]. Entangled photons can also increase measurement sensitivities as compared with classical photons. The standard quantum limit for noise scales as $1/\sqrt{N}$, where N is the number of measurements. Using entangled photons, this improves to $1/N$ [79]. A prototypical example is using N00N states to enhance the measurement precision of the phase shift in an interferometer [80, 81]. Sub-shot-noise imaging of weak absorbing objects has also been achieved [17].

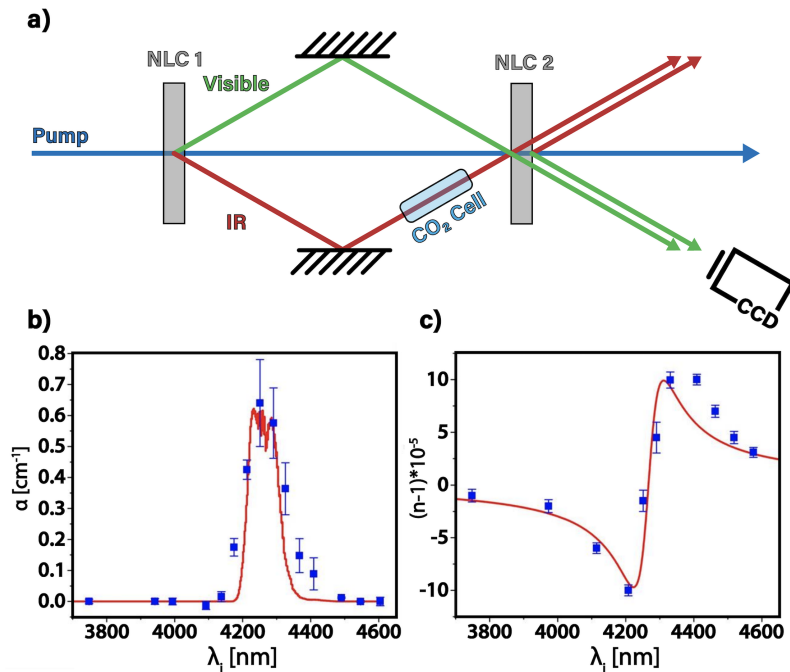


Figure 2.3: Measuring infrared absorption with visible photons. (a) Experimental layout. Entangled infrared (IR) and visible photons are generated through SPDC on the first nonlinear crystal (NLC1). A CO₂ cell is placed in the IR path to introduced absorption. The IR and visible photons cross at the second nonlinear crystal (NLC2) and interfere with the SPDC photons from NLC2. The interference pattern for the visible photons, which do not interact with the CO₂ are recorded. (b) IR absorption spectrum extracted from visible interference measurement. (c) Refractive index near the CO₂ resonance. Adapted from Ref. [60].

2.5 Spectroscopy with two or more entangled photons

Multiple entangled photon interactions can be split into two categories: the linearization of nonlinear interactions by preserving the correlations between the entangled photons (i.e., entangled two-photon absorption), and measurements in which a sample modifies the correlations between photons to measure excited state properties. Multiphoton entangled experiments are performed by replacing the beam splitter in an HOM interferometer so that both entangled photons interact with a sample. Whereas many one photon entangled interactions can be reproduced with shaped classical light, the interactions of two or more entangled photons with a sample lead to non-classical processes [14, 23, 82]. These interactions arise directly from the two-photon indistinguishability. Overly generalized, when the sample interacts with the biphoton pair, its response is as if only one photon were incident with the sum of

their energies. Before being spatially and temporally overlapped, the two entangled photons propagate in the material as if they were separate photons.

The two-photon interaction can therefore be modulated by time-delaying or shaping one side of the HOM interferometer. This allows for the measurement of excited state polarizations as well as populations. For example, multidimensional spectroscopy can be recreated by using three or more entangled photons or pulse shaping the entangled photons [14, 83, 84]. Compared to conventional multidimensional spectroscopy, entangled multidimensional spectroscopy is predicted to suppress the uncorrelated background levels and enhance the sensitivity to electronic couplings, manifested as pronounced off-diagonal cross-peaks in the 2D spectra, Fig. 2.4.

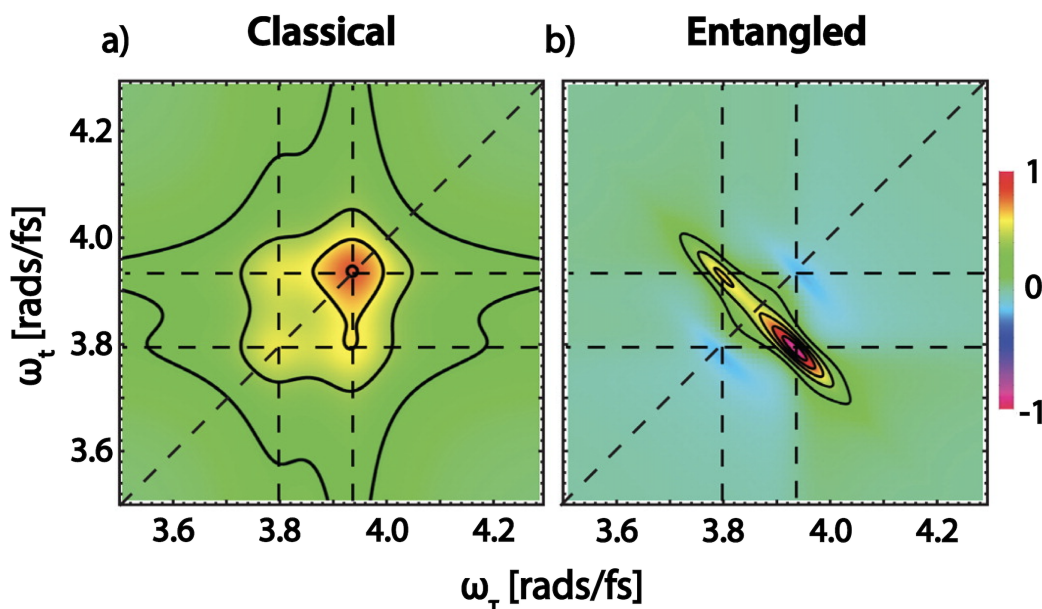


Figure 2.4: Simulated two-dimensional fluorescence spectra for electronically coupled molecular dimer with (a) classical light sources, and (b) entangled photon pairs. Multidimensional spectroscopy with entangled photons has improved sensitivity to the dimer conformation. Adapted from Ref. [83].

There are other distinct differences between nonlinear entangled and classical spectroscopy. First, the two entangled photons are predicted to act as one only if their coherence/entanglement time, represented by the width of the HOM dip, is shorter than the decoherence of the excited state being measured. The coherence/entanglement time can therefore be used to alter and control the nonlinear process, allowing another route to multidimensional spectroscopy [85]. The measured spectrum is

again more sensitive to electronic coupling than in the classical case. Second, temporal dynamics in entangled photon experiments are measured via the correlations between the two entangled photons. Unlike pump probe spectroscopy, the temporal dynamics are not inferred from the sample's impulse response to a multiphoton pump pulse. Third, the entangled photons can measure whether an excited state superposition they excite in a qubit preserves their entanglement. Entangled photon interactions are therefore predicted to be sensitive probes for many-body dynamics and collective states [24, 86, 87].

Entangled photon spectroscopy also has the potential to measure ultrafast dynamics with higher spectral resolution than a classical approach. For entangled photon spectroscopy, the energy resolution is given by the down-converted pump source's linewidth. This is because the frequency–frequency photon distribution created by SPDC is correlated to the downconverted center frequency as shown in Fig. 2.5 [21]. This is compared with the Gaussian distribution commonly associated with a laser, in which any two photons can interact with the sample (Fig. 2.5(a) compared to Fig. 2.5(b)). In an entangled interaction, only the frequency conjugate pair will interact with the material, postselecting the photons along the frequency diagonal. All entangled photon interactions therefore add up to within the pump linewidth of the original pump laser source for the SPDC, and the frequency resolution is decoupled from the temporal resolution (Fig. 2.5(c) compared to Fig. 2.5(d)). Broadband entangled two-photon absorption in rubidium has already demonstrated a 3 to 5 orders of magnitude improvement on spectral and temporal resolution [88]. It has also been suggested that the creation of only conjugate electric fields optimizes the otherwise nonlinear interaction.

The temporal resolution of the entangled experiment is still proportional to the bandwidth of the down-converted photons. The width of the HOM dip can therefore be changed by modulating the relative time delay of the different frequencies using a pulse shaper [88]. Combining pulse-shaping and entangled photons is predicted to allow non-classical population distribution and novel photochemistry processes [88–91]. The decoupled temporal and spectral resolution has been predicted to create narrow bandwidth excited state populations from femtosecond bandwidths as shown in Fig. 2.5(e) compared to Fig. 2.5(f). Simulation also suggests that under entangled two-photon excitation, the intermediate single-exciton transport in the bacterial reaction center of *Blastochloris viridis* can be suppressed and nonclassical control of two-exciton states can be achieved [89].

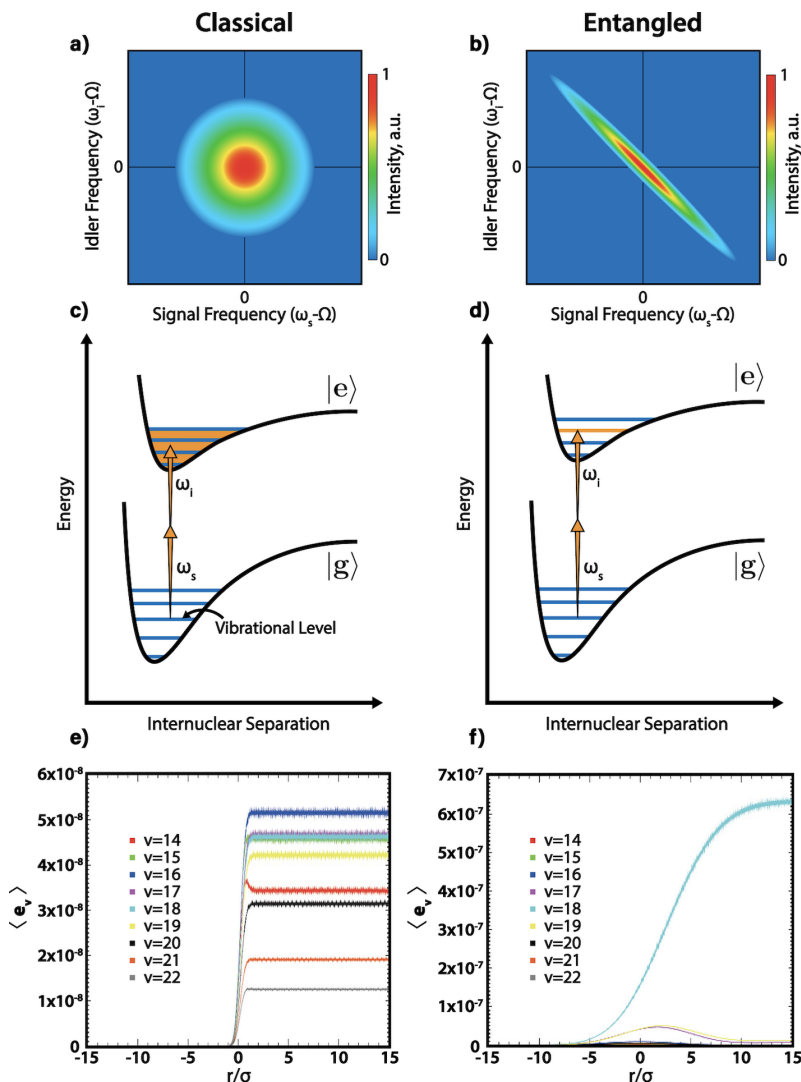


Figure 2.5: Spectral resolution in entangled two-photon spectroscopy. (a) Gaussian frequency distribution for uncorrelated photons as common from a classical laser. (b) Frequency anti-correlation for entangled photon pairs from SPDC. (c) The classical frequency distribution means that any combination of photons can excite the sample. A pulsed laser therefore excites an ensemble of vibrational states as predicted in (e). (d) The entangled photon frequency distribution means that transitions only occur that add up to the pump source's linewidth. Selective excitation of a single vibronic level therefore is predicted to occur independent of the SPDC bandwidth and temporal resolution (f). (e) Excited states population with pulsed laser excitation, where multiple vibronic levels are populated. Theoretical data (e) and (f) adapted from Ref. [21].

2.6 Current directions in entangled light-matter interactions

Several intriguing directions exist in exploring entangled light-matter interactions. One entangled photon interaction suggests that material and molecular interactions

can modulate the probability of measuring a second, non-interacting photon. The role this could have in transmuting material and chemical changes, as well as in processes like energy transfer, leave many open questions. Perhaps most intriguing are interactions with two or more entangled photons. Oversimplified, when two entangled photons are incident on a sample, they can appear as one photon with their summed energy. Nonlinear, multiphoton interactions up to N photons are therefore predicted to scale linearly [10]. The linearity of two photon entangled process was previously measured in sodium and cesium [7, 8] and has now been repeated in some molecular and solid-state systems (Fig. 6) [4, 6, 7, 9, 32, 33]. Similar to the beamsplitter in the HOM interferometer, the strong amplitude and phase correlation [92] within the entangled photon pair of SPDC suppresses higher order interaction terms [88].

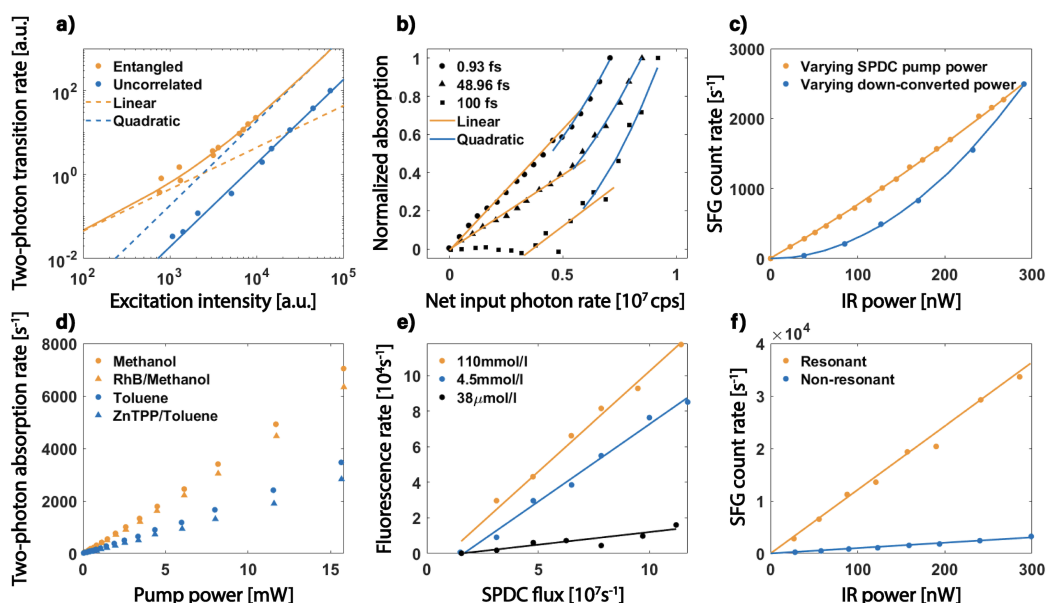


Figure 2.6: The linearity of various entangled two-photon processes as a function of power. (a) Two-photon transition rate in trapped cesium with entangled and coherent light. Transition rate for uncorrelated coherent excitation is reduced by a factor of 10 for comparison. (b) Power dependence of ETPA rate in porphyrin dendrimer under 3 different entanglement times. (c) Power dependence of sum-frequency generation with entangled photons. (d) ETPA rate for RhB and ZnTPP in solvent. (e) ETPA-induced fluorescence rate for Rh6G in ethanol under different concentration. (f) Resonantly enhanced sum-frequency generation with entangled photons. Data presented are adapted from Refs. [4, 6, 7, 9, 32, 33].

While the entangled two-photon intensity scaling can be understood, the cross section of the process raises many questions. The entangled photon cross sections

measured to date in molecular systems fall within the $10^{-17} - 10^{-18} \text{ cm}^2$ range [6]. This cross section is closer to that of a single photon absorption event, 10^{-16} cm^2 , and orders of magnitude larger than that of a classical two-photon absorption event, $10^{-47} \text{ cm}^4\text{s}$. Why the entangled two-photon absorption cross section does not match the classical one photon cross section, despite both processes being linear, is an open question. The entangled two-photon absorption cross section also does not appear to follow classical two-photon absorption rules in organic porphyrin dendrimers [6].

In practice, the entangled two-photon absorption will compete with the semiclassical two-photon absorption. Their relative contribution is quantified by the ratio between the entangled absorption rate αI and the uncorrelated two-photon absorption rate βI^2 , where α and β are associated cross sections. An entangled process is more efficient ($I < \alpha/\beta$) for fluxes lower than a GW for currently measured cross sections. The ratio can also be used to see that, for example, a one mW entangled photon flux has the same excitation rate as a million times more powerful classical laser. When calculating these ratios, it is important to include the conversion from W to photons per s through the ratio of $1J = 6.242 * 10^{18} \text{ eV}$ for the βI^2 . This must be done to cancel the cm^4s units when going to photons per s.

To study ultrafast material dynamics, an important factor in entangled two-photon absorption is the coherence (entanglement time) relative to the decoherence of the excited state. Studies on several diatomic molecules and organic porphyrin dendrimers have suggested that transitions involving virtual states respond to entangled two-photon excitations at a different timescale than transitions involving other mechanisms, such as excited state charge transfer [6, 93]. The entangled two-photon absorption cross section may therefore vary drastically between different transitions, exhibiting nonmonotonic dependence on the entanglement time, even if two systems classical cross sections are similar.

However, few experimental systems have been measured to date to confirm these rules. Measurements have yet to be repeated in condensed matter, low dimensional materials, or other common molecules — leaving many open questions as to how two or more photon entangled interactions can be optimized. The primary questions can be summarized as: (1) how do intermediate states control the entangled photon interaction, (2) what structural motifs can increase or decrease the strength of the entangled photon interaction, (3) how does excited state coupling with spins, vibrations, and electrons preserve or decrease the entangled light–matter interactions, and (4) more generally, how to utilize entanglement to reveal and engineer novel ma-

terials and device responses that are not accessible with traditional methods. Other open questions, such as how selection rules are modified by polarization entangled photons and how photonic enhancement techniques will modify the interactions [94–102], promise for intriguing expansions to existing fields.

Controlling the entangled multiphoton interactions has practical as well as fundamental motivation. Entangled two-photon processes can occur at the same rate as a pulsed-laser-induced two-photon excitations but at over a million times lower fluxes, accounting for the intensity scaling between quadratic and linear processes. If the material and molecular design parameters can be optimized, optoelectronic and biomedical applications using two-photon processes could be driven by a CW laser diode instead of a pulsed laser. Theory has also shown that due to the linear scaling, the spectrally overlapped simulated Raman scattering and two-photon absorption can be separated and selectively excited by tuning the entanglement properties of the pump [103]. For imaging applications, entangled two-photon fluorescence is suitable for in-depth imaging of photosensitive tissues at low flux. The linear scaling and enhanced cross section are predicted to occur for N-photon interactions, potentially bringing linearization to a family of nonlinear optical techniques [10]. Entangled multiphoton interactions have also been predicted to increase resonance energy transfer by several orders of magnitude [104] — and it can be extrapolated that the entangled effects will extend to most applications of multiphoton processes.

2.7 New opportunities in materials science

The key distinction of entangled photon excitation, aside from the linearization of nonlinear processes, is that the entangled photons can be made to show quantum correlations in multiple variables (polarization, energy, OAM, etc.) [105]. By interfering these entangled states of light with the quantum correlated excitations of a material, new properties and applications are to be expected [106]. Or, it may be possible to dynamically form correlations between two independent excitations that are not regularly present [107–111]. This key difference may lead to new insights in spectroscopy, but perhaps more excitingly, new degrees of control in quantum materials. In this section, we outline a few potential directions that entangled light-matter interactions could have an immediate benefit in.

First and foremost, the study and understanding of entangled light-matter interactions could become critical in the age of quantum computing and information systems [112, 113]. How the entangled photon correlations are modified, favor-

ably or not, by material elements is key for coupling qubit systems together as well as for investigating the types of control schemes that could be applicable to complex quantum systems [114]. Perhaps even more fundamentally, entanglement is suggested to be at the heart of quantum materials, which display strong electronic and nucleon correlations [115]. The inclusion of correlations in any Hamiltonian is the key to describing complex phenomena and for accurate calculations [116]. Many such Hamiltonians are also proposed to include entanglement, such as singlet–triplet scattering [25]. While the Fermi liquid theory and the Hubbard model have been used with great success, the direct experimental measurement of these strong interactions remains a difficult challenge [117–119]. The change in entangled photon correlations interacting with such systems may prove key, complementing approaches like ultracold atoms in optical lattices [120] and second quanta scans in multidimensional spectroscopy [121].

The ability of entangled photons to perform nonlinear optics with low power CW lasers should also prove transformative for photonics and electro-optical devices. Common components such as frequency mixers, saturable absorbers, or phase shifters can operate without a pulsed laser input, while wide band gap materials can be interacted with via photons at half the band gap energy. Additional functionality can be implemented in such devices relying on the preservation or change of the entangled photon correlations. An experiment that demonstrates this concept is to create polarization entangled biphoton states and couple one of the photons into a plasmonic metamaterial [122]. The coupled polarization state is determined and modulated by detecting the polarization of its partner. By altering the coupled polarization non-locally, the plasmonic device could in principle operate from perfect absorption to full transmission. The general idea of manipulating the material's functions non-locally via entanglement could lead to multifunctional integrated devices such as quantum logic gates, but also has fundamental advantages in processes like resonant energy transfer [104, 123].

An important goal in materials science is the on-demand manipulation of electrons in solids via the application of external stimuli [124]. The coupling of the entangled photon pair's quantum correlations to strongly correlated materials could result in novel, exotic responses. One example would be in the field of valleytronics [125, 126]. In two-dimensional semiconductors such as MoS_2 , distinct valleys can be populated under a resonant excitation by circularly polarized light [125]. The circularly polarized excitation photon can be replaced by an entangled photon

pair. More precisely, a cross-polarized pair could be generated via Type-II down-conversion, after which the biphoton is split into its orthogonal polarization modes via a polarizing beamsplitter. A subsequent change in basis to circular polarization can be achieved by a pair of quarter-waveplates in both arms of the HOM type setup. The entangled photon energies could be set to select one or both valley excitations. The superposition between the spin state and the entangled photons would allow measurements of spin decoherence and coupling between the valleys. A similar idea could be used to test the ability of topological insulators to maintain spin correlations relative to photonic correlations.

Entangled photons could also find applications in material fabrication and lithography. Proposed techniques such as quantum photolithography aim to utilize entangled photons prepared in a N00N state to overcome the diffraction limit by a factor of $1/N$, alleviating the need to go to shorter UV wavelengths [127]. The enhanced cross section for entangled multiphoton absorption could allow simplified photolithography and growth schemes, techniques that use below band gap light for patterning, or even additional degrees of freedom by using two or more entangled states. The microscopic chemical processes that govern photopolymerization or photocatalytic growth processes might similarly be tuned by entanglement.

2.8 Outlook

While much work has gone into exploring entangled photons for quantum information and computational applications, the basics of entangled light-matter interactions and the potential applications in chemistry and material science are largely unexplored. In general, the field is advancing rapidly on the theoretical front, but most experimental questions remain open. How materials and molecular design can control entangled light-matter interactions remains mostly unknown, especially in materials and condensed matter systems. Given the relative ease of high-flux entangled photon generation, the simplicity of the optical schemes, and the various potential advantages of using non-classical light, we foresee entangled light-matter interactions being a rapidly growing field in the near future.

References

1. Horodecki, R., Horodecki, P., Horodecki, M. & Horodecki, K. Quantum entanglement. *Reviews of Modern Physics* **81**, 865–942. <https://link.aps.org/doi/10.1103/RevModPhys.81.865> (2018) (June 2009).

2. Nielsen, M. A. & Chuang, I. Quantum Computation and Quantum Information. *American Journal of Physics* **70**, 558–559. <https://aapt.scitation.org/doi/10.1119/1.1463744> (2020) (Apr. 2002).
3. Javanainen, J. & Gould, P. L. Linear intensity dependence of a two-photon transition rate. *Physical Review A* **41**, 5088–5091. <https://link.aps.org/doi/10.1103/PhysRevA.41.5088> (2019) (May 1990).
4. Dayan, B., Pe'er, A., Friesem, A. A. & Silberberg, Y. Nonlinear Interactions with an Ultrahigh Flux of Broadband Entangled Photons. *Physical Review Letters* **94**, 043602. <https://link.aps.org/doi/10.1103/PhysRevLett.94.043602> (2020) (Feb. 2005).
5. Dayan, B. Theory of two-photon interactions with broadband down-converted light and entangled photons. *Physical Review A* **76**, 043813. <https://link.aps.org/doi/10.1103/PhysRevA.76.043813> (2020) (Oct. 2007).
6. Lee, D.-I. & Goodson, T. Entangled Photon Absorption in an Organic Porphyrin Dendrimer. *The Journal of Physical Chemistry B* **110**, 25582–25585. <https://doi.org/10.1021/jp066767g> (2018) (Dec. 2006).
7. Georgiades, N. P., Polzik, E. S., Edamatsu, K., Kimble, H. J. & Parkins, A. S. Nonclassical Excitation for Atoms in a Squeezed Vacuum. *Physical Review Letters* **75**, 3426–3429. <https://link.aps.org/doi/10.1103/PhysRevLett.75.3426> (2020) (Nov. 1995).
8. Teich, M. C., Schroeder, J. M. & Wolga, G. J. Double-Quantum Photoelectric Emission from Sodium Metal. *Physical Review Letters* **13**, 611–614. <https://link.aps.org/doi/10.1103/PhysRevLett.13.611> (2020) (Nov. 1964).
9. Sensarn, S., Ali-Khan, I., Yin, G. Y. & Harris, S. E. Resonant Sum Frequency Generation with Time-Energy Entangled Photons. *Physical Review Letters* **102**, 053602. <https://link.aps.org/doi/10.1103/PhysRevLett.102.053602> (2020) (Feb. 2009).
10. Peřina, J., Saleh, B. E. A. & Teich, M. C. Multiphoton absorption cross section and virtual-state spectroscopy for the entangled n -photon state. *Physical Review A* **57**, 3972–3986. <https://link.aps.org/doi/10.1103/PhysRevA.57.3972> (2018) (May 1998).
11. Matsukevich, D. N. *et al.* Entanglement of a Photon and a Collective Atomic Excitation. *Physical Review Letters* **95**, 040405. <https://link.aps.org/doi/10.1103/PhysRevLett.95.040405> (2020) (July 2005).
12. Xiang, B. *et al.* Manipulating optical nonlinearities of molecular polaritons by delocalization. *Science Advances* **5**, eaax5196. <https://advances.sciencemag.org/lookup/doi/10.1126/sciadv.aax5196> (2020) (Sept. 2019).

13. Ribeiro, R. F., Martínez-Martínez, L. A., Du, M., Campos-Gonzalez-Angulo, J. & Yuen-Zhou, J. Polariton chemistry: Controlling molecular dynamics with optical cavities. *Chemical Science* **9**, 6325–6339. <https://pubs.rsc.org/en/content/articlelanding/2018/sc/c8sc01043a> (2020) (Aug. 2018).
14. Dorfman, K. E., Schlawin, F. & Mukamel, S. Nonlinear optical signals and spectroscopy with quantum light. *Reviews of Modern Physics* **88**, 045008. <https://link.aps.org/doi/10.1103/RevModPhys.88.045008> (2018) (Dec. 2016).
15. Kuzmich, A. & Mandel, L. Sub-shot-noise interferometric measurements with two-photon states. *Quantum and Semiclassical Optics: Journal of the European Optical Society Part B* **10**, 493–500. <http://stacks.iop.org/1355-5111/10/i=3/a=008?key=crossref.fd33afd748cab2e17dfba547b16192e> (2020) (June 1998).
16. Slussarenko, S. *et al.* Unconditional violation of the shot-noise limit in photonic quantum metrology. *Nature Photonics* **11**, 700–703. <https://www.nature.com/articles/s41566-017-0011-5> (2023) (Nov. 2017).
17. Brida, G., Genovese, M. & Ruo Berchera, I. Experimental realization of sub-shot-noise quantum imaging. *Nature Photonics* **4**, 227–230. <https://www.nature.com/articles/nphoton.2010.29> (2020) (Apr. 2010).
18. Hosten, O., Engelsen, N. J., Krishnakumar, R. & Kasevich, M. A. Measurement noise 100 times lower than the quantum-projection limit using entangled atoms. *Nature* **529**, 505–508. <https://www.nature.com/articles/nature16176> (2020) (Jan. 2016).
19. Giovannetti, V., Lloyd, S. & Maccone, L. Quantum-Enhanced Measurements: Beating the Standard Quantum Limit. *Science* **306**, 1330–1336. <http://science.sciencemag.org/content/306/5700/1330> (2018) (Nov. 2004).
20. Oka, H. Enhanced vibrational-mode-selective two-step excitation using ultrabroadband frequency-entangled photons. *Physical Review A* **97**, 063859. <https://link.aps.org/doi/10.1103/PhysRevA.97.063859> (2019) (June 2018).
21. Oka, H. Selective two-photon excitation of a vibronic state by correlated photons. *The Journal of Chemical Physics* **134**, 124313. <https://aip.scitation.org/doi/10.1063/1.3573565> (2019) (Mar. 2011).
22. Schlawin, F., Dorfman, K. E., Fingerhut, B. P. & Mukamel, S. Manipulation of two-photon-induced fluorescence spectra of chromophore aggregates with entangled photons: A simulation study. *Physical Review A* **86**, 023851. <https://link.aps.org/doi/10.1103/PhysRevA.86.023851> (2020) (Aug. 2012).

23. Schlawin, F., Dorfman, K. E. & Mukamel, S. Entangled Two-Photon Absorption Spectroscopy. *Accounts of Chemical Research* **51**, 2207–2214. <https://doi.org/10.1021/acs.accounts.8b00173> (2018) (Sept. 2018).
24. Bittner, E. R., Li, H., Piryatinski, A., Srimath Kandada, A. R. & Silva, C. Probing exciton/exciton interactions with entangled photons: Theory. *The Journal of Chemical Physics* **152**, 071101. <https://aip.scitation.org/doi/10.1063/1.5139197> (2020) (Feb. 2020).
25. Buscemi, F., Bordone, P. & Bertoni, A. Entanglement dynamics of electron-electron scattering in low-dimensional semiconductor systems. *Physical Review A* **73**, 052312. <https://link.aps.org/doi/10.1103/PhysRevA.73.052312> (2023) (May 2006).
26. Huang, Z. & Kais, S. Entanglement as measure of electron–electron correlation in quantum chemistry calculations. *Chemical Physics Letters* **413**, 1–5. <https://www.sciencedirect.com/science/article/pii/S0009261405010651> (2023) (Sept. 2005).
27. Eshun, A., Cai, Z., Awies, M., Yu, L. & Goodson, T. Investigations of Thienoacene Molecules for Classical and Entangled Two-Photon Absorption. *The Journal of Physical Chemistry A* **122**, 8167–8182. <https://doi.org/10.1021/acs.jpca.8b06312> (2018) (Oct. 2018).
28. Guzman, A. R., Harpham, M. R., Süzer, Ö., Haley, M. M. & Goodson, T. G. Spatial Control of Entangled Two-Photon Absorption with Organic Chromophores. *Journal of the American Chemical Society* **132**, 7840–7841. <https://doi.org/10.1021/ja1016816> (2019) (June 2010).
29. Harpham, M. R., Süzer, Ö., Ma, C.-Q., Bäuerle, P. & Goodson, T. Thiophene Dendrimers as Entangled Photon Sensor Materials. *Journal of the American Chemical Society* **131**, 973–979. <https://doi.org/10.1021/ja803268s> (2019) (Jan. 2009).
30. Varnavski, O., Pinsky, B. & Goodson, T. Entangled Photon Excited Fluorescence in Organic Materials: An Ultrafast Coincidence Detector. *The Journal of Physical Chemistry Letters* **8**, 388–393. <https://doi.org/10.1021/acs.jpcllett.6b02378> (2020) (Jan. 2017).
31. Villabona-Monsalve, J. P., Varnavski, O., Palfey, B. A. & Goodson, T. Two-Photon Excitation of Flavins and Flavoproteins with Classical and Quantum Light. *Journal of the American Chemical Society* **140**, 14562–14566. <https://doi.org/10.1021/jacs.8b08515> (2018) (Nov. 2018).
32. Tabakaev, D. *et al.* Energy-time-entangled two-photon molecular absorption. *Physical Review A* **103**, 033701. <https://link.aps.org/doi/10.1103/PhysRevA.103.033701> (2021) (Mar. 2021).

33. Villabona-Monsalve, J. P., Calderón-Losada, O., Nuñez Portela, M. & Valencia, A. Entangled Two Photon Absorption Cross Section on the 808 nm Region for the Common Dyes Zinc Tetraphenylporphyrin and Rhodamine B. *The Journal of Physical Chemistry A* **121**, 7869–7875. <https://doi.org/10.1021/acs.jpca.7b06450> (2018) (Oct. 2017).
34. Hong, C. K., Ou, Z. Y. & Mandel, L. Measurement of subpicosecond time intervals between two photons by interference. *Physical Review Letters* **59**, 2044–2046. <https://link.aps.org/doi/10.1103/PhysRevLett.59.2044> (2018) (Nov. 1987).
35. Galvez, E. J. *et al.* Interference with correlated photons: Five quantum mechanics experiments for undergraduates. *American Journal of Physics* **73**, 127–140. <https://aapt.scitation.org/doi/10.1119/1.1796811> (2018) (Jan. 2005).
36. Gianani, I. Robust spectral phase reconstruction of time-frequency entangled bi-photon states. *Physical Review Research* **1**, 033165. <https://link.aps.org/doi/10.1103/PhysRevResearch.1.033165> (2020) (Dec. 2019).
37. Kalashnikov, D. A. *et al.* Quantum interference in the presence of a resonant medium. *Scientific Reports* **7**, 11444. <https://www.nature.com/articles/s41598-017-11694-z> (2021) (Sept. 2017).
38. Scully, M. O. & Zubairy, M. S. *Quantum Optics* ISBN: 978-0-521-43595-6. <https://www.cambridge.org/core/books/quantum-optics/08DC53888452CBC6CDC0FD8A1A1A4DD7> (Cambridge University Press, Cambridge, 1997).
39. Lavoie, J. *et al.* Phase-Modulated Interferometry, Spectroscopy, and Refractometry using Entangled Photon Pairs. *Advanced Quantum Technologies* **3**, 1900114. <https://onlinelibrary.wiley.com/doi/abs/10.1002/qute.201900114> (2022) (2020).
40. Barreiro, J. T., Langford, N. K., Peters, N. A. & Kwiat, P. G. Generation of Hyperentangled Photon Pairs. *Physical Review Letters* **95**, 260501. <https://link.aps.org/doi/10.1103/PhysRevLett.95.260501> (2020) (Dec. 2005).
41. Kwiat, P. G. Hyper-entangled states. *Journal of Modern Optics* **44**, 2173–2184. <https://www.tandfonline.com/doi/abs/10.1080/09500349708231877> (2020) (Nov. 1997).
42. Trojek, P., Schmid, C., Bourennane, M., Weinfurter, H. & Kurtsiefer, C. Compact source of polarization-entangled photon pairs. *Optics Express* **12**, 276–281. <https://www.osapublishing.org/oe/abstract.cfm?uri=oe-12-2-276> (2020) (Jan. 2004).

43. Volz, J., Kurtsiefer, C. & Weinfurter, H. Compact all-solid-state source of polarization-entangled photon pairs. *Applied Physics Letters* **79**, 869–871. <https://aip.scitation.org/doi/10.1063/1.1389835> (2020) (Aug. 2001).
44. Fejer, M. M. in *Guided Wave Nonlinear Optics* (eds Ostrowsky, D. B. & Reinisch, R.) 133–145 (Springer Netherlands, Dordrecht, 1992). ISBN: 978-94-011-2536-9. https://doi.org/10.1007/978-94-011-2536-9_9 (2020).
45. Armstrong, J. A., Bloembergen, N., Ducuing, J. & Pershan, P. S. Interactions between Light Waves in a Nonlinear Dielectric. *Physical Review* **127**, 1918–1939. <https://link.aps.org/doi/10.1103/PhysRev.127.1918> (2019) (Sept. 1962).
46. Byer, R. L. Quasi-Phasematched Nonlinear Interactions and Devices. *Journal of Nonlinear Optical Physics & Materials* **06**, 549–592. <https://www.worldscientific.com/doi/10.1142/S021886359700040X> (2020) (Dec. 1997).
47. Jechow, A., Heuer, A. & Menzel, R. High brightness, tunable biphoton source at 976 nm for quantum spectroscopy. *Optics Express* **16**, 13439–13449. <https://www.osapublishing.org/oe/abstract.cfm?uri=oe-16-17-13439> (2020) (Aug. 2008).
48. Sensarn, S., Yin, G. Y. & Harris, S. E. Generation and Compression of Chirped Biphotons. *Physical Review Letters* **104**, 253602. <https://link.aps.org/doi/10.1103/PhysRevLett.104.253602> (2020) (June 2010).
49. Harris, S. E. & Sensarn, S. *Toward Single-Cycle Biphotons in Conference on Coherence and Quantum Optics (2007), paper CMD1* (Optical Society of America, June 2007), CMD1. <https://www.osapublishing.org/abstract.cfm?uri=CQO-2007-CMD1> (2019).
50. Harris, S. E. Chirp and Compress: Toward Single-Cycle Biphotons. *Physical Review Letters* **98**, 063602. <https://link.aps.org/doi/10.1103/PhysRevLett.98.063602> (2020) (Feb. 2007).
51. Carrasco, S. *et al.* Enhancing the axial resolution of quantum optical coherence tomography by chirped quasi-phase matching. *Optics Letters* **29**, 2429–2431. <https://www.osapublishing.org/ol/abstract.cfm?uri=ol-29-20-2429> (2019) (Oct. 2004).
52. Hum, D. S. & Fejer, M. M. Quasi-phasematching. *Comptes Rendus Physique* **8**, 180–198. <http://adsabs.harvard.edu/abs/2007CRPhy...8..180H> (2019) (Mar. 2007).
53. León-Montiel, R. d. J., Svozilík, J., Torres, J. P. & U'Ren, A. B. Temperature-Controlled Entangled-Photon Absorption Spectroscopy. *Physical Review Letters* **123**, 023601. <https://link.aps.org/doi/10.1103/PhysRevLett.123.023601> (2023) (July 2019).

54. Nasr, M. B. *et al.* Ultrabroadband Biphotons Generated via Chirped Quasi-Phase-Matched Optical Parametric Down-Conversion. *Physical Review Letters* **100**, 183601. <https://link.aps.org/doi/10.1103/PhysRevLett.100.183601> (2019) (May 2008).
55. Lubin, G. *et al.* Quantum correlation measurement with single photon avalanche diode arrays. *Optics Express* **27**, 32863–32882. <https://www.osapublishing.org/oe/abstract.cfm?uri=oe-27-23-32863> (2020) (Nov. 2019).
56. Reichert, M., Defienne, H. & Fleischer, J. W. Massively Parallel Coincidence Counting of High-Dimensional Entangled States. *Scientific Reports* **8**, 1–7. <https://www.nature.com/articles/s41598-018-26144-7> (2019) (May 2018).
57. Moreau, P.-A., Mougins-Sisini, J., Devaux, F. & Lantz, E. Realization of the purely spatial Einstein-Podolsky-Rosen paradox in full-field images of spontaneous parametric down-conversion. *Physical Review A* **86**, 010101. <https://link.aps.org/doi/10.1103/PhysRevA.86.010101> (2020) (July 2012).
58. Edgar, M. P. *et al.* Imaging high-dimensional spatial entanglement with a camera. *Nature Communications* **3**, 1–6. <https://www.nature.com/articles/ncomms1988> (2020) (Aug. 2012).
59. Abouraddy, A. F., Yarnall, T. M. & Di Giuseppe, G. Phase-unlocked Hong-Ou-Mandel interferometry. *Physical Review A* **87**, 062106. <https://link.aps.org/doi/10.1103/PhysRevA.87.062106> (2019) (June 2013).
60. Kalashnikov, D. A., Paterova, A. V., Kulik, S. P. & Krivitsky, L. A. Infrared spectroscopy with visible light. *Nature Photonics* **10**, 98–101. <https://www.nature.com/articles/nphoton.2015.252> (2018) (Feb. 2016).
61. Lindner, C., Wolf, S., Kiessling, J. & Kühnemann, F. Fourier transform infrared spectroscopy with visible light. *Optics Express* **28**, 4426–4432. <https://www.osapublishing.org/oe/abstract.cfm?uri=oe-28-4-4426> (2020) (Feb. 2020).
62. Kviatkovsky, I., Chrzanowski, H. M., Avery, E. G., Bartolomaeus, H. & Ramelow, S. Microscopy with undetected photons in the mid-infrared. *Science Advances*. <https://www.science.org/doi/abs/10.1126/sciadv.abd0264> (2022) (Oct. 2020).
63. Kalachev, A. A. *et al.* Biphoton spectroscopy of YAG:Er³⁺ crystal. *Laser Physics Letters* **4**, 722. <https://iopscience.iop.org/article/10.1002/lapl.200710061/meta> (2020) (June 2007).
64. Kalachev, A. A. *et al.* Biphoton spectroscopy in a strongly nondegenerate regime of SPDC. *Laser Physics Letters* **5**, 600–602. <https://onlinelibrary.wiley.com/doi/abs/10.1002/lapl.200810044> (2019) (2008).

65. Yabushita, A. & Kobayashi, T. Spectroscopy by frequency entangled photon pairs. *Physical Review A* **69**, 013806. <http://arxiv.org/abs/quant-ph/0306154> (2019) (Jan. 2004).
66. Paterova, A., Yang, H., An, C., Kalashnikov, D. & Krivitsky, L. Measurement of infrared optical constants with visible photons. *New Journal of Physics* **20**, 043015. <https://doi.org/10.1088%2F1367-2630%2Faab5ce> (2020) (Apr. 2018).
67. Adams, B. W. *et al.* X-ray quantum optics. *Journal of Modern Optics* **60**, 2–21. <https://doi.org/10.1080/09500340.2012.752113> (2020) (Jan. 2013).
68. Shwartz, S. & Harris, S. E. Polarization Entangled Photons at X-Ray Energies. *Physical Review Letters* **106**, 080501. <https://link.aps.org/doi/10.1103/PhysRevLett.106.080501> (2020) (Feb. 2011).
69. Padgett, M. J. & Boyd, R. W. An introduction to ghost imaging: Quantum and classical. *Philosophical transactions. Series A, Mathematical, physical, and engineering sciences* **375**. <https://www.ncbi.nlm.nih.gov/pmc/articles/PMC5487713/> (2019) (Aug. 2017).
70. Abouraddy, A. F., Stone, P. R., Sergienko, A. V., Saleh, B. E. A. & Teich, M. C. Entangled-Photon Imaging of a Pure Phase Object. *Physical Review Letters* **93**, 213903. <https://link.aps.org/doi/10.1103/PhysRevLett.93.213903> (2020) (Nov. 2004).
71. Bornman, N., Prabhakar, S., Vallés, A., Leach, J. & Forbes, A. Ghost imaging with engineered quantum states by Hong–Ou–Mandel interference. *New Journal of Physics* **21**, 073044. <https://doi.org/10.1088%2F1367-2630%2Fab2f4d> (2020) (July 2019).
72. Pittman, T. B., Shih, Y. H., Strekalov, D. V. & Sergienko, A. V. Optical imaging by means of two-photon quantum entanglement. *Physical Review A* **52**, R3429–R3432. <https://link.aps.org/doi/10.1103/PhysRevA.52.R3429> (2019) (Nov. 1995).
73. Strekalov, D. V., Sergienko, A. V., Klyshko, D. N. & Shih, Y. H. Observation of Two-Photon “Ghost” Interference and Diffraction. *Physical Review Letters* **74**, 3600–3603. <https://link.aps.org/doi/10.1103/PhysRevLett.74.3600> (2019) (May 1995).
74. Aspden, R. S., Tasca, D. S., Boyd, R. W. & Padgett, M. J. EPR-based ghost imaging using a single-photon-sensitive camera. *New Journal of Physics* **15**, 073032. <https://doi.org/10.1088%2F1367-2630%2F15%2F7%2F073032> (2019) (July 2013).
75. Lane, T. J., Lane, T. J., Ratner, D. & Ratner, D. What are the advantages of ghost imaging? Multiplexing for x-ray and electron imaging. *Optics Express* **28**, 5898–5918. <https://www.osapublishing.org/oe/abstract.cfm?uri=oe-28-5-5898> (2020) (Mar. 2020).

76. Teich, M. C., Saleh, B. E. A., Wong, F. N. C. & Shapiro, J. H. Variations on the theme of quantum optical coherence tomography: a review. *Quantum Information Processing* **11**, 903–923. <https://doi.org/10.1007/s11128-011-0266-6> (2020) (Aug. 2012).
77. Mazurek, M. D., Schreier, K. M., Prevedel, R., Kaltenbaek, R. & Resch, K. J. Dispersion-cancelled biological imaging with quantum-inspired interferometry. *Scientific Reports* **3**, 1–5. <https://www.nature.com/articles/srep01582> (2020) (Apr. 2013).
78. Okano, M. *et al.* 0.54 μm resolution two-photon interference with dispersion cancellation for quantum optical coherence tomography. *Scientific Reports* **5**, 1–8. <https://www.nature.com/articles/srep18042> (2020) (Dec. 2015).
79. Giovannetti, V., Lloyd, S. & Maccone, L. Advances in quantum metrology. *Nature Photonics* **5**, 222–229. <https://www.nature.com/articles/nphoton.2011.35> (2020) (Apr. 2011).
80. Xiang, G. Y., Higgins, B. L., Berry, D. W., Wiseman, H. M. & Pryde, G. J. Entanglement-enhanced measurement of a completely unknown optical phase. *Nature Photonics* **5**, 43–47. <https://www.nature.com/articles/nphoton.2010.268> (2020) (Jan. 2011).
81. Okamoto, R. *et al.* Beating the standard quantum limit: Phase super-sensitivity of N-photon interferometers. *New Journal of Physics* **10**, 073033. <https://doi.org/10.1088%2F1367-2630%2F10%2F7%2F073033> (2020) (July 2008).
82. Stefanov, A. On the role of entanglement in two-photon metrology. *Quantum Science and Technology* **2**, 025004. <https://doi.org/10.1088%2F2058-9565%2Faa6ae1> (2020) (Apr. 2017).
83. Raymer, M. G., Marcus, A. H., Widom, J. R. & Vitullo, D. L. P. Entangled Photon-Pair Two-Dimensional Fluorescence Spectroscopy (EPP-2DFS). *The Journal of Physical Chemistry B* **117**, 15559–15575. <https://doi.org/10.1021/jp405829n> (2018) (Dec. 2013).
84. Otten, M., Kenneweg, T., Hensen, M., Gray, S. K. & Pfeiffer, W. Coherent photon coincidence spectroscopy of single quantum systems. *Physical Review A* **102**, 043118. <https://link.aps.org/doi/10.1103/PhysRevA.102.043118> (2023) (Oct. 2020).
85. Roslyak, O. & Mukamel, S. Multidimensional pump-probe spectroscopy with entangled twin-photon states. *Physical Review A* **79**, 063409. <https://link.aps.org/doi/10.1103/PhysRevA.79.063409> (2018) (June 2009).

86. Li, R. L. *et al.* Controlled growth of imine-linked two-dimensional covalent organic framework nanoparticles. *Chemical Science* **10**, 3796–3801. <https://pubs.rsc.org/en/content/articlelanding/2019/sc/c9sc00289h> (2023) (Mar. 2019).
87. Lachance-Quirion, D. *et al.* Entanglement-based single-shot detection of a single magnon with a superconducting qubit. *Science* **367**, 425–428. <https://science.sciencemag.org/content/367/6476/425> (2020) (Jan. 2020).
88. Dayan, B., Pe'er, A., Friesem, A. A. & Silberberg, Y. Two Photon Absorption and Coherent Control with Broadband Down-Converted Light. *Physical Review Letters* **93**, 023005. <https://link.aps.org/doi/10.1103/PhysRevLett.93.023005> (July 2004).
89. Schlawin, F., Dorfman, K. E., Fingerhut, B. P. & Mukamel, S. Suppression of population transport and control of exciton distributions by entangled photons. *Nature Communications* **4**, 1–7. <https://www.nature.com/articles/ncomms2802> (2019) (Apr. 2013).
90. Lever, F., Ramelow, S. & Gühr, M. Effects of time-energy correlation strength in molecular entangled photon spectroscopy. *Physical Review A* **100**, 053844. <https://link.aps.org/doi/10.1103/PhysRevA.100.053844> (2020) (Nov. 2019).
91. Oka, H. Entangled two-photon absorption spectroscopy for optically forbidden transition detection. *The Journal of Chemical Physics* **152**, 044106. <https://aip.scitation.org/doi/10.1063/1.5138691> (2020) (Jan. 2020).
92. Bergli, J., Adenier, G., Thörn, A. P. & Vistnes, A. I. Frequency and phase relations of entangled photons observed by a two-photon interference experiment. *Physical Review A* **100**, 023850. <https://link.aps.org/doi/10.1103/PhysRevA.100.023850> (2020) (Aug. 2019).
93. Burdick, R. K. *et al.* Predicting and Controlling Entangled Two-Photon Absorption in Diatomic Molecules. *The Journal of Physical Chemistry A* **122**, 8198–8212. <https://doi.org/10.1021/acs.jpca.8b07466> (2018) (Oct. 2018).
94. Pirandola, S., Bardhan, B. R., Gehring, T., Weedbrook, C. & Lloyd, S. Advances in photonic quantum sensing. *Nature Photonics* **12**, 724–733. <https://www.nature.com/articles/s41566-018-0301-6> (2020) (Dec. 2018).
95. Fan, W., Lawrie, B. J. & Pooser, R. C. Quantum plasmonic sensing. *Physical Review A* **92**, 053812. <https://link.aps.org/doi/10.1103/PhysRevA.92.053812> (2020) (Nov. 2015).

96. Pooser, R. C. & Lawrie, B. Plasmonic Trace Sensing below the Photon Shot Noise Limit. *ACS Photonics* **3**, 8–13. <https://doi.org/10.1021/acsp Photonics.5b00501> (2020) (Jan. 2016).
97. Lee, C. L. D. & Hewitt, K. C. First demonstration of surface enhanced-stimulated Raman spectroscopy (SE-SRS) using low-power CW sources. *Faraday Discussions* **205**, 227–232. <http://xlink.rsc.org/?DOI=C7FD00137A> (2020) (2017).
98. Oka, H. Highly-efficient entangled two-photon absorption with the assistance of plasmon nanoantenna. *Journal of Physics B: Atomic, Molecular and Optical Physics* **48**, 115503. <https://doi.org/10.1088%2F0953-4075%2F48%2F11%2F115503> (2020) (Apr. 2015).
99. Osaka, Y., Yokoshi, N., Nakatani, M. & Ishihara, H. Enhanced Up-Conversion of Entangled Photons and Quantum Interference under a Localized Field in Nanostructures. *Physical Review Letters* **112**, 133601. <https://link.aps.org/doi/10.1103/PhysRevLett.112.133601> (2020) (Apr. 2014).
100. Basiri-Esfahani, S., Myers, C. R., Armin, A., Combes, J. & Milburn, G. J. Integrated quantum photonic sensor based on Hong-Ou-Mandel interference. *Optics Express* **23**, 16008–16023. <https://www.osapublishing.org/oe/abstract.cfm?uri=oe-23-12-16008> (2020) (June 2015).
101. Lee, Y.-S., Lee, S. M., Kim, H. & Moon, H. S. Highly bright photon-pair generation in Doppler-broadened ladder-type atomic system. *Optics Express* **24**, 28083. <http://arxiv.org/abs/1609.02378> (2020) (Nov. 2016).
102. Kalashnikov, D. A., Pan, Z., Kuznetsov, A. I. & Krivitsky, L. A. Quantum Spectroscopy of Plasmonic Nanostructures. *Physical Review X* **4**, 011049. <https://link.aps.org/doi/10.1103/PhysRevX.4.011049> (2020) (Mar. 2014).
103. Roslyak, O., Marx, C. A. & Mukamel, S. Nonlinear spectroscopy with entangled photons: Manipulating quantum pathways of matter. *Physical Review A* **79**, 033832. <https://link.aps.org/doi/10.1103/PhysRevA.79.033832> (2018) (Mar. 2009).
104. Avanaki, K. N. & Schatz, G. C. Entangled Photon Resonance Energy Transfer in Arbitrary Media. *The Journal of Physical Chemistry Letters* **10**, 3181–3188. <https://doi.org/10.1021/acs.jpcllett.9b00902> (2020) (June 2019).
105. Pan, J.-W. *et al.* Multiphoton entanglement and interferometry. *Reviews of Modern Physics* **84**, 777–838. <https://link.aps.org/doi/10.1103/RevModPhys.84.777> (2018) (May 2012).
106. Mukamel, S. *et al.* Roadmap on Quantum Light Spectroscopy. *Journal of Physics B: Atomic, Molecular and Optical Physics*. <http://iopscience.iop.org/10.1088/1361-6455/ab69a8> (2020) (2020).

107. Gao, W. B., Fallahi, P., Togan, E., Miguel-Sanchez, J. & Imamoglu, A. Observation of entanglement between a quantum dot spin and a single photon. *Nature* **491**, 426–430. <https://www.nature.com/articles/nature11573> (2023) (Nov. 2012).
108. Bayer, M. *et al.* Coupling and Entangling of Quantum States in Quantum Dot Molecules. *Science* **291**, 451–453. <https://www.science.org/doi/10.1126/science.291.5503.451> (2023) (Jan. 2001).
109. Lee, K. C. *et al.* Entangling Macroscopic Diamonds at Room Temperature. *Science* **334**, 1253–1256. <http://science.sciencemag.org/content/334/6060/1253> (2021) (Dec. 2011).
110. Muthukrishnan, A., Agarwal, G. S. & Scully, M. O. Inducing Disallowed Two-Atom Transitions with Temporally Entangled Photons. *Physical Review Letters* **93**, 093002. <https://link.aps.org/doi/10.1103/PhysRevLett.93.093002> (2023) (Aug. 2004).
111. Prochaska, L. *et al.* Singular charge fluctuations at a magnetic quantum critical point. *Science* **367**, 285–288. <https://www.science.org/doi/10.1126/science.aag1595> (2023) (Jan. 2020).
112. Bouwmeester, D. & Zeilinger, A. in *The Physics of Quantum Information: Quantum Cryptography, Quantum Teleportation, Quantum Computation* (eds Bouwmeester, D., Ekert, A. & Zeilinger, A.) 1–14 (Springer, Berlin, Heidelberg, 2000). ISBN: 978-3-662-04209-0. https://doi.org/10.1007/978-3-662-04209-0_1 (2023).
113. Kimble, H. J. The quantum internet. *Nature* **453**, 1023–1030. <https://www.nature.com/articles/nature07127> (2023) (June 2008).
114. Chang, D. E., Douglas, J. S., González-Tudela, A., Hung, C.-L. & Kimble, H. J. Colloquium: Quantum matter built from nanoscopic lattices of atoms and photons. *Reviews of Modern Physics* **90**, 031002. <https://link.aps.org/doi/10.1103/RevModPhys.90.031002> (2023) (Aug. 2018).
115. Keimer, B. & Moore, J. E. The physics of quantum materials. *Nature Physics* **13**, 1045–1055. <https://www.nature.com/articles/nphys4302> (2023) (Nov. 2017).
116. Jones, R. O. Density functional theory: Its origins, rise to prominence, and future. *Reviews of Modern Physics* **87**, 897–923. <https://link.aps.org/doi/10.1103/RevModPhys.87.897> (2023) (Aug. 2015).
117. Scalapino, D. J. A common thread: The pairing interaction for unconventional superconductors. *Reviews of Modern Physics* **84**, 1383–1417. <https://link.aps.org/doi/10.1103/RevModPhys.84.1383> (2023) (Oct. 2012).

118. Löhneysen, H. v., Rosch, A., Vojta, M. & Wölfle, P. Fermi-liquid instabilities at magnetic quantum phase transitions. *Reviews of Modern Physics* **79**, 1015–1075. <https://link.aps.org/doi/10.1103/RevModPhys.79.1015> (2023) (Aug. 2007).
119. Basov, D. N., Averitt, R. D., van der Marel, D., Dressel, M. & Haule, K. Electrodynamics of correlated electron materials. *Reviews of Modern Physics* **83**, 471–541. <https://link.aps.org/doi/10.1103/RevModPhys.83.471> (2023) (June 2011).
120. Bloch, I., Dalibard, J. & Nascimbène, S. Quantum simulations with ultracold quantum gases. *Nature Physics* **8**, 267–276. <https://www.nature.com/articles/nphys2259> (2023) (Apr. 2012).
121. Dorfman, K. E. & Mukamel, S. Multidimensional spectroscopy with entangled light: loop vs ladder delay scanning protocols. *New Journal of Physics* **16**, 033013. <https://doi.org/10.1088%2F1367-2630%2F16%2F3%2F033013> (2020) (Mar. 2014).
122. Altuzarra, C. *et al.* Coherent Perfect Absorption in Metamaterials with Entangled Photons. *ACS Photonics* **4**, 2124–2128. <https://doi.org/10.1021/acsphotonics.7b00514> (2023) (Sept. 2017).
123. Li, Y., Nemilentsau, A. & Argyropoulos, C. Resonance energy transfer and quantum entanglement mediated by epsilon-near-zero and other plasmonic waveguide systems. *Nanoscale* **11**, 14635–14647. <https://pubs.rsc.org/en/content/articlelanding/2019/nr/c9nr05083c> (2023) (Aug. 2019).
124. Basov, D. N., Averitt, R. D. & Hsieh, D. Towards properties on demand in quantum materials. *Nature Materials* **16**, 1077–1088. <https://www.nature.com/articles/nmat5017> (2023) (Nov. 2017).
125. Mak, K. F., He, K., Shan, J. & Heinz, T. F. Control of valley polarization in monolayer MoS₂ by optical helicity. *Nature Nanotechnology* **7**, 494–498. <https://www.nature.com/articles/nnano.2012.96> (2023) (Aug. 2012).
126. Xu, X., Yao, W., Xiao, D. & Heinz, T. F. Spin and pseudospins in layered transition metal dichalcogenides. *Nature Physics* **10**, 343–350. <https://www.nature.com/articles/nphys2942> (2023) (May 2014).
127. Boto, A. N. *et al.* Quantum Interferometric Optical Lithography: Exploiting Entanglement to Beat the Diffraction Limit. *Physical Review Letters* **85**, 2733–2736. <https://link.aps.org/doi/10.1103/PhysRevLett.85.2733> (2022) (Sept. 2000).

*Chapter 3***DESIGNING HIGH-POWER, OCTAVE SPANNING ENTANGLED
PHOTON SOURCES FOR QUANTUM SPECTROSCOPY**

ABSTRACT

Entangled photon spectroscopy is a nascent field that has important implications for measurement and imaging across chemical, biology, and materials fields. Entangled photon spectroscopy potentially offers improved spatial and temporal-frequency resolutions, increased cross sections for multiphoton and nonlinear measurements, and new abilities in inducing or measuring quantum correlations. A critical step in enabling entangled photon spectroscopies is the creation of high-flux entangled sources that can use conventional detectors, as well as provide redundancy for the losses in realistic samples. Here, we report a periodically poled, chirped, lithium tantalate platform that generates entangled photon pairs with a $\sim 10^{-7}$ efficiency. For a near watt level diode laser, this results in a near μW -level flux. The single photon per mode limit that is necessary to maintain non-classical photon behavior is still satisfied by distributing this power over up to an octave-spanning bandwidth. The spectral-temporal photon correlations are observed via a Michelson-type interferometer that measures the broadband Hong-Ou-Mandel two-photon interference. A coherence time of 245 fs for a 10 nm bandwidth in the collinear case and a 62 fs for a 125 nm bandwidth in the non-collinear case is measured using a CW pump laser, and, essentially, collecting the full photon cone. We outline in detail the numerical methods used for designing and tailoring the entangled photons source, such as changing center wavelength or bandwidth, with the ultimate aim of increasing the availability of high-flux UV-Vis entangled photon sources in the optical spectroscopy community.

Most of this chapter has been reproduced with permission from:

Szoke, S. *et al.* Designing high-power, octave spanning entangled photon sources for quantum spectroscopy. *The Journal of Chemical Physics* **154**. Publisher: American Institute of Physics, 244201. ISSN: 0021-9606. <https://aip.scitation.org/doi/10.1063/5.0053688> (2021) (June 2021).

3.1 Introduction

An entangled photon pair is generated by splitting a single photon into two photons via spontaneous parametric down conversion (SPDC) [1]. The quantum correlations between the two photons have several effects. First, when coherently recombined in time and space, the two entangled photons behave as the initial pump photon. In other words, the two entangled photons can be thought of as acting like a single photon in light-matter interactions [2]. As a result, two entangled photons leave the same side of a beamsplitter [3] and diffract from a grating at the wavelength of the pump photon [4–6]. Entangled photon pairs also linearize multiphoton and nonlinear spectroscopy, as has been well-studied in two-photon absorption and fluorescence [7–13]. Entangled photons also have non-Fourier reciprocal spectral-temporal resolutions and are able to yield spatial resolutions which scale inversely with the number of correlated entangled photons N [14–18].

These properties, plus the more well known sub-shot noise and classical light rejection behaviors, make entangled photons tempting for use in ultrafast laser spectroscopy [19, 20]. The fragility of the entangled states, and the difficulty and expense associated with single photon counting, necessitates a need for high flux (nW- μ W) entangled photon sources that would easily interface with existing ultrafast optics setups [21]. However, commonly used nonlinear crystals (BBO, KDP), usually have entangled photon creation efficiencies in the 10^{-10} to 10^{-12} range [22–24]. Reliance on ‘birefringent phase matching’ limits the highest usable nonlinear coefficients of the crystal as well as the bandwidth of entangled photons that can be created [25–27]. The possible phase-matching conditions result in bandwidths in the tens of nanometers range, which corresponds to 100s of femtoseconds to picoseconds in correlation times in experiments. Given the current assumption that the entangled photon correlation time must be less than a molecule or material’s de-phasing time to allow a nonlinear or multiphoton enhancement, the narrow bandwidth of birefringent phase matching presents critical limits on entangled spectroscopy’s feasibility [19, 28, 29].

In contrast, the ferroelectric properties of materials such as KTP and lithium niobate allow the crystals to be periodically poled and utilize a ‘quasi phase-matching’ (QPM) technique [30–32]. Quasi-phase-matching allows the use of Type-0 collinear phase matching [33], SPDC efficiencies of 10^{-6} to 10^{-10} [34, 35], a broadly tunable center wavelength (set by the grating period instead of crystal angle) [36], and easy implementation of waveguides that can saturate single photon detectors with

~mW of CW diode laser input power [37]. Broad bandwidth phase matching is achieved by introducing a chirp into the poling period of the structure. The nonlinear poling allows for more wavelengths to be phase matched, while also retaining the benefits associated with longer crystals, namely a larger downconverted photon flux. The increased bandwidth directly affects the effective temporal resolution of experiments [38–40]. The broad bandwidth also allows increased power densities, as the single photon per wavelength mode occupation limit necessary for non-classical effects is not exceeded (calculated as the flux in photons/s divided by the bandwidth in Hz) [41, 42]. While KTP and lithium niobate have been the primary workhorse for entangled photon generation in quantum information system settings, they have limitations with regards to their damage thresholds and UV cut-offs. In contrast, lithium tantalate is more ideal for physical chemistry and materials research because it has higher power handling capabilities (240 MW/cm^2) [43] and a lower UV absorption edge ($\approx 280 \text{ nm}$) [44, 45].

To accelerate the adoption of entangled photon techniques, we outline how to create an entangled photon source that can achieve near μW powers of entangled photons down to UV wavelengths with temporal resolutions of tens of femtoseconds. These entangled photon fluxes are high enough to be visible by eye when starting from a 1 W CW pump laser, greatly facilitating the alignment of entangled experiments. Here, the generated photon pairs are centered around a degenerate wavelength of 812 nm, resulting from a 406 nm pump source, but this wavelength can be tuned as outlined by the formulas in the paper. The 8% MgO doped congruent lithium tantalate (CLT) gratings use a Type-0, collinear quasi-phase matching configuration. A Michelson type interferometric scheme [46] measures the fourth-order interference of the entangled photons and gives coherence times of 245 fs for a bandwidth of 10 nm and 62 fs for a bandwidth of 125 nm. Of course, simply producing a broad bandwidth of entangled photons is not the same as carrying out experiments using them. We discuss our attempts to utilize the full SPDC cone and bandwidth in subsequent experiments, emphasizing where optics development is still needed to achieve maximum temporal resolution and flux. Using the full cone is in contrast to most experiments where irises are used to select two points from the SPDC cone, thereby severely reducing the total photon flux at the gain of state purity. The paper aims to give quick access to the sources needed for the emerging field of nonlinear entangled photon optics as well as outlining the next steps needed in the field.

3.2 Theory

Designing broadband SPDC in a chirped nonlinear materials

Prior to quantifying the experimental behavior of the SPDC sources, we lay out the theoretical and numerical details used in their design.

In SPDC, the creation of two entangled photons arises from the quantum mechanical process of a single pump photon mixing with the underlying vacuum state. The two down-converted daughter photons display strong correlations in time, energy, and momentum due to the parametric mixing process [1, 47]. The time and energy correlations originate from the individual photons being generated simultaneously from the pump photon:

$$E_p(\omega_p) = E_s(\omega_s) + E_i(\omega_i) \quad (3.1)$$

$$\therefore \omega_i = \omega_p - \omega_s \quad (3.2)$$

where ω_p , ω_s , and ω_i are the frequencies of the pump, signal, and idler photon, respectively. The momentum correlation is dictated by the phase matching condition, which is a consequence of the wave-like nature of the interacting fields. Each field has a corresponding wave vector defined via its respective phase velocity $v_p = c/n(\omega, T)$ in the medium:

$$k(\omega, T) = \frac{\omega n(\omega, T)}{c} \quad (3.3)$$

with $n(\omega, T)$ being the frequency and temperature dependent refractive index of the material. The following vector sum, the longitudinal component of which is depicted in Fig. 3.1, should be satisfied in order to ensure that a proper phase relationship between the interacting waves is maintained throughout the nonlinear crystal.

$$\Delta \mathbf{k}(\omega_p, \omega_s, \omega_i) = \mathbf{k}_p(\omega_p, n_p(\omega_p, T)) - \mathbf{k}_s(\omega_s, n_s(\omega_s, T)) - \mathbf{k}_i(\omega_i, n_i(\omega_i, T)). \quad (3.4)$$

It is only when this relationship holds true ($\Delta k = 0$) that constructive interference between the propagating waves can occur and energy is transferred dominantly in one direction, rather than oscillating back and forth between the two optical modes [48].

A natural extension of this phase-matching principle, termed quasi-phase-matching, is apparent if one considers the duality between position and momentum space.

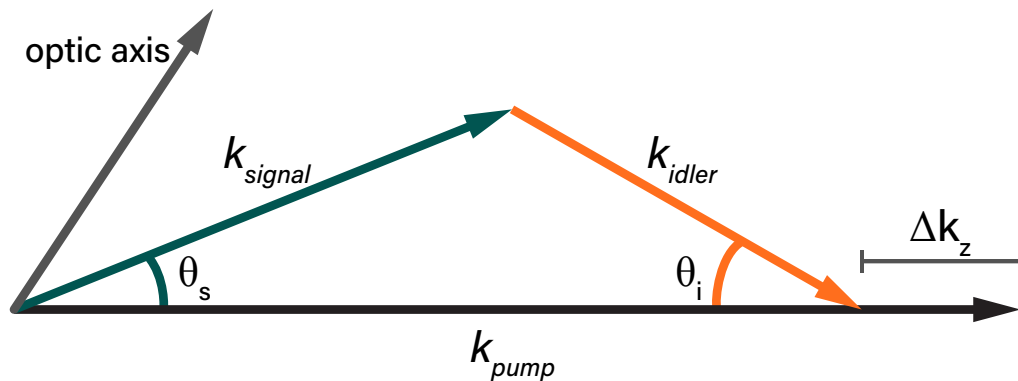


Figure 3.1: Phase-matching diagram for a two-photon down conversion process, showing the longitudinal phase-mismatch component Δk_z . The entangled photons (signal and idler) are each shown to have their distinct wave vectors k and emission angles θ . The phase-mismatch component must be compensated to create entangled photons by spontaneous parametric down conversion (SPDC).

A periodic lattice in position space directly corresponds to a well-defined wave vector k in momentum space via a Fourier transform. Therefore, if the nonlinear dielectric tensor domains of ferroelectric nonlinear crystal are modulated with a specific periodicity Λ , a quasi-momentum term $\Gamma(\Lambda)$ arises, which can be used to satisfy a non-phase-matched nonlinear interaction.

$$\Delta \tilde{k}(\omega_p, \omega_s, \omega_i) = \Delta k(\omega_p, \omega_s, \omega_i) - \Gamma(\Lambda) \quad (3.5)$$

The quasi-phase-matching term $\Gamma(\Lambda)$ also has an additional advantage, in that it can be chosen to be higher-order. Here, the order of the configuration is defined by m .

$$\Gamma(\Lambda) = \frac{2\pi m}{\Lambda}, \quad m \in 2\mathbb{Z} + 1 \quad (-0) \quad (3.6)$$

This serves a particular experimental benefit as it allows for nonlinear interactions to be phase-matched (albeit with lower efficiency), even if the required 1st order periodicity is too small to be fabricated [49].

We now describe the design of a grating in congruent lithium tantalate with the design goal of a 406 nm pump wavelength that creates a >400 nm bandwidth around the degenerate 812 nm SPDC point. The source must also be capable of creating near μW powers given a 1 W input power. The first step is to obtain the Sellmeier equations that describe the frequency and temperature dependent refractive indices of the material [50]. The numeric values and a representative plot are found in the supplementary information. Using the Sellmeier equations, the

phase mismatch (Eq. 3.5) is then evaluated for a wide range of pump-signal/idler wavelength configurations while keeping one entangled photon frequency a constant. External conditions such as the desired temperature range and minimum achievable poling periodicity are also enforced such that the parameter space remains within experimentally realistic boundaries. The root of Eq. 3.5 can then be found by a root-finding algorithm. For the congruent lithium tantalate and a 406-812 SPDC process, and imposing a realistic $< 200^{\circ}\text{C}$ temperature condition, solving for the root of Eq. 3.5 yields a poling period of $9.5 \mu\text{m}$ at 133°C (see fig. A.2 for the graphical solution).

Quasi-phase-matching is a strongly temperature dependent technique. By solving Eq. 3.5 for a range of temperatures near the calculated degeneracy point (133°C), the splitting and tuning of the SPDC spectrum can be calculated. Tuning the SPDC spectrum via the crystal temperature is useful for controlling what intermediate states are involved in, the magnitude of, and the temporal resolution of an entangled two photon process. The temperature dependent behavior is shown in Fig. 3.2. Here, the transition between the degenerate and non-degenerate domains is clearly observable, with lower temperatures corresponding to a weaker degenerate emission profile. The lower plot of Fig. 3.2 also clearly shows a very strong narrowing of the signal and idler bandwidths as one temperature tunes further away from degeneracy.

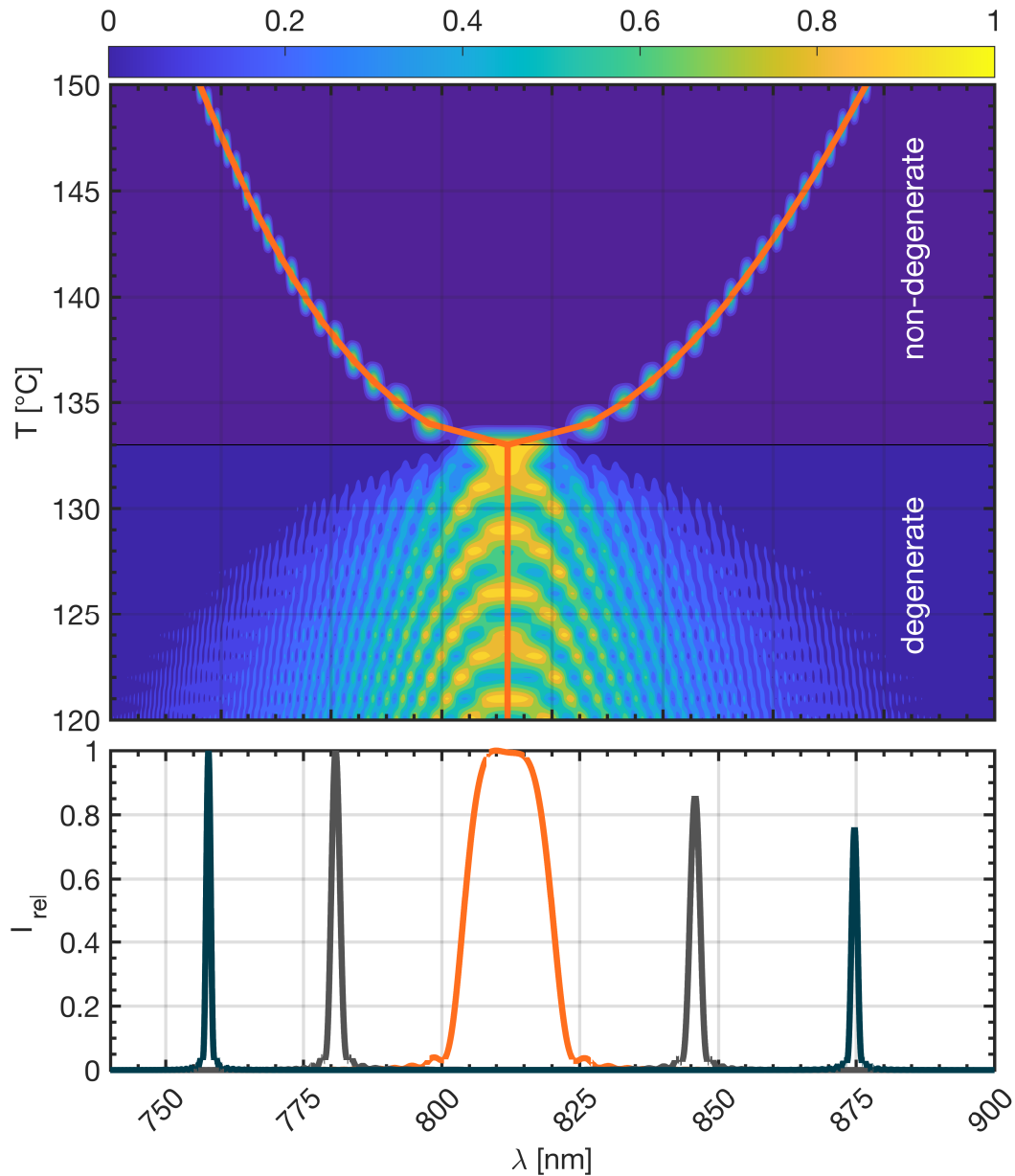


Figure 3.2: SPDC emission spectrum for ppCLT at various phase-matching temperatures showing transition from degenerate to non-degenerate down conversion. Bottom plot showing spectra at three temperatures corresponding to cross sections of the 2D plot. The phase matching temperature results in the broadest bandwidth.

Additionally, both signal and idler have an inherent angular emission property determined by the momentum conservation condition in Eq. 3.5. The strong frequency dependence of the outgoing angles can be numerically calculated from the momentum conservation equation if one decomposes the wave vectors into their longitudinal and transverse components, and solves the trigonometric equations for

transverse phase-matching. Subsequently computing the emission angle for each frequency of interest, in conjunction with the frequency dependent refractive index of the nonlinear crystal, the SPDC cone's spectral characteristic for various crystal temperatures can be plotted (Fig. 3.3). As predicted, at the degenerate emission temperature of 133°C, the plot shows that the emission angle of the 812 nm signal and idler photons is 0°C. More importantly however, comparing the results to those in Fig. 3.2, the shaded non-degenerate region also corresponds to a collinear emission profile. Vice versa, temperatures below 133°C display a (albeit weak) degenerate, non-collinear character.

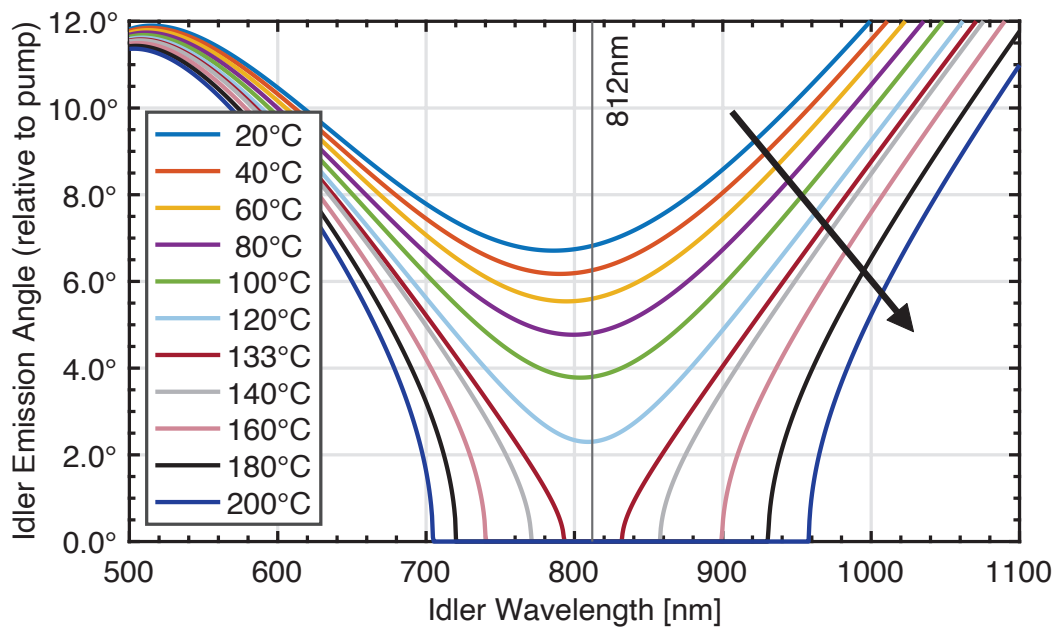


Figure 3.3: Broadband signal/idler emission angles in ppCLT with 9.5 μm poling period, showing how the SPDC source does not act as an ideal dipole emitter when broadband entangled photon pairs are desired. Points where curves reach a value of zero correspond to collinear, non-degenerate emission. Note that at certain temperatures, there need not be any SPDC emission in certain directions, governed by the spectral emission characteristics in Fig. 3.2. Arrow indicating direction of increasing temperature.

In a chirped crystal, the bandwidth of the down-converted entangled photons is increased by changing the poling period throughout the crystal. The increasing width elements correspond to different phase-matched wavelength configurations of Eq. 3.5 (Fig. 3.4). The photons still add up to the narrow linewidth of the pump laser but the temporal resolution is given by the temporal alignment and down-converted bandwidth of the entangled photons. This is why entangled photon experiments

are said to have independent spectral and temporal resolutions. The importance of the pump laser's linewidth in determining the entangled photon state's purity, and thus the access to non-classical spectroscopic properties, is discussed in the supplementary information.

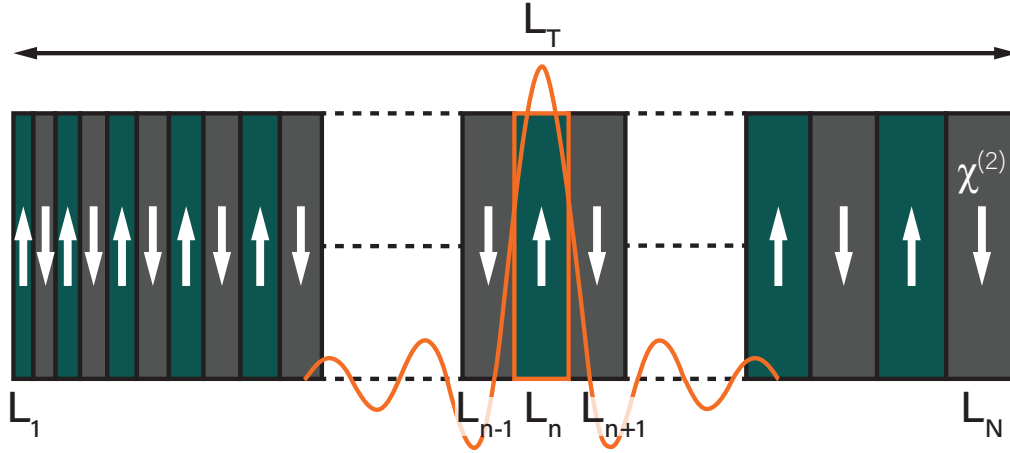


Figure 3.4: Depiction of a chirped periodically poled crystal with total length L_T . Each crystal segment of length L_n is associated with a *sinc*-shaped downconversion amplitude around a different center wavelength. Equivalently to a normal periodically poled crystal, the domain orientation is reversed in adjacent elements.

Following a similar treatment to [51], the crystal can be decomposed into its individual domains, in each of which the downconversion amplitude follows the usual *sinc* function-like phase-matching dependence [52]. This is attributed to the Fourier transform of a rectangular function in real-space representing the probability of a downconversion event occurring inside the crystal element.

$$A_n(\omega_s, \omega_i) = L_n \text{sinc}\left(\frac{L_n \Delta k}{2}\right) \quad (3.7)$$

With L_n being the length of the n^{th} crystal element. Similarly, a cumulative-phase term can be defined, which is related to a forward propagating wave with phase-mismatch Δk traversing a crystal length L_{prop} after it has been generated in the SPDC process at crystal element n .

$$\varphi = \Delta k L_{prop} = \Delta k \left(\frac{L_n}{2} + \sum_{m=n+1}^N L_m \right) \quad (3.8)$$

Carrying out a sum over all individual crystal elements then allows for the resulting SPDC spectrum to be calculated (Eq. 3.9) and thereby observe the effects of different

chirping parameters. For lithium tantalate, this is shown in Fig. 3.5. In the case of CLT, a $\pm 10\%$ chirp around the degenerate poling periodicity calculated above yields a full octave spanning SPDC bandwidth. Trivially, in the limit of no chirp, where all crystal elements are equal in size, the solution for a periodically poled crystal of length L is recovered.

$$A(\omega_s, \omega_i) = \chi_0 \sum_{n=1}^N (-1)^n L_n \text{sinc}\left(\frac{L_n \Delta k}{2}\right) \times e^{-i\Delta k\left(\frac{L_n}{2} + \sum_{m=n+1}^N L_m\right)}. \quad (3.9)$$

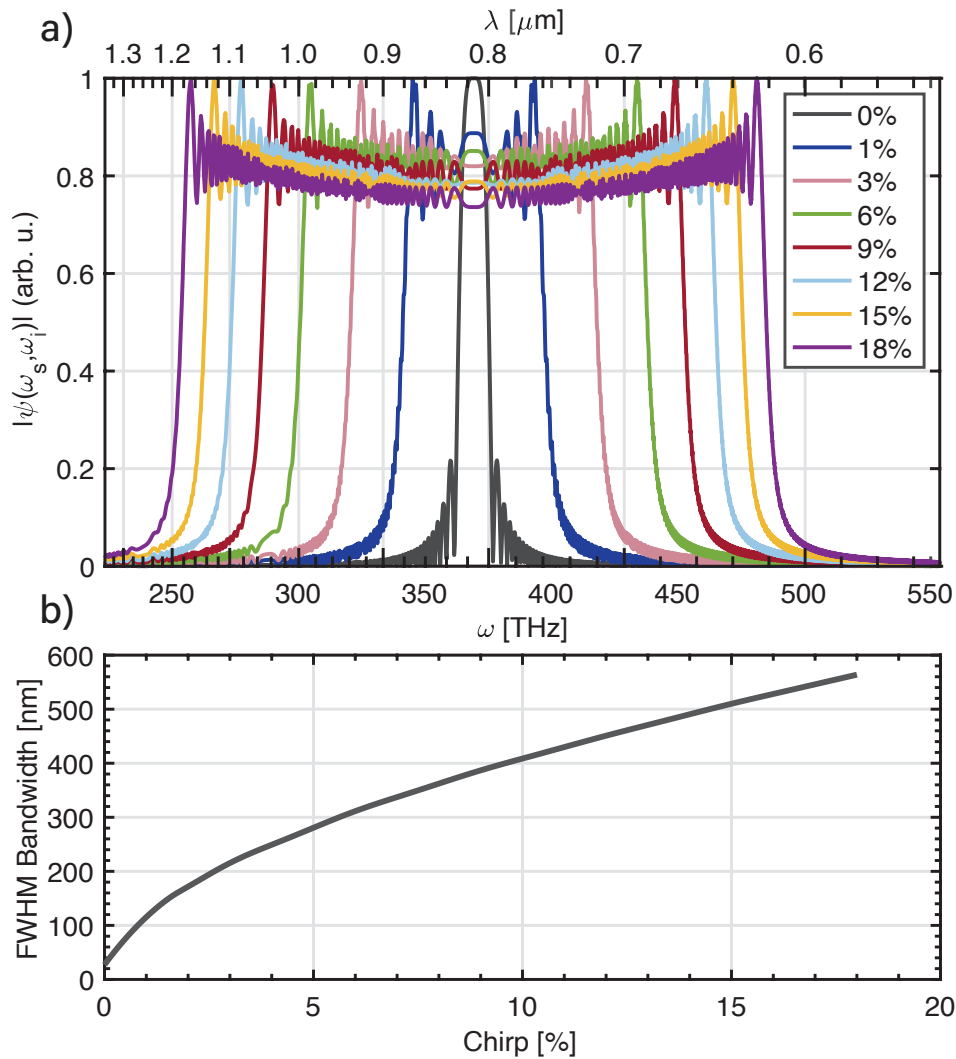


Figure 3.5: SPDC emission bandwidth broadening. (a) SPDC emission bandwidth broadening as a function of chirp parameter, defined as total percentage deviation from the degenerate poling period. (b) Numerically calculated FWHM bandwidth trend as a function of poling period chirp.

By plotting the solution of Eq. 3.9 as a function of the position inside the crystal along the propagation direction, we can gain some intuition for how the constructive interference results in a broadened spectrum. In the case of CLT, a $\pm 10\%$ chirp around the degenerate poling periodicity calculated above yields a full octave spanning SPDC bandwidth as shown in Fig. 3.6. Here we used a total grating length of 18 mm equal to the chip used in subsequent experiments.

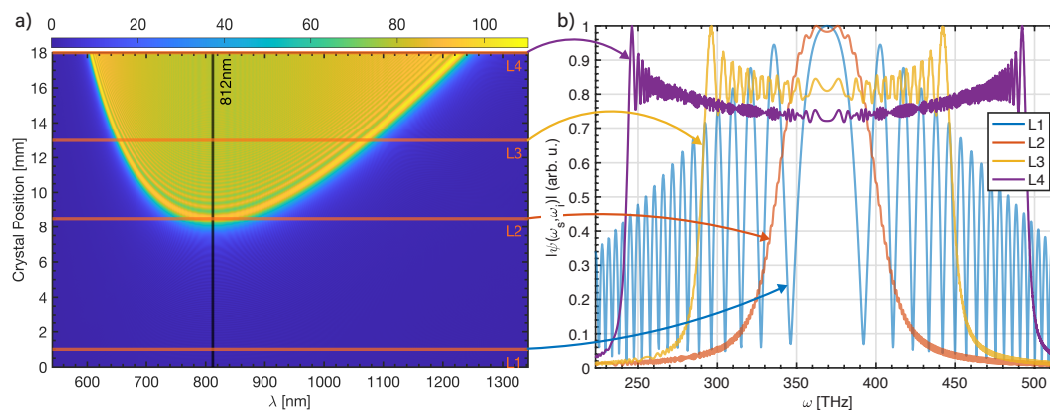


Figure 3.6: SPDC buildup in a ppCLT grating. (a) Build up of the collective SPDC spectrum as a function of the position inside a chirped ppCLT grating in the direction of propagation. (b) Line cuts across the 2D spectrum plot in (a) showing the normalized spectrum (in frequency space) at the positions designated as L1, L2, L3, and L4, respectively.

The 2D plot in Fig. 3.6 provides some additional insight into how modulation of the poling period affects the build-up of the emitted spectrum. In particular, it's important to note that while the first 8mm length of the crystal appears to show no downconversion taking place, this is indeed not the case. While all crystal elements in this region satisfy a particular phase-matching condition, it is only after a certain propagation length that the phases of each spectral mode coherently sum to a strong enough amplitude that would be perceivable on the plot. Furthermore, the broadening of the downconverted bandwidth does have a particular drawback, in that the frequencies close to degeneracy become weaker in intensity. This is best observed in the line cuts for positions L3 and L4, where instead of a constant intensity across all frequencies, the emission spectrum peaks at the lower and higher cut-offs but begins to droop more severely as the bandwidth increases. Thus, increasing the chirping of the poling period indefinitely does not necessarily yield a flat power spectral density. It should be pointed out that this issue can be addressed via chirp profiles which follow not a linear but some higher order functional form [53].

In contrast to narrowband SPDC where the emission angles for the photon pairs are well confined within the two narrow arcs satisfying momentum conservation, such extremely broadband downconversion poses inherent difficulties in the spatial degree of freedom due angular (chromatic) dispersion of the resulting beam. As Fig. 3.3 shows, the emission angles increase quickly away from degeneracy. This presents several experimental issues, as the beam no longer represents an ideal point source, which will be discussed in the experimental section below. Taking into account the physical dimensions of the grating cross section (detailed in the experimental section below), it is easy to see that the output aperture of the grating can at most only accommodate $\arctan(0.15 \text{ mm}/9 \text{ mm}) \approx 1^\circ$ of emission in the horizontal axis, and $\arctan(0.5 \text{ mm}/9 \text{ mm}) \approx 3.2^\circ$ along the vertical axis relative to the center point of the crystal where we focus. Beyond this, large parts of the SPDC emission cone will begin to interact with the domain boundaries which form the grating channel. While in principle the refractive index is the same for both un-poled and poled crystal regions, the periodic poling process causes some stress at the domain walls. Therefore, the edge of the each pattern in the lateral direction acts as a kind of scattering center, possibly resulting in unwanted interference patterns. Therefore special attention should be paid to accommodate the spatial distribution of the cone as it diverges inside the channel.

A final point to consider is the total length of the grating is to be chosen by considering two interlinked criteria. Firstly, the expected power spectral density of the entangled photons at the output scales as L^2 . Emission intensity can therefore be significantly increased by utilizing longer structures. Conversely, the expected power spectral density also depends on a $\text{sinc}\left(\frac{L_n \Delta k}{2}\right)$ multiplicative factor. Hence, longer gratings result in narrower emission bandwidths. This ‘dual’-argument also applies to poling patterns which have a chirp, as while increasing the amount of variation in the poling periodicity serves to broaden the emission bandwidth, each spectral component will be less populated with photons and thus less brilliant. Particularly for entangled photon spectroscopy, the optimal flux is around the single photon per mode limit. Above this, the quantum and entangled effects will start to blur out due to classical effects. So, to maximize the entangled flux such that it remains within the single photon per mode limit, it is crucial that higher total fluxes (due to increased grating lengths) are spread out across broader bandwidths (via stronger chirps). An unchirped or bulk crystal will blur out quantum effects quicker than the chirped crystal with increasing length. The length reported here is to balance these effects.

3.3 Experiment and results

SPDC Characterization

The periodically poled congruent lithium tantalate gratings were manufactured by HC Photonics. The unchirped chip consists of 8 gratings with different poling periods (8.5, 9, 9.5, 10, 10.5, 11, 11.5, 12 μm). It is 20 mm long and each channel has a 0.9 mm by 0.5 mm cross section. The chirped chip consists of 6 gratings with varying chirp parameters and entrance poling periods (Table 3.1). Each grating is 18 mm long and has a 1 mm by 0.3 mm cross section. The gratings are AR-coated on both input and output faces at 406 nm ($R < 0.5\%$)/812 nm ($R < 0.5\%$).

Grating	$\Lambda_1[\mu\text{m}]$	$\Lambda_c[\mu\text{m}]$	$\Lambda_2[\mu\text{m}]$	Chirp
1	9.000	9.45	9.900	10%
2	9.048	9.50	9.952	10%
3	9.095	9.55	10.005	10%
4	9.143	9.60	10.057	10%
5	9.190	9.65	10.110	10%
6	9.238	9.70	10.162	10%

Table 3.1: Chip parameters

The experimental setup, as illustrated in Fig. 3.8, consisted of a computer-tunable, CW Ti:Sapphire laser (M2 SolsTiS) and an external SHG cavity to act as the pump source. The maximal output power of the SHG at 406 nm was 1.15 W with a 0.89 nm linewidth. The pump beam is focused through the ppCLT grating using an aspheric lens with a 40 cm focal length. This focal length is chosen such that the size of the focused beam was smaller than the grating's cross sectional dimension and further optimized for peak SPDC brightness. The position of the crystal can be finely adjusted in the XYZ directions using a piezoelectric stage, which is critical for maximizing the entangled photon flux. The angular deviation of the grating's long axis relative to the input beam was not as crucial as the X-Y centering of the chip around the focused beam and the z-control over exact focal point positioning. The temperature of the crystal is controlled by a ceramic heater and PID loop (Covesion) to an accuracy of 10 mK.

To measure the SPDC spectrum as well as the power of the downconverted flux, the output of the grating is passed through a total of three OD-4 500 nm longpass filters (Edmund Optics) to eliminate the residual 406 nm pump. The SPDC cone is collimated with an off-axis parabolic mirror and then focused into a USB spectrometer (Thorlabs). For more detailed characterization, the SPDC cone is collimated

with a telephoto lens and then focused into a spectrometer (Princeton Instruments IsoPlane) with a 15cm focal length lens. In this configuration, spectral and power measurements are performed with an electron multiplying intensified CCD camera (emICCD, Princeton Instruments MAX4). For the broadband spectral measurements, spectra are collected and stitched together as a 800 nm blazed grating with 150 grooves/mm is scanned across several center wavelengths. These spectra are then background corrected, quantum efficiency corrected according to the detection efficiency of the emICCD camera, and normalized.

Fig. 3.7 (a) depicts the SPDC spectra for the $9.50 \mu\text{m}$ unchirped grating as the temperature of the crystal is varied from 60°C to 160°C . Above 150°C , the shift from degenerate to non-degenerate emission conditions is apparent from the decrease in intensity around the degenerate wavelength region of 812 nm (gray dashed line). In comparison, as shown in Fig. 3.7 (b), at 145°C , the chirped chip (blue curve) exhibits much broader and flatter emission than the unchirped counterpart (red curve). The ratio of the flux produced by the chirped grating to that produced by the unchirped grating is ~ 1.7 . This increased flux is due to the lower wavelength components, as shown in Fig. 3.7b. The occupation per spatial mode was not estimated here because of the difficulty of collimating the full SPDC cone.

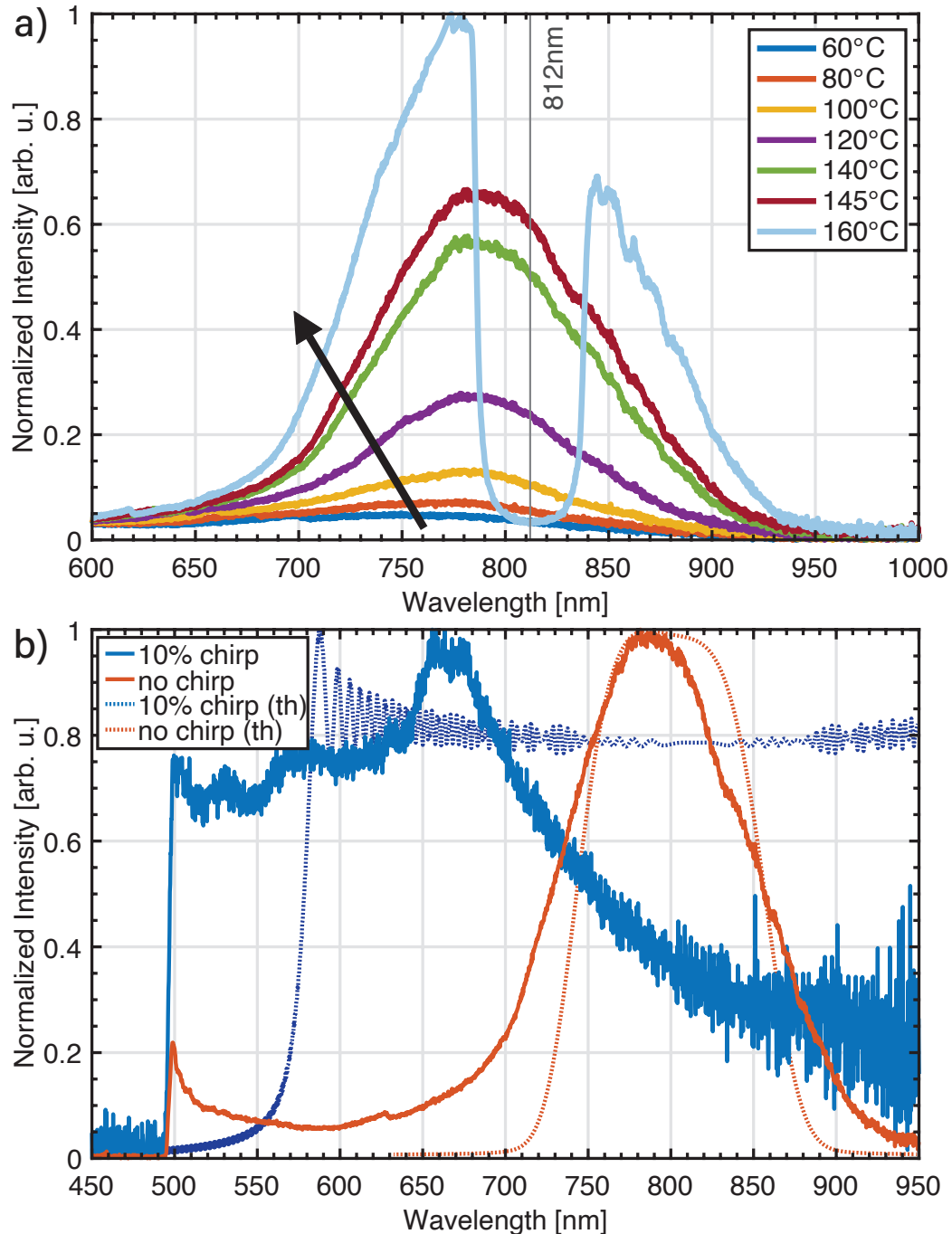


Figure 3.7: Simulated and measured SPDC spectra for chirped and unchirped gratings. (a) SPDC spectra for a 9.50 μm unchirped grating, gray reference line marks the degenerate wavelength of 812 nm. Arrow a guide in the direction of increasing temperature. (b) Experimental (solid) and theoretical (dashed) SPDC spectra for a chirped grating with a 9.50 μm center poling period and 10% chirp rate. Both spectra taken at a temperature of 145°C. The chirped emission is broader and has a flatter top than the unchirped emission. Note the detector cut-off at 900 nm.

Two-Photon Interference

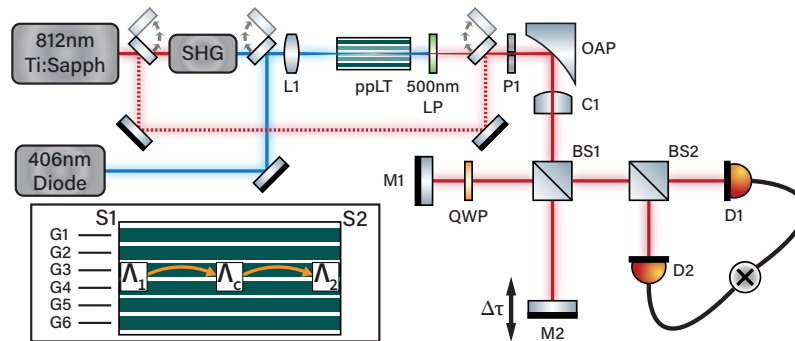


Figure 3.8: Entangled photon pair Michelson interferometer used to measure the fourth order interference. SHG: second harmonic generation unit, L1: focusing lens, ppLT: periodically poled lithium tantalate chip, LP: longpass filter, OAP: off-axis parabolic mirror, C1: cylindrical lens, BS1 and BS2: 50:50 beamsplitters, M1 and M2: mirrors, QWP: quarter-wave plate, D1 and D2: multimode fiber coupled single photon avalanche diodes connected to coincidence counting unit. The flip mirrors allow re-configuring such that the Ti:Sapph output is picked off and used for aid in alignment of downstream optics. A 406 nm diode laser is used as an alternate pump source. (Inset) Chip diagram showing the grating layout and their corresponding entrance (Λ_1), center (Λ_c), and end (Λ_2) poling periodicity locations in reference to Table.3.1.

The fourth-order interference between entangled photon pairs was quantified with a two-photon Michelson interferometer, depicted in Fig. 3.8. The Michelson interferometer is chosen because the configuration allows a broader bandwidth of the SPDC cone to be easily utilized, in contrast to a Mach-Zehnder configuration. Following the end of the ppLT chip, the entangled photons are collimated with an off-axis parabolic mirror and a cylindrical lens. These photons are directed through a broadband nonpolarizing 50:50 beamsplitter (BS1, Layertec) which separates the incident photons into two paths. In the reflected path, the photons pass through an achromatic quarter-wave plate (Thorlabs) twice to rotate their polarizations. The optical path length difference between the two arms is adjusted by scanning a mirror mounted to a linear stage in the transmitted arm. Coincidence counts vs. optical path length difference are then collected at one of the output arms of BS1. The coincidence counting setup consists of a second broadband 50:50 beamsplitter (BS2, Layertec), and two free-space-to-fiber coupling setups connecting to single-photon avalanche diodes (SPADs, Laser Component COUNT) and time-tagging electronics (PicoHarp 300). Because of the high SPDC flux, the pump beam must first be dimmed by three orders of magnitude to avoid SPAD saturation (counting

rate 10^6 photons/s). Full counting rate experiments can be completed using the CCD alone [54, 55] but were not implemented at the time of writing this paper.

The free-space-to-fiber coupling setups each consist of 2 mirrors to align the beam-splitter outputs through a 4.51 mm focal length asphere, which then focuses the beam into a multimode fiber ($105\mu\text{m}$ core diameter, 0.22 NA) connected to the SPADs. For these measurements, the coincidence time-bin resolution is set to 8 ps and coincidences are summed within a 10 ns window. Fourth-order interferograms were measured for different bandwidths of entangled photon pairs. For the first experiment, bandpass filters centered at 810 nm with a 10 nm FWHM are mounted to the front of each of the fiber coupling units. Note that this filter is not at the 812nm degenerate wavelength and reduces the degree of entanglement. For the second experiment, the 810 nm bandpass filters are removed to couple the broadband, collinear SPDC into the SPADs. Finally, the oven is allowed to cool to the non-collinear but degenerate temperature of 150°C , and broadband two-photon interference was measured again. Note that due to the large bandwidth of the SPDC, the fiber coupling efficiency of the non-degenerate photons is also poor at less than 10% of total power. Thus, 42% of the overall SPDC flux was lost before reaching the fibers connecting to the SPADs. Over 20% of the loss was due to the high angular dispersion of the beam, while the other $\sim 20\%$ of the loss was due to the reflective optics such as the aluminum OAP and silver mirrors. As discussed at the end of this section, optics development is still needed similar to using classical broadband ultrafast lasers.

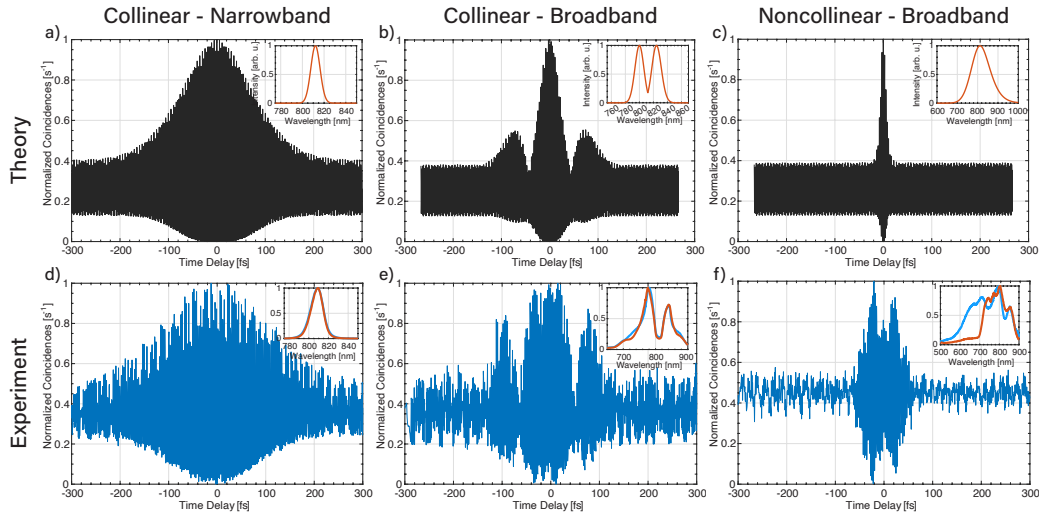


Figure 3.9: Simulated (top row) and measured (bottom row) fourth-order interference for narrowband collinear (a,d), broadband collinear (b,e), and broadband non-collinear (c,f) entangled photons. Coincidence counts are measured with 15 s integration time. The insets in each figure depict the SPDC spectra used to simulate or measure the corresponding interference in each detector arm. For simulations, Gaussian functions are used to approximate SPDC spectral envelopes. As shown in Table 3.2, the theoretical and measured coherence times are 200 fs and 245 fs for collinear narrowband, 45 fs and 57.4 fs for collinear broadband, 18 fs and 62 fs for non-collinear broadband. The growing difference between expected time resolution from the SPDC bandwidth and the measured interference is due to the difficulty with fiber coupling the full cone emission profile.

Fig. 3.9 shows the simulated fourth-order interferences using the produced bandwidth of the SPDC source and then the measured fourth-order interferences for two collinear bandwidths and a third non-collinear, full spectrum measurement. When the quarter-wave plate is set to 0° , the photons arriving at BS1 have the same polarization, and interfere coherently as correlated pairs. The interference pattern is robust against pump power fluctuations. When the quarter-wave plate is rotated to 45° , the reflected arm becomes perpendicularly polarized to the transmitted arm, the interference pattern disappears, and the coincidence counts follow the average pump power reading collected before and after the coincidence detection (Figs. A.8,A.9). The resulting coherence length of the total flux can be determined from the width of the interference peak. Table 3.2 summarizes the theoretical and measured coherence lengths.

For the measurement with 810-(10) nm bandpass filters mounted to the front of the fiber coupling units, shown in Fig. 3.9(d), the coherence length is approximately

	Collinear narrowband	Collinear broadband	Non-collinear broadband
Theoretical coherence time [fs]	200	45	18
Measured coherence time [fs]	245	57.4	62

Table 3.2: Coherence times of different configurations and bandwidths of SPDC

$73\mu\text{m}$ (or 245 fs). The simulated interference pattern as well as the coherence length of $60\mu\text{m}$ (200 fs), shown in Fig. 3.9(a), agree fairly with the measurement given that the 10nm bandpass filter is offset from the degenerate wavelength of 812 nm. Note that the measured bandwidth after the fiber is roughly double what it actually is because the spectrometer slit had to be run wide to get sufficient flux for spectral analysis after the fiber coupling. The theoretical plot uses the correct bandwidth. Fig. 3.9(e) shows the interference from collinear broadband SPDC flux without bandpass filters. The bandwidth is reduced and the SPDC spectrum is split (nondegenerate) because the phase matching temperature is maintained at the elevated collinear emission (Fig. 3.2). From the width of the center peak, the coherence length is approximately $17.2\mu\text{m}$ (or 57.4 fs). For reference, the simulated coherence length is approximately $13\mu\text{m}$ (45 fs). Similarly, Fig. 3.9(f) shows the lower temperature non-collinear broadband interference. Here, the full 200 nm bandwidth of the SPDC source is attempted to be used (expected temporal width 8 fs). However the spectrum reaching the detector is limited to 125 nm because of collimation issues, upstream optics, and fiber coupling. The coherence length calculated from the measured width of the peak is $18.9\mu\text{m}$ (or 62 fs). This indicates that the degree of entanglement has degraded due to poor fiber coupling at non-collinear temperatures and other upstream optics. For example, the spectrum after the multiple beamsplitters is not balanced (Fig. 3.9(f), inset) as compared to the other cases. The increased temporal width is also indicative of the need for dispersion management upstream, just as is similar to a broadband ultrafast laser pulse of an expected 20 fs pulse. The same would be true for the chirped (> 200 nm) SPDC source so an interferogram is not shown here. Note that the measured broadband spectra in the insets do not well match the theoretical spectra. This is because 1) fiber coupling of the broad bandwidth was not optimal and 2) the free

space spectrometer slit was opened wide to increase the measurement fluxes which leads to a spectral broadening by a factor of 2.

The lack of fiber coupling efficiency in the broadband, non-collinear case is not simply one of input optics. Immediately following the chip, the spatial profile of the entangled photons is cone-like with a wavelength-dependent distribution (Fig. 3.10 left). The measured angular deviation with wavelength matches the simulated entangled photon emission. Within a non-degenerate pair, the idler photon has a larger emission angle than the signal photon. The wavelength-dependent angular emission cone presents a challenge in the implementation of free-space broadband entangled photon setups because the emission does not act like a single point source. We attempted to collimate the emission cone using a variety of free-space optical configurations and found that a telephoto lens or an off-axis parabolic mirror (sometimes with an additional cylindrical lens for beam shaping) provides the best long range spatial profiles. After a propagation length of 45 cm into the far field, the entangled photon cone collapses (Fig. 3.10 middle). This spatial profile collapse is most likely due to the interference of photon pairs created along the length of the crystal and scattering effects near the domain boundaries of the grating. The end result shows characteristics of somewhere between a Laguerre and a Hermite mode which would match the circular emission in a square profile created by the source. The beam profile will likely be improved by using adaptive optics. The far field effects could also be reduced by using a waveguide instead of a grating; however, nanophotonic implementations cannot handle the high input powers used in this paper and fiber coupling of the broadband emission spectrum from waveguides is not yet well developed. Another obvious option is, instead of using fiber coupled SPADs for the detection, is to move to emICCD photon counting techniques that would not require focusing of the collapsed beam profile. However, this approach still needs exploration and requires an emICCD even more costly than SPADs. A necessary future development for the broadband entangled photon source is the clean-up of the SPDC spatial mode. Following the output of the bulk crystal, several possible improvements can be implemented including a spatial light modulator (SLM) to imprint phase and intensity shifts on the SPDC cone [56]. Alternatively, a combination of diffraction gratings and lenses could be used to correct the angular dispersion of the broadband wavelengths. The SPDC output could also be coupled into a broad bandwidth photonic crystal fiber such that the photons are propagating in a single spatial mode. Further, the spatial mode of the input pump beam could be modulated with an SLM or combinations of lenses/axicons to achieve the desired

output SPDC spatial mode. Further investigation into the creation and collimation of broadband entangled photons is critical for the implementation of short temporal length, high flux entangled photon spectroscopy.

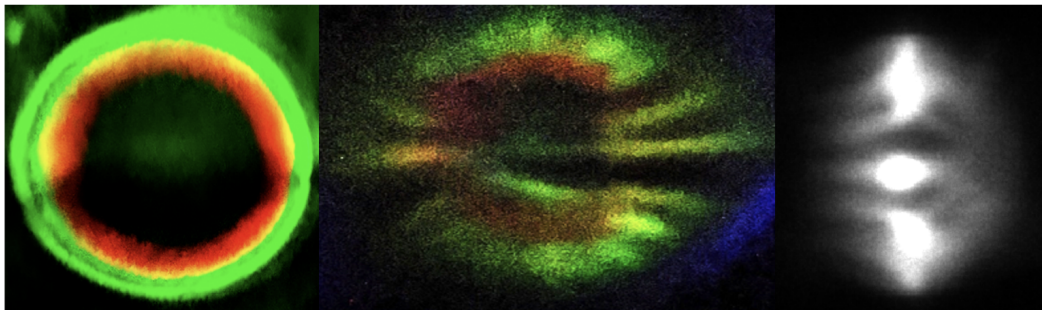


Figure 3.10: Images of collimated SPDC emission cone at 145°C in the near field (left), far field (middle) after collimation with an off axis parabolic mirror, and far field after collimation and focusing by a 15.45 cm focal length lens (right). The left and middle images are collected with a standard cell-phone camera, the right image is collected with an emICCD.

3.4 Conclusion

Quasi-phase-matching in periodically poled crystals offers significant benefits in the experimental implementation of broadband entangled photon sources for use in spectroscopy. Simulated parameters for unchirped, periodically poled lithium tantalate gratings were utilized to design and construct a broadband entangled photon source spanning nearly an octave in frequency. This broadband source was characterized by measuring the output spectra of the grating and the fourth order interference by a two-photon Michelson interferometer. The two-photon Michelson interferometer was used to emphasize where further optics and detector development is still need to utilize the broadband and short temporal width sources. As in, the SPDC spectrum can be reliably created from the designed chip, however, the downstream optics and detectors still need development to fully utilize this source. Given the theoretical and experimentally demonstrated advantages of entangled photons in studies of chemical, biological, and material systems, we anticipate the widespread applicability of this particular energy-time entangled photon source.

References

1. Burnham, D. C. & Weinberg, D. L. Observation of Simultaneity in Parametric Production of Optical Photon Pairs. *Physical Review Letters* **25**, 84–87. [http](#)

- [ps://link.aps.org/doi/10.1103/PhysRevLett.25.84](https://link.aps.org/doi/10.1103/PhysRevLett.25.84) (2020) (July 1970).
2. Szoke, S., Liu, H., Hickam, B. P., He, M. & Cushing, S. K. Entangled light–matter interactions and spectroscopy. *Journal of Materials Chemistry C* **8**, 10732–10741. <http://pubs.rsc.org/en/content/articlelanding/2020/tc/d0tc02300k> (2020) (Aug. 2020).
 3. Hong, C. K., Ou, Z. Y. & Mandel, L. Measurement of subpicosecond time intervals between two photons by interference. *Physical Review Letters* **59**, 2044–2046. <https://link.aps.org/doi/10.1103/PhysRevLett.59.2044> (2018) (Nov. 1987).
 4. Mitev, V., Balet, L., Torcheboeuf, N., Renevey, P. & Boiko, D. L. Discrimination of entangled photon pair from classical photons by de Broglie wavelength. *Scientific Reports* **10**, 7087. <https://www.nature.com/articles/s41598-020-63833-8> (2023) (Apr. 2020).
 5. Shimizu, R., Edamatsu, K. & Itoh, T. Quantum diffraction and interference of spatially correlated photon pairs generated by spontaneous parametric down-conversion. *Physical Review A* **67**, 041805. <https://link.aps.org/doi/10.1103/PhysRevA.67.041805> (2019) (Apr. 2003).
 6. Abouraddy, A. F., Saleh, B. E. A., Sergienko, A. V. & Teich, M. C. Double-slit interference of biphotons generated in spontaneous parametric downconversion from a thick crystal. *Journal of Optics B: Quantum and Semiclassical Optics* **3**, S50. <https://dx.doi.org/10.1088/1464-4266/3/1/359> (2023) (Feb. 2001).
 7. Javanainen, J. & Gould, P. L. Linear intensity dependence of a two-photon transition rate. *Physical Review A* **41**, 5088–5091. <https://link.aps.org/doi/10.1103/PhysRevA.41.5088> (2019) (May 1990).
 8. Dayan, B., Pe'er, A., Friesem, A. A. & Silberberg, Y. Nonlinear Interactions with an Ultrahigh Flux of Broadband Entangled Photons. *Physical Review Letters* **94**, 043602. <https://link.aps.org/doi/10.1103/PhysRevLett.94.043602> (2020) (Feb. 2005).
 9. Villabona-Monsalve, J. P., Burdick, R. K. & Goodson, T. Measurements of Entangled Two-Photon Absorption in Organic Molecules with CW-Pumped Type-I Spontaneous Parametric Down-Conversion. *The Journal of Physical Chemistry C*, [acs.jpcc.0c08678](https://pubs.acs.org/doi/10.1021/acs.jpcc.0c08678). <https://pubs.acs.org/doi/10.1021/acs.jpcc.0c08678> (2020) (Oct. 2020).
 10. Raymer, M. G., Marcus, A. H., Widom, J. R. & Vitullo, D. L. P. Entangled Photon-Pair Two-Dimensional Fluorescence Spectroscopy (EPP-2DFS). *The Journal of Physical Chemistry B* **117**, 15559–15575. <https://doi.org/10.1021/jp405829n> (2018) (Dec. 2013).

11. Tabakaev, D. *et al.* Energy-time-entangled two-photon molecular absorption. *Physical Review A* **103**, 033701. <https://link.aps.org/doi/10.1103/PhysRevA.103.033701> (2021) (Mar. 2021).
12. Li, T., Li, F., Altuzarra, C., Classen, A. & Agarwal, G. S. Squeezed light induced two-photon absorption fluorescence of fluorescein biomarkers. *Applied Physics Letters* **116**, 254001. <https://aip.scitation.org/doi/10.1063/5.0010909> (2020) (June 2020).
13. Kang, G. *et al.* Efficient Modeling of Organic Chromophores for Entangled Two-Photon Absorption. *Journal of the American Chemical Society* **142**, 10446–10458. <https://doi.org/10.1021/jacs.0c02808> (2020) (June 2020).
14. Boto, A. N. *et al.* Quantum Interferometric Optical Lithography: Exploiting Entanglement to Beat the Diffraction Limit. *Physical Review Letters* **85**, 2733–2736. <https://link.aps.org/doi/10.1103/PhysRevLett.85.2733> (2022) (Sept. 2000).
15. Steuernagel, O. On the concentration behaviour of entangled photons. *Journal of Optics B: Quantum and Semiclassical Optics* **6**, S606–S609. <https://iopscience.iop.org/article/10.1088/1464-4266/6/6/021> (2023) (June 2004).
16. Oka, H. Selective two-photon excitation of a vibronic state by correlated photons. *The Journal of Chemical Physics* **134**, 124313. <https://aip.scitation.org/doi/10.1063/1.3573565> (2019) (Mar. 2011).
17. Oka, H. Enhanced vibrational-mode-selective two-step excitation using ultrabroadband frequency-entangled photons. *Physical Review A* **97**, 063859. <https://link.aps.org/doi/10.1103/PhysRevA.97.063859> (2019) (June 2018).
18. Schlawin, F., Dorfman, K. E. & Mukamel, S. Entangled Two-Photon Absorption Spectroscopy. *Accounts of Chemical Research* **51**, 2207–2214. <https://doi.org/10.1021/acs.accounts.8b00173> (2018) (Sept. 2018).
19. Dorfman, K. E., Schlawin, F. & Mukamel, S. Nonlinear optical signals and spectroscopy with quantum light. *Reviews of Modern Physics* **88**, 045008. <https://link.aps.org/doi/10.1103/RevModPhys.88.045008> (2018) (Dec. 2016).
20. MacLean, J.-P. W., Schwarz, S. & Resch, K. J. Reconstructing ultrafast energy-time-entangled two-photon pulses. *Physical Review A* **100**, 033834. <https://link.aps.org/doi/10.1103/PhysRevA.100.033834> (2023) (Sept. 2019).
21. Nasr, M. B., Giuseppe, G. D., Saleh, B. E. A., Sergienko, A. V. & Teich, M. C. Generation of high-flux ultra-broadband light by bandwidth amplification in spontaneous parametric down conversion. *Optics Communications* **246**,

- 521–528. <https://www.sciencedirect.com/science/article/pii/S0030401804011162> (2023) (Feb. 2005).
22. Kwiat, P. G. *et al.* New High-Intensity Source of Polarization-Entangled Photon Pairs. *Physical Review Letters* **75**, 4337–4341. <https://link.aps.org/doi/10.1103/PhysRevLett.75.4337> (2020) (Dec. 1995).
 23. Friberg, S., Hong, C. K. & Mandel, L. Measurement of Time Delays in the Parametric Production of Photon Pairs. *Physical Review Letters* **54**, 2011–2013. <https://link.aps.org/doi/10.1103/PhysRevLett.54.2011> (2020) (May 1985).
 24. Kwiat, P. G., Waks, E., White, A. G., Appelbaum, I. & Eberhard, P. H. Ultrabright source of polarization-entangled photons. *Physical Review A* **60**, R773–R776. <https://link.aps.org/doi/10.1103/PhysRevA.60.R773> (2019) (Aug. 1999).
 25. Karan, S. *et al.* Phase matching in β -barium borate crystals for spontaneous parametric down-conversion. *Journal of Optics* **22**, 083501. <https://dx.doi.org/10.1088/2040-8986/ab89e4> (2023) (June 2020).
 26. Nikogosyan, D. N. Beta barium borate (BBO). *Applied Physics A* **52**, 359–368. <https://doi.org/10.1007/BF00323647> (2023) (June 1991).
 27. Midwinter, J. E. & Warner, J. The effects of phase matching method and of crystal symmetry on the polar dependence of third-order non-linear optical polarization. *British Journal of Applied Physics* **16**, 1667. <https://dx.doi.org/10.1088/0508-3443/16/11/307> (2023) (Nov. 1965).
 28. Roslyak, O. & Mukamel, S. Multidimensional pump-probe spectroscopy with entangled twin-photon states. *Physical Review A* **79**, 063409. <https://link.aps.org/doi/10.1103/PhysRevA.79.063409> (2018) (June 2009).
 29. Lerch, S. & Stefanov, A. Experimental requirements for entangled two-photon spectroscopy. *The Journal of Chemical Physics* **155**, 064201. <https://aip.scitation.org/doi/10.1063/5.0050657> (2022) (Aug. 2021).
 30. Wang, S., Pasiskevicius, V., Hellström, J., Laurell, F. & Karlsson, H. First-order type II quasi-phase-matched UV generation in periodically poled KTP. *Optics Letters* **24**, 978–980. <https://www.osapublishing.org/ol/abstract.cfm?uri=ol-24-14-978> (2020) (July 1999).
 31. Yu, N. E., Ro, J. H., Cha, M., Kurimura, S. & Taira, T. Broadband quasi-phase-matched second-harmonic generation in MgO-doped periodically poled LiNbO₃ at the communications band. *Optics Letters* **27**, 1046–1048. <https://opg.optica.org/ol/abstract.cfm?uri=ol-27-12-1046> (2023) (June 2002).

32. Lin, J. *et al.* Broadband Quasi-Phase-Matched Harmonic Generation in an On-Chip Monocrystalline Lithium Niobate Microdisk Resonator. *Physical Review Letters* **122**, 173903. <https://link.aps.org/doi/10.1103/PhysRevLett.122.173903> (2020) (May 2019).
33. Chen, J., Pearlman, A. J., Ling, A., Fan, J. & Migdall, A. L. A versatile waveguide source of photon pairs for chip-scale quantum information processing. *Optics Express* **17**, 6727. <https://www.osapublishing.org/oe/abstract.cfm?uri=oe-17-8-6727> (2020) (Apr. 2009).
34. Bock, M., Lenhard, A., Chunnillal, C. & Becher, C. Highly efficient heralded single-photon source for telecom wavelengths based on a PPLN waveguide. *Optics Express* **24**, 23992–24001. <https://www.osapublishing.org/oe/abstract.cfm?uri=oe-24-21-23992> (2018) (Oct. 2016).
35. Shi, B.-S. & Tomita, A. Highly efficient generation of pulsed photon pairs with bulk periodically poled potassium titanyl phosphate. *Journal of the Optical Society of America B* **21**, 2081–2084. <https://opg.optica.org/josab/abstract.cfm?uri=josab-21-12-2081> (2023) (Dec. 2004).
36. Armstrong, J. A., Bloembergen, N., Ducuing, J. & Pershan, P. S. Interactions between Light Waves in a Nonlinear Dielectric. *Physical Review* **127**, 1918–1939. <https://link.aps.org/doi/10.1103/PhysRev.127.1918> (2019) (Sept. 1962).
37. Tanzilli, S. *et al.* Highly efficient photon-pair source using periodically poled lithium niobate waveguide. *Electronics Letters* **37**, 26–28 (Jan. 2001).
38. Nasr, M. B. *et al.* Ultrabroadband Biphotons Generated via Chirped Quasi-Phase-Matched Optical Parametric Down-Conversion. *Physical Review Letters* **100**, 183601. <https://link.aps.org/doi/10.1103/PhysRevLett.100.183601> (2019) (May 2008).
39. Pe'er, A., Dayan, B., Friesem, A. A. & Silberberg, Y. Temporal Shaping of Entangled Photons. *Physical Review Letters* **94**, 073601. <https://link.aps.org/doi/10.1103/PhysRevLett.94.073601> (2020) (Feb. 2005).
40. Ou, Z. Y. & Lu, Y. J. Cavity Enhanced Spontaneous Parametric Down-Conversion for the Prolongation of Correlation Time between Conjugate Photons. *Physical Review Letters* **83**, 2556–2559. <https://link.aps.org/doi/10.1103/PhysRevLett.83.2556> (2023) (Sept. 1999).
41. Hadfield, R. H. Single-photon detectors for optical quantum information applications. *Nature Photonics* **3**, 696–705. <https://www.nature.com/articles/nphoton.2009.230> (2022) (Dec. 2009).
42. Lerch, S. & Stefanov, A. Observing the transition from quantum to classical energy correlations with photon pairs. *Communications Physics* **1**, 1–6. <https://www.nature.com/articles/s42005-018-0027-2> (2023) (June 2018).

43. Zverev, G. M., Levchuk, E. A., Pashkov, V. A. & Poryadin, Y. D. Laser-Radiation-Induced Damage to the Surface of Lithium Niobate and Tantalate Single Crystals. *Soviet Journal of Quantum Electronics* **2**, 167. <https://iopscience.iop.org/article/10.1070/QE1972v002n02ABEH004409/meta> (2023) (Feb. 1972).
44. Antonov, V. A., Arsenev, P. A., Linda, I. G. & Farstendiker, V. L. Colour centres in single crystals of lithium tantalate. *physica status solidi (a)* **28**, 673–676. <https://onlinelibrary.wiley.com/doi/abs/10.1002/pssa.2210280234> (2023) (1975).
45. Meyn, J.-P. & Fejer, M. M. Tunable ultraviolet radiation by second-harmonic generation in periodically poled lithium tantalate. *Optics Letters* **22**, 1214–1216. <https://opg.optica.org/ol/abstract.cfm?uri=ol-22-16-1214> (2023) (Aug. 1997).
46. Lopez-Mago, D. & Novotny, L. Coherence measurements with the two-photon Michelson interferometer. *Physical Review A* **86**, 023820. <https://link.aps.org/doi/10.1103/PhysRevA.86.023820> (2020) (Aug. 2012).
47. Klyshko, D. N., Penin, A. N. & Polkovnikov, B. F. Parametric Luminescence and Light Scattering by Polaritons. *Journal of Experimental and Theoretical Physics Letters* **11**, 11–14 (1970).
48. Boyd, R. W. *Nonlinear Optics* ISBN: 978-0-08-048596-6 (Elsevier, May 2008).
49. Fejer, M. M., Magel, G. A., Jundt, D. H. & Byer, R. L. Quasi-phase-matched second harmonic generation: tuning and tolerances. *IEEE Journal of Quantum Electronics* **28**, 2631–2654 (Nov. 1992).
50. Moutzouris, K., Hloupis, G., Stavrakas, I., Triantis, D. & Chou, M.-H. Temperature-dependent visible to near-infrared optical properties of 8 mol% Mg-doped lithium tantalate. *Optical Materials Express* **1**, 458–465. <https://www.osapublishing.org/ome/abstract.cfm?uri=ome-1-3-458> (2020) (July 2011).
51. Di Giuseppe, G. *et al.* Entangled-photon generation from parametric down-conversion in media with inhomogeneous nonlinearity. *Physical Review A* **66**, 013801. <https://link.aps.org/doi/10.1103/PhysRevA.66.013801> (2023) (July 2002).
52. Burlakov, A. V. *et al.* Interference effects in spontaneous two-photon parametric scattering from two macroscopic regions. *Physical Review A* **56**, 3214–3225. <https://link.aps.org/doi/10.1103/PhysRevA.56.3214> (2023) (Oct. 1997).
53. Brańczyk, A. M., Fedrizzi, A., Stace, T. M., Ralph, T. C. & White, A. G. Engineered optical nonlinearity for quantum light sources. *Optics Express* **19**, 55–65 (Jan. 2011).

54. Reichert, M., Defienne, H. & Fleischer, J. W. Massively Parallel Coincidence Counting of High-Dimensional Entangled States. *Scientific Reports* **8**, 1–7. <https://www.nature.com/articles/s41598-018-26144-7> (2019) (May 2018).
55. Zhang, Y. *et al.* Multidimensional quantum-enhanced target detection via spectrotemporal-correlation measurements. *Physical Review A* **101**, 053808. <https://link.aps.org/doi/10.1103/PhysRevA.101.053808> (2020) (May 2020).
56. Bessire, B., Bernhard, C., Feurer, T. & Stefanov, A. Versatile shaper-assisted discretization of energy–time entangled photons. *New Journal of Physics* **16**, 033017. <https://dx.doi.org/10.1088/1367-2630/16/3/033017> (2023) (Mar. 2014).

Chapter 4

SINGLE PHOTON SCATTERING CAN ACCOUNT FOR THE
DISCREPANCIES BETWEEN ENTANGLED TWO-PHOTON
MEASUREMENT TECHNIQUES

ABSTRACT

Entangled photon pairs are predicted to linearize and increase the efficiency of two-photon absorption, allowing continuous wave laser diodes to drive ultrafast time-resolved spectroscopy and nonlinear processes. Despite a range of theoretical studies and experimental measurements, inconsistencies persist about the value of the entanglement enhanced interaction cross section. A spectrometer is constructed that can temporally and spectrally characterize the entangled photon state before, during, and after any potential two-photon excitation event. Specifically, this instrument is based upon an interferometric design that probabilistically separates the entangled photon pairs and monitors the resulting transmitted signal, as well as the spectrally-resolved 90-degree signal from the sample. For the molecule Rhodamine 6G, which has a virtual state pathway, any entangled two-photon interaction is found to be equal to or lower than classical, single photon scattering events. This result can account for the discrepancies between the wide variety of entangled two-photon absorption cross sections reported from different measurement techniques. The reported instrumentation represents a major development in the field due to its ability to unambiguously separate classical and entangled effects and therefore is of importance for the growing field of nonlinear and multiphoton entangled spectroscopy.

Most of this chapter has been adapted with permission from:

Hickam, B. P. *et al.* Single-Photon Scattering Can Account for the Discrepancies among Entangled Two-Photon Measurement Techniques. *The Journal of Physical Chemistry Letters*, 4934–4940. ISSN: 1948-7185, 1948-7185. <https://pubs.acs.org/doi/10.1021/acs.jpcllett.2c00865> (2022) (May 2022).

4.1 Introduction

It is well known that the inherent correlations between entangled photons lead to spectroscopic enhancements in signal-to-noise [1–4], and diffraction limits [5] as well as measurement techniques such as ghost imaging [6–12]. A new and quickly growing field of entangled two-photon spectroscopy exploits these correlations in a different manner: enhancing excited state and multiphoton interactions [13–16]. For example, early experiments purported that entangled photons can linearize two-photon processes to achieve near one-photon absorption cross sections [17]. This finding would have far-reaching implications in optics and photonics as low power, continuous wave (CW) laser systems could replace pulsed lasers in spectroscopic techniques such as nonlinear bioimaging and ultrafast spectroscopy [18–20]. Combined with nanophotonic platforms that are capable of generating and manipulating entangled photon pairs [21, 22], ultrafast measurements could achieve unprecedented accessibility and availability.

While the entangled photons' linearization of two-photon processes can be derived theoretically [23–25], intense debate exists over the enhancement factor compared to classical two-photon absorption. Naively, one would expect the entangled two-photon absorption (ETPA) cross section to be close to that of a single photon process, given the linearization of the absorption. However, as shown in Fig. 4.1, the reported range of ETPA cross sections varies from near single photon levels to non-existent or barely higher than classical two-photon absorption at the same photon flux [17, 19, 26–38]. Complicating this debate is the disparate measurement techniques based on transmission, coincidence counting, and fluorescence that have been used. An agreed upon measurement process does not exist, and even those that are proposed rely on intensity counting methods instead of temporally and spectrally characterizing the entangled photon state during a proposed interaction event.

In this paper, we construct a spectrometer that temporally and spectrally measures the entangled photon state before, during, and after a proposed entangled two-photon event. The spectrometer is used to measure the proposed ETPA of a prototypical molecular dye, Rhodamine 6G (R6G), which has a well characterized, virtual state-mediated classical two-photon absorption pathway [40, 41]. To enhance the chances of measuring a two-photon fluorescence signal, the spectrometer uses a custom, high-flux (20 nW) entangled photon source with a tunable bandwidth and correlation time down to 20 fs [42]. By measuring the temporal and spectral characteristics of the entangled state in transmission, and the 90-degree signal relative to the cuvette,

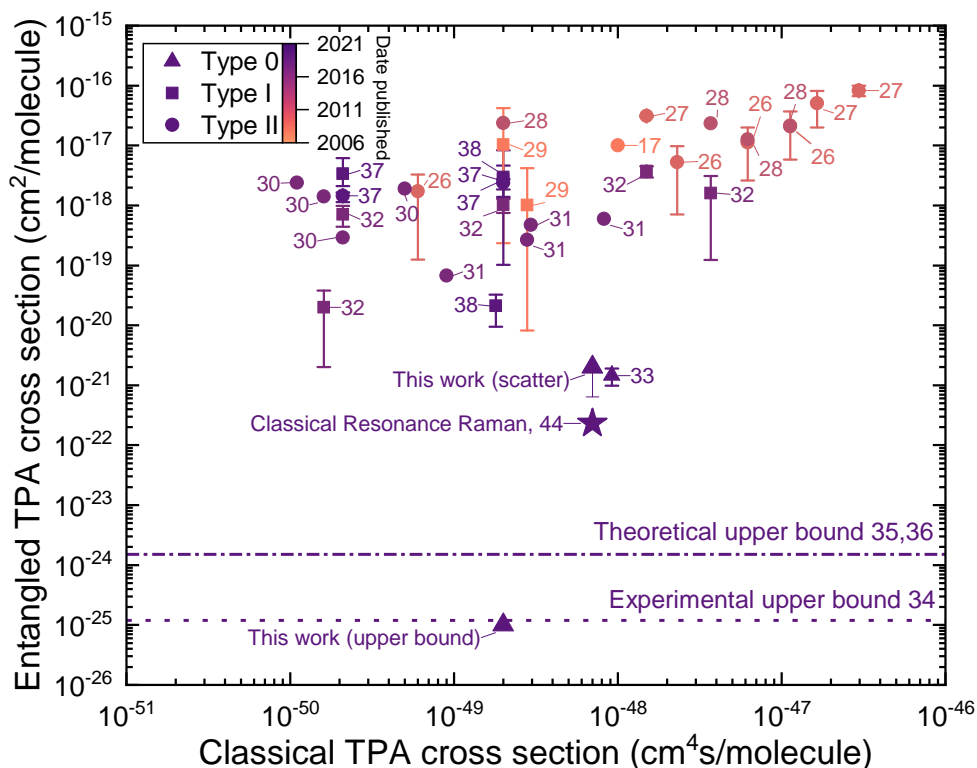


Figure 4.1: Reported experimental ETPA cross sections vs. classical TPA cross sections compiled from all ETPA studies conducted prior to January 2022 [17, 19, 26–38]. The shape of the data point reflects the polarization type of the entangled photons. Reported ETPA cross sections for the same compound at varying concentrations are represented as an average with vertical error bars indicating the highest and lowest reported bounds. The dashed lines represent ETPA upper bounds that were previously reported [27–29]. The shading of the points indicates the year in which the results were published, with darker colors representing more recent data. Classical resonance Raman cross section is also included [39].

we determine that if any entangled enhancement to the virtual-state mediated two-photon absorption is present, it has a cross section smaller than that of single photon (resonant) scattering ($\sim 10^{-21}$ cm²/molecule).

The conclusion is based on the facts that: 1) the entangled state is nearly identical before and after transmission, with only a slight amplitude loss, and 2) the scattered signal temporally follows the pattern of one-photon interference instead of entangled two-photon interference, with spectral components far from the fluorescence spectrum of the dye. The single photon scattering explains the past discrepancies in

measured cross sections between different techniques. Moreover, the paper presents a blueprint for a spectrometer that can unambiguously determine entangled photon excited state effects in the rapidly growing field of entangled nonlinear and multiphoton spectroscopy. The scattering limited cross section for R6G also bolsters current theories that suggest virtual state pathways have cross sections that are beyond noise limits of single photon detectors and that real intermediate states may be necessary for entangled two-photon excitation events with high cross sections [43, 44].

4.2 Experimental overview

Entangled photons are generated from a periodically poled 8% MgO doped congruent lithium tantalate (CLT) bulk crystal. The design and spectral characterization of the entangled photon source have previously been reported [42]. The crystal is optimized for type-0 energy-time entanglement by spontaneous parametric down-conversion (SPDC). A bandwidth of ~ 200 nm is produced by down-conversion of a 406 nm CW diode laser with a 1.5 nm linewidth. The large bandwidth and 10^{-8} conversion efficiency allow for a flux in the sub- μ W range without exceeding the single-pair-per-mode quantum limit, as calculated by total photon pairs per second divided by the frequency bandwidth in Hz. The available photon flux is a significant improvement compared with the pW powers in most previous reports that use traditional bulk crystals such as beta barium borate (β -BBO) [17, 32, 37]. The broad bandwidth also results in a ~ 20 fs correlation time (entanglement time) as measured after the sample. The entanglement time is not transform limited due to the group delay dispersion in the periodically poled chip and further optics. The high flux and tunable correlation times, from tens of femtoseconds to picoseconds, maximize the likelihood of measuring any entangled event [28, 29]. The entangled photon bandwidth can be varied by tuning the temperature of the bulk crystal. For experiments in this paper, two distinct entangled photon bandwidths centered at 812 nm were utilized: a non-degenerate “split” SPDC spectrum spanning ~ 200 nm in wavelength and a degenerate “unsplit” SPDC spectrum (more details in B). The two SPDC spectra are used to emphasize the scattering that can happen both close to and far from resonance of a molecule’s absorption.

Rhodamine 6G was selected for this study because of its absorption near the SPDC pump laser wavelength [40], its purely virtual two-photon classical absorption, as well as its high fluorescence quantum yield [45]. There are also several references of the proposed R6G ETPA from different measurement techniques [26, 27]. A concentration of 5 mM R6G in ethanol is used for experiments; the classical single-

photon fluorescence spectrum for this concentration is depicted in Fig. 4.4. Solvent effects and molecular dimerization at high sample concentration accounts for the redshifted spectrum [46]. Previously reported one-photon absorption cross sections for R6G in ethanol are on the order of $10^{-16} - 10^{-17} \text{ cm}^2/\text{molecule}$ and the two-photon absorption cross section is $70(\pm 10.5) * 10^{-50} \text{ cm}^4\text{s}/\text{molecule}$ [40]. A higher 110 mM sample was also tested with the same conclusions. The 110 mM sample would have a 10-times higher fluorescence after the drop in quantum yield and self-absorption effects are taken into account, but the results of the paper were unchanged.

A custom two-photon Michelson-type interferometer, shown in Fig. 4.2, is used to characterize the entangled photon state. Specifically, the fourth-order interference, spectral characteristics, and entanglement (coherence) time of the broadband entangled photons are determined [47, 48]. Type-0 SPDC was chosen because it utilizes the highest second-order nonlinear coefficient of LiTaO_3 [49]. The two-photon Michelson-type interferometer allows the broad, collinear SPDC bandwidth to be more easily directed onto the sample. More specifically, the photon pairs are focused (beam waist $500 \mu\text{m}$) onto the center of the cuvette. The measurement protocol is as follows: first, a cuvette containing pure ethanol is placed at the output of the Michelson interferometer. Second, the fourth-order interference is measured by collecting coincidences as a function of an optical time delay. The coincidence counting detection setup consists of a broadband 50:50 beamsplitter and two single photon avalanche photodiodes (SPADs, Laser Components). The fourth-order interference measurements are then repeated with the cuvette filled with R6G solution. Simultaneous to the coincidence counting measurement, a single photon counting EMICCD spectrometer (Princeton Instruments) is placed at 90 degrees relative to the excitation beam to measure any scatter or fluorescence. The collection efficiency including the spectrometer is $\sim 10^{-4}$, calculated from the measured classical single photon fluorescence and quantum yield of R6G. By monitoring the timescale and spectral features of the 90-degree signal, one can differentiate one-photon events, such as scattering, from an entangled two-photon absorption or fluorescence event [26, 27, 50]. A complete mathematical description of the interferometer output can be found in the supplementary information.

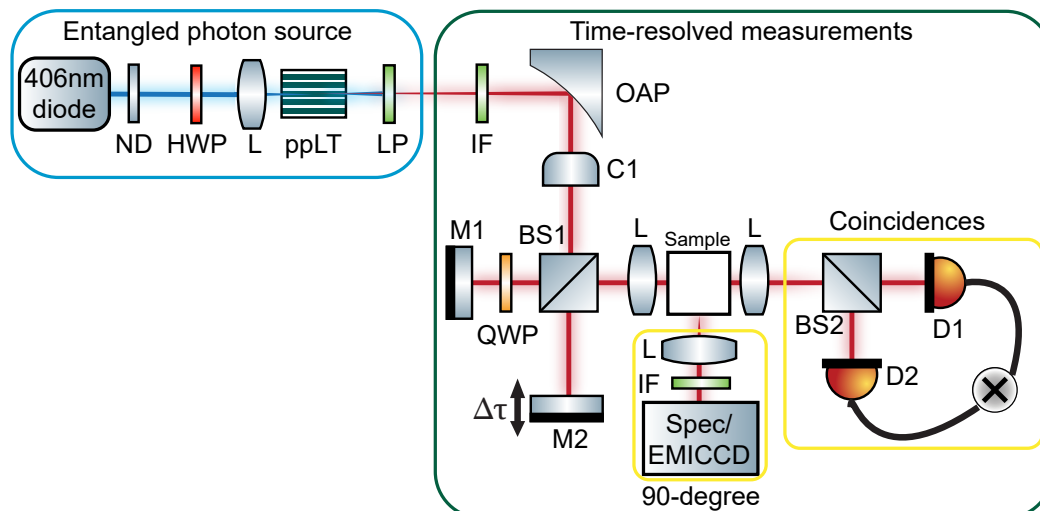


Figure 4.2: Experimental setup used to measure the proposed entangled two-photon absorption and 90-degree signal. The entangled photon source consists of a continuous wave diode laser pumping a periodically poled lithium tantalate crystal. The resultant entangled photon cone is collimated before the two-photon Michelson interferometer. The fourth-order interference of the entangled photon pairs is measured with a coincidence counting configuration and the time-resolved 90-degree signal was imaged onto a spectrometer/EMICCD. ND: continuous neutral density filter wheel, HWP: half-wave plate, L: lens, ppLT: periodically poled lithium tantalate chip, LP: 500 nm longpass filter, IF: interference filter, OAP: off-axis parabolic mirror, C1: cylindrical lens, QWP: quarter-wave plate, BS1 and BS2: 50:50 plate beamsplitters, M1 and M2: mirrors, D1 and D2: multimode fiber coupled single photon avalanche diodes connected to a coincidence circuit, Spec/EMICCD: Spectrometer and electron multiplying intensified charge coupled device.

4.3 Results: Fourth-order interference measurements

Figure 4.3 shows the fourth-order interference of the entangled photon state before and after interacting with 5 mM R6G/ethanol as well as the signal collected at 90-degrees to the excitation pathway during the interaction. Corresponding theoretical fitting is included in the supplementary information. The top trace is the measured coincidences through a cuvette filled with pure ethanol. In a two-photon Michelson interferogram, the degree of entanglement can be qualitatively inferred by examining the amplitude ratio above and below the oscillation baseline. A “top-heavy” feature, for example shown in Fig. 4.3 top trace, indicates photon bunching. Given the $> 95\%$ visibility measured here and the fact that SPDC with a CW laser inherently creates an entangled state, we can reasonably confirm that our input source is entangled. For this experiment, the coherence/entanglement time is < 20 fs and the

interference visibility is 0.94. When the cuvette is filled with R6G (middle trace in Fig. 4.3), the visibility of the interference slightly decreases to 0.86, but the interferogram retains the spectral and temporal features shown with ethanol (with a slight shift in temporal patterns due to the change in refractive index. If ETPA does occur, then the photon bunching feature will diminish and the classical component will change spectrally due to the added fluorescence signal (or a nonuniform single photon absorption process).

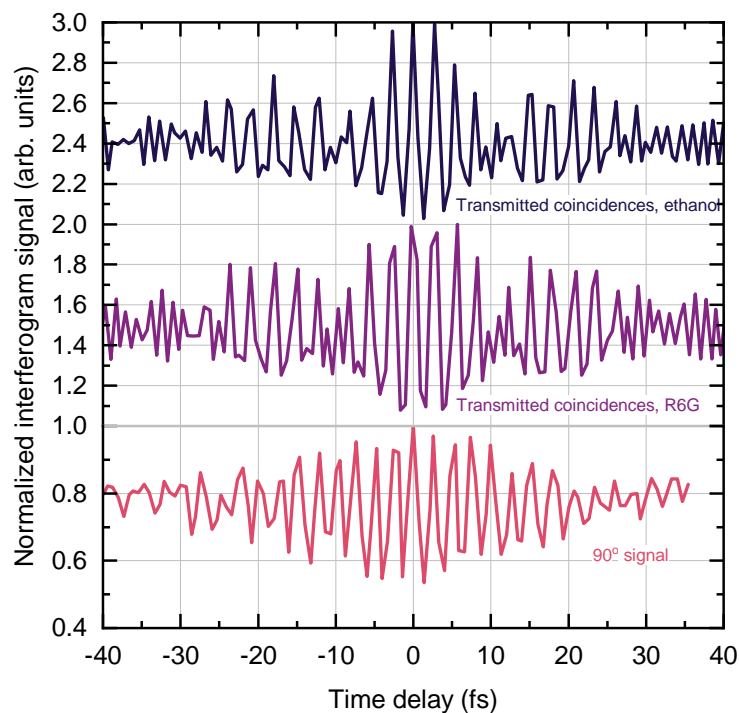


Figure 4.3: Photon counts versus time delay for broadband entangled photons traveling through a two-photon Michelson interferometer. The top trace is transmitted coincidence counts through ethanol, the middle trace is transmitted coincidence counts through R6G in ethanol, and the bottom trace is summed EMICCD counts of the 90-degree signal. Comparison of these three signals indicates that only single photon events, and not an entangled two-photon event, is present for the R6G. The y axis has been scaled and shifted for visualization.

To simulate fourth-order interferograms, the Fourier-transformed spectra of experimental interferograms are fitted to Gaussian peaks (Fig. B.1). The fitted spectrum is then used as the input spectrum for an entangled two-photon Michelson simulation (Fig. B.2). The bottom trace in Fig. 4.3 shows the summed spectrum collected at 90-degrees by the EMICCD. The interferogram follows that of a one-photon in-

terference from a single Gaussian peak, also depicted in Fig. B.1. If the collected signal originated from an entangled two-photon event, it would follow the pattern of the input state and exhibit a matching two-photon interference as the molecule would act similar to a coincidence counter [50].

4.4 Results: Wavelength-resolved measurements of Rhodamine 6G

The one-photon nature of the scattered signal is further confirmed by looking at the wavelength spectrum collected at 90-degrees (Fig. 4.4). The measured single photon fluorescence of R6G is shown for reference in purple. For the non-degenerate entangled photon spectrum (Fig. B.4), a scattered signal is measured that correlates with the wings of the spectrum, well away from the expected fluorescence spectrum. When a degenerate spectrum with a bandwidth centered at 800 nm is used, farther away from the R6G absorption tail, a reduced amplitude scatter at 800 nm is measured. The scattered spectrum that is measured is a convolution of the wavelength dependent molecular scattering cross section and the SPDC signal which is why it does not appear identical to Figure B.4. As a control, zinc tetraphenylporphyrin (ZnTPP) was measured because it has a narrow-band absorption at 400 nm that is ~ 200 nm from the SPDC spectrum as well as a much weaker absorption near 550 nm (aligned with R6G). No scattered signal was measured for ZnTPP within the sensitivity limit of our spectrometer, which may be expected because ZnTPP has a lower absorption cross section than R6G, but other factors regarding the nature of the scattering process may come into play. All light is transmitted within our error bars and Figure B.7 represents the dark count fluctuations of the EMICCD. At this point, the exact nature of the scattering mechanism is unknown, but the scattered spectrum and its single-photon time dependence are clearly measured.

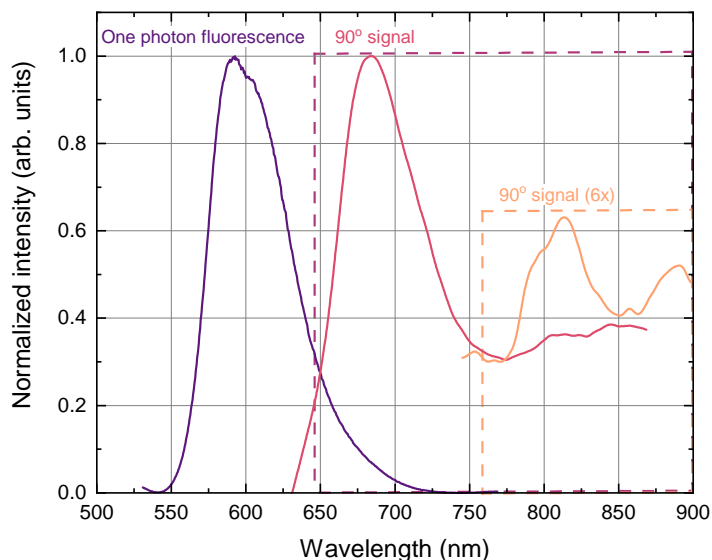


Figure 4.4: One photon fluorescence (purple trace) and the measured scatter spectra from 5mM R6G in ethanol for non-degenerate (pink trace) and degenerate (orange trace) entangled photons. The spectra have been normalized and scaled such that they can be displayed on similar scales. The scattered signal matches the entangled photon spectrum indicating that a one-photon process is present, and not fluorescence from an entangled two-photon process.

4.5 Results: Measured entangled photon interaction cross sections

The scattered cross section is calculated using the equation [26]:

$$S_E = \gamma * N_E * c * 10^{-6} * l * N_A * \sigma_E \quad (4.1)$$

where S_E is the collected scatter signal, γ is the collection efficiency, N_E is the incident entangled photon flux, c is the concentration in mM, l is the pathlength in cm, N_A is Avogadro's number, and σ_E is the entangled two-photon absorption cross section. The resulting scattered cross section is $2 \pm 1 * 10^{-21} \text{ cm}^2/\text{molecule}$. For comparison, the measured attenuation from a transmission spectrum (Fig. 4.5), the standard method of the field, yields a cross section of $4 \pm 1 * 10^{-21} \text{ cm}^2/\text{molecule}$ cross section (See the supplementary information for more information on the measurement). The agreement between the measured scattered cross section and the measured attenuation cross section further confirms that no entanglement enhanced two-photon absorption or fluorescence is measured.

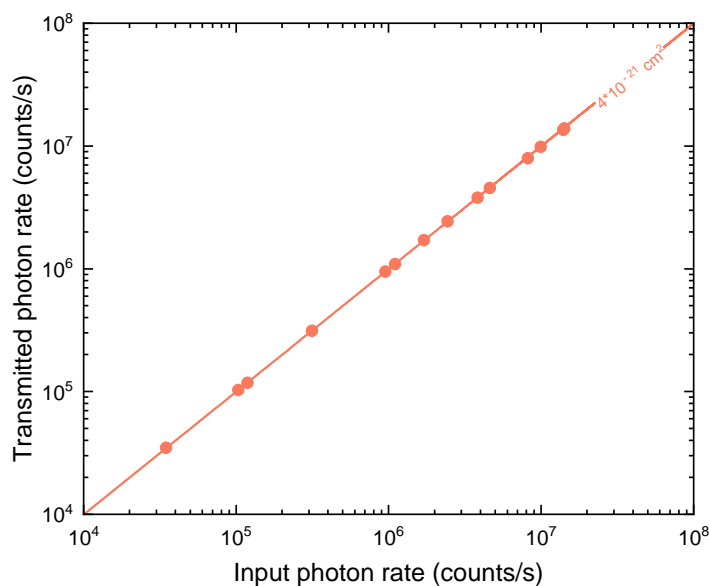


Figure 4.5: Measured transmitted photon rate (orange data points) and fit (orange solid line) vs input photon rate for 5mM Rhodamine 6G in water. Using the method standard in literature, the ETPA cross section from the measured absorption rate would be $4 \pm 1 \times 10^{-21} \text{ cm}^2/\text{molecule}$. However, from these experiments, the linear relationship is determined to not be from ETPA, but rather from a single photon scattering process. Note that the error bars for each data point are on the order of the graph point size.

4.6 Conclusion

Our measurements indicate that off- or near-resonant scattering can lead to inflated absorption cross sections in intensity counting transmission, coincidence, or fluorescence experiments. The measured values are also above the maximum theoretical ETPA cross sections for R6G from quantum-mechanical derivations ($3 \times 10^{-24} \text{ cm}^2/\text{molecule}$, dashed line in Fig. 4.1) [29]. The results are also in-line with the measurements of Parzuchowski et al. [27], where no signal was measured after extensive filtering and an ETPA cross section upper limit of $1.2 \times 10^{-25} \text{ cm}^2/\text{molecule}$ was established for R6G. Note again that our spectrometer is capable of measuring cross sections down to the $10^{-25} \text{ cm}^2/\text{molecule}$ range, so if present, a fluorescence event would be detectable by these guidelines. The $10^{-25} \text{ cm}^2/\text{molecule}$ sensitivity is estimated based on the noise floor of the detector and the maximum possible photon count before detector saturation. At this sensitivity, we estimate the maximum fluorescence count rate, including collection efficiency, to be approximately 5-10 photons/s. The linear dependence measurement of Fig. 4.5 also covers input

powers spanning four orders of magnitude, well beyond the intensity range reported in most manuscripts. The slope over this range is not completely linear but also not completely quadratic. If measured over a smaller range, the slope would appear linear, in agreement with previous reports. The scattered signal at 90 degrees, if not properly filtered, and measured sparsely, would also represent a signal that appears to match the entanglement time — emphasizing the importance of spectral and temporal measurements.

The measurements in this paper are performed on a virtual-state mediated two-photon excitable molecule. Recently, theoretical and experimental measurements have emphasized the importance of resonant or near resonant real states to achieve large two-photon entangled interactions [43, 44, 51]. The results of this paper indicate that caution must be taken when measuring entangled two-photon events because single-photon scattering and other reported single-photon processes such as hot band absorption [52] will mimic linear absorption at low power. Only by characterizing the entangled state, instead of relying solely on intensity measurements, can a definitive conclusion be reached. As the field of excited state entangled interactions continues to be explored, and molecules are synthesized to maximize entangled interactions, a standardized measurement scheme, such the one as presented here, is vital.

4.7 Experimental details

Broadband energy-time entangled photon pairs are generated via spontaneous parametric down-conversion of pump photons in a custom made periodically poled 8% MgO doped congruent lithium tantalate (CLT) bulk crystal (HC Photonics). The grating design is optimized for the Type-0 collinear quasi-phase matching condition and the poling period is $9.5 \mu\text{m}$. The design and characterization of the grating has been previously reported [42]. The crystal is pumped by a continuous wave diode laser that outputs 400 mW of 406 nm light with a linewidth of 1.5 nm (Coherent OBIS). The polarization state of the diode laser is conditioned with a polarization beamsplitter and half-wave plate (Thorlabs) before the beam is focused into the crystal with a UV fused silica plano-convex lens. The temperature of the ppLT grating is maintained at phase-matching temperatures to an accuracy of 10 mK with a heater and PID loop (Covesion). After creation, the entangled photon pairs are passed through a total of three OD-4 500nm longpass filters (Edmund Optics) to eliminate any residual 406 nm pump photons.

For the static transmission and 90-degree signal measurements, the SPDC flux is focused into a cuvette containing Rhodamine 6G and the transmission or 90-degree signal is collected with a lens system to image with a spectrometer and an electron multiplying intensified CCD camera (PIMAX4, Princeton Instruments). The pump power is varied with a continuously variable ND wheel (Thorlabs) and monitored with a power meter (Newport). Additional longpass filters ensured that stray pump photons did not reach the EMICCD.

Time-resolved entangled state characterization was performed by first collimating the entangled photon pairs with an off-axis parabolic mirror and cylindrical lens. Following the collimation optics, the entangled pairs are directed into a two-photon Michelson interferometer [47, 48]. This configuration is chosen over the Mach-Zehnder configuration as it enables a broader bandwidth of entangled photon pairs to be utilized in a simpler collinear geometry. A broadband, dispersion compensating beamsplitter (BS1, Layertec) probabilistically separates the entangled photon pairs and directs them to two sets of mirrors, which then reflect the photons such that they are spatially overlapped on the beamsplitter. In one arm, an achromatic quarter-wave plate (Thorlabs) rotates the polarization state of the entangled pairs. In the other arm, the optical path length is adjusted by scanning a mirror mounted on a translation stage (Newport), with a minimum $0.1 \mu\text{m}$ resolution that translates to a temporal resolution of 0.33 fs.

Coincidence counts are collected using a second broadband, dispersion compensating beamsplitter (Layertec) and two free-space-to-fiber setups that couple entangled photon pairs into single photon avalanche photodiodes (SPADs, Laser Component COUNT) connected to time-tagging electronics (PicoHarp 300). The free-space-to-fiber setups each consist of two mirrors to align the output paths of the second beamsplitter into a 4.51 mm focal length asphere (Thorlabs), which then focuses the SPDC into a multimode fiber ($105 \mu\text{m}$ core diameter, 0.22 NA). A 500 nm longpass filter is placed before the asphere to ensure that stray pump light is not collected. For fourth-order interference measurements, the coincidence time-bin resolution is set to 8 ps and a coincidence histogram is collected at each stage position over an integration time of 5 seconds. Accidental coincidence counts are calculated by averaging the tail of each histogram and subtracting the average value from the entire histogram. The coincidence counts are then summed within a 14 ns window.

A volumetric pipette (Eppendorf) was used to add absolute ethanol (Sigma-Aldrich) to a vial containing powdered Rhodamine 6G (Sigma-Aldrich) to achieve desired concentrations.

References

1. Jedrkiewicz, O., Blanchet, J.-L., Brambilla, E., Di Trapani, P. & Gatti, A. Detection of the Ultranarrow Temporal Correlation of Twin Beams via Sum-Frequency Generation. *Physical Review Letters* **108**, 253904. <https://link.aps.org/doi/10.1103/PhysRevLett.108.253904> (2019) (June 2012).
2. Bondani, M., Allevi, A., Zambra, G., Paris, M. G. A. & Andreoni, A. Sub-shot-noise photon-number correlation in a mesoscopic twin beam of light. *Physical Review A* **76**, 013833. <https://link.aps.org/doi/10.1103/PhysRevA.76.013833> (2021) (July 2007).
3. Brida, G., Genovese, M. & Ruo Berchera, I. Experimental realization of sub-shot-noise quantum imaging. *Nature Photonics* **4**, 227–230. <https://www.nature.com/articles/nphoton.2010.29> (2020) (Apr. 2010).
4. Giovannetti, V., Lloyd, S. & Maccone, L. Advances in quantum metrology. *Nature Photonics* **5**, 222–229. <https://www.nature.com/articles/nphoton.2011.35> (2020) (Apr. 2011).
5. Boto, A. N. *et al.* Quantum Interferometric Optical Lithography: Exploiting Entanglement to Beat the Diffraction Limit. *Physical Review Letters* **85**, 2733–2736. <https://link.aps.org/doi/10.1103/PhysRevLett.85.2733> (2022) (Sept. 2000).
6. Bornman, N., Prabhakar, S., Vallés, A., Leach, J. & Forbes, A. Ghost imaging with engineered quantum states by Hong–Ou–Mandel interference. *New Journal of Physics* **21**, 073044. <https://doi.org/10.1088%2F1367-2630%2Fab2f4d> (2020) (July 2019).
7. Aspden, R. S., Tasca, D. S., Boyd, R. W. & Padgett, M. J. EPR-based ghost imaging using a single-photon-sensitive camera. *New Journal of Physics* **15**, 073032. <https://doi.org/10.1088%2F1367-2630%2F15%2F7%2F073032> (2019) (July 2013).
8. Kviatkovsky, I., Chrzanowski, H. M., Avery, E. G., Bartolomaeus, H. & Ramelow, S. Microscopy with undetected photons in the mid-infrared. *Science Advances*. <https://www.science.org/doi/abs/10.1126/sciadv.abd0264> (2022) (Oct. 2020).
9. Padgett, M. J. & Boyd, R. W. An introduction to ghost imaging: Quantum and classical. *Philosophical transactions. Series A, Mathematical, physical, and engineering sciences* **375**. <https://www.ncbi.nlm.nih.gov/pmc/articles/PMC5487713/> (2019) (Aug. 2017).

10. Abouraddy, A. F., Stone, P. R., Sergienko, A. V., Saleh, B. E. A. & Teich, M. C. Entangled-Photon Imaging of a Pure Phase Object. *Physical Review Letters* **93**, 213903. <https://link.aps.org/doi/10.1103/PhysRevLett.93.213903> (2020) (Nov. 2004).
11. Pittman, T. B., Shih, Y. H., Strekalov, D. V. & Sergienko, A. V. Optical imaging by means of two-photon quantum entanglement. *Physical Review A* **52**, R3429–R3432. <https://link.aps.org/doi/10.1103/PhysRevA.52.R3429> (2019) (Nov. 1995).
12. Strekalov, D. V., Sergienko, A. V., Klyshko, D. N. & Shih, Y. H. Observation of Two-Photon “Ghost” Interference and Diffraction. *Physical Review Letters* **74**, 3600–3603. <https://link.aps.org/doi/10.1103/PhysRevLett.74.3600> (2019) (May 1995).
13. Li, B. & Hofmann, H. F. Energy-time entanglement and intermediate-state dynamics in two-photon absorption. *Physical Review A* **104**, 022434. <https://link.aps.org/doi/10.1103/PhysRevA.104.022434> (2022) (Aug. 2021).
14. Carnio, E., Buchleitner, A. & Schlawin, F. How to optimize the absorption of two entangled photons. *SciPost Physics Core* **4**, 028. <https://scipost.org/10.21468/SciPostPhysCore.4.4.028> (2022) (Oct. 2021).
15. Lerch, S. & Stefanov, A. Experimental requirements for entangled two-photon spectroscopy. *The Journal of Chemical Physics* **155**, 064201. <https://aip.scitation.org/doi/10.1063/5.0050657> (2022) (Aug. 2021).
16. Svidzinsky, A. *et al.* Enhancing stimulated Raman excitation and two-photon absorption using entangled states of light. *Physical Review Research* **3**, 043029. <https://link.aps.org/doi/10.1103/PhysRevResearch.3.043029> (2023) (Oct. 2021).
17. Lee, D.-I. & Goodson, T. Entangled Photon Absorption in an Organic Porphyrin Dendrimer. *The Journal of Physical Chemistry B* **110**, 25582–25585. <https://doi.org/10.1021/jp066767g> (2018) (Dec. 2006).
18. Dorfman, K. E., Schlawin, F. & Mukamel, S. Nonlinear optical signals and spectroscopy with quantum light. *Reviews of Modern Physics* **88**, 045008. <https://link.aps.org/doi/10.1103/RevModPhys.88.045008> (2018) (Dec. 2016).
19. Varnavski, O. & Goodson III, T. Two-photon fluorescence microscopy at extremely low excitation intensity: The power of quantum correlations. *Journal of the American Chemical Society*, jacs.0c01153. <https://pubs.acs.org/doi/10.1021/jacs.0c01153> (2020) (July 2020).
20. Ma, Y.-Z. & Doughty, B. Nonlinear Optical Microscopy with Ultralow Quantum Light. *The Journal of Physical Chemistry A* **125**, 8765–8776. <https://pubs.acs.org/doi/10.1021/acs.jpca.1c06797> (2022) (Oct. 2021).

21. Kim, J.-H., Aghaeimeibodi, S., Carolan, J., Englund, D. & Waks, E. Hybrid integration methods for on-chip quantum photonics. *Optica* **7**, 291. <https://www.osapublishing.org/abstract.cfm?URI=optica-7-4-291> (2022) (Apr. 2020).
22. Javid, U. A. *et al.* Ultrabroadband Entangled Photons on a Nanophotonic Chip. *Physical Review Letters* **127**, 183601. <https://link.aps.org/doi/10.1103/PhysRevLett.127.183601> (2022) (Oct. 2021).
23. Javanainen, J. & Gould, P. L. Linear intensity dependence of a two-photon transition rate. *Physical Review A* **41**, 5088–5091. <https://link.aps.org/doi/10.1103/PhysRevA.41.5088> (2019) (May 1990).
24. Dayan, B. Theory of two-photon interactions with broadband down-converted light and entangled photons. *Physical Review A* **76**, 043813. <https://link.aps.org/doi/10.1103/PhysRevA.76.043813> (2020) (Oct. 2007).
25. Georgiades, N. P., Polzik, E. S., Edamatsu, K., Kimble, H. J. & Parkins, A. S. Nonclassical Excitation for Atoms in a Squeezed Vacuum. *Physical Review Letters* **75**, 3426–3429. <https://link.aps.org/doi/10.1103/PhysRevLett.75.3426> (2020) (Nov. 1995).
26. Tabakaev, D. *et al.* Energy-time-entangled two-photon molecular absorption. *Physical Review A* **103**, 033701. <https://link.aps.org/doi/10.1103/PhysRevA.103.033701> (2021) (Mar. 2021).
27. Parzuchowski, K. M. *et al.* Setting Bounds on Entangled Two-Photon Absorption Cross Sections in Common Fluorophores. *Physical Review Applied* **15**, 044012. <https://link.aps.org/doi/10.1103/PhysRevApplied.15.044012> (2021) (Apr. 2021).
28. Landes, T. *et al.* Experimental feasibility of molecular two-photon absorption with isolated time-frequency-entangled photon pairs. *Physical Review Research* **3**, 033154. <https://link.aps.org/doi/10.1103/PhysRevResearch.3.033154> (2021) (Aug. 2021).
29. Landes, T. *et al.* Quantifying the enhancement of two-photon absorption due to spectral-temporal entanglement. *Optics Express* **29**, 20022–20033. <https://www.osapublishing.org/oe/abstract.cfm?uri=oe-29-13-20022> (2021) (June 2021).
30. Burdick, R. K., Schatz, G. C. & Goodson, T. Enhancing Entangled Two-Photon Absorption for Picosecond Quantum Spectroscopy. *Journal of the American Chemical Society*. <https://doi.org/10.1021/jacs.1c09728> (2021) (Oct. 2021).
31. Corona-Aquino, S. *et al.* Experimental study on the effects of photon-pair temporal correlations in entangled two-photon absorption. *arXiv:2101.10987 [physics, physics:quant-ph]*. <http://arxiv.org/abs/2101.10987> (2021) (Jan. 2021).

32. Harpham, M. R., Süzer, Ö., Ma, C.-Q., Bäuerle, P. & Goodson, T. Thiophene Dendrimers as Entangled Photon Sensor Materials. *Journal of the American Chemical Society* **131**, 973–979. <https://doi.org/10.1021/ja803268s> (2019) (Jan. 2009).
33. Guzman, A. R., Harpham, M. R., Süzer, Ö., Haley, M. M. & Goodson, T. G. Spatial Control of Entangled Two-Photon Absorption with Organic Chromophores. *Journal of the American Chemical Society* **132**, 7840–7841. <https://doi.org/10.1021/ja1016816> (2019) (June 2010).
34. Upton, L. *et al.* Optically Excited Entangled States in Organic Molecules Illuminate the Dark. *The Journal of Physical Chemistry Letters* **4**, 2046–2052. <https://pubs.acs.org/doi/10.1021/jz400851d> (2020) (June 2013).
35. Villabona-Monsalve, J. P., Calderón-Losada, O., Nuñez Portela, M. & Valencia, A. Entangled Two Photon Absorption Cross Section on the 808 nm Region for the Common Dyes Zinc Tetraphenylporphyrin and Rhodamine B. *The Journal of Physical Chemistry A* **121**, 7869–7875. <https://doi.org/10.1021/acs.jpca.7b06450> (2018) (Oct. 2017).
36. Villabona-Monsalve, J. P., Varnavski, O., Palfey, B. A. & Goodson, T. Two-Photon Excitation of Flavins and Flavoproteins with Classical and Quantum Light. *Journal of the American Chemical Society* **140**, 14562–14566. <https://doi.org/10.1021/jacs.8b08515> (2018) (Nov. 2018).
37. Eshun, A., Cai, Z., Awies, M., Yu, L. & Goodson, T. Investigations of Thienoacene Molecules for Classical and Entangled Two-Photon Absorption. *The Journal of Physical Chemistry A* **122**, 8167–8182. <https://doi.org/10.1021/acs.jpca.8b06312> (2018) (Oct. 2018).
38. Villabona-Monsalve, J. P., Burdick, R. K. & Goodson, T. Measurements of Entangled Two-Photon Absorption in Organic Molecules with CW-Pumped Type-I Spontaneous Parametric Down-Conversion. *The Journal of Physical Chemistry C*, [acs.jpcc.0c08678](https://pubs.acs.org/doi/10.1021/acs.jpcc.0c08678). <https://pubs.acs.org/doi/10.1021/acs.jpcc.0c08678> (2020) (Oct. 2020).
39. Shim, S., Stuart, C. M. & Mathies, R. A. Resonance Raman Cross-Sections and Vibronic Analysis of Rhodamine 6G from Broadband Stimulated Raman Spectroscopy. *ChemPhysChem* **9**, 697–699. <https://onlinelibrary.wiley.com/doi/abs/10.1002/cphc.200700856> (2022) (2008).
40. Makarov, N. S., Drobizhev, M. & Rebane, A. Two-photon absorption standards in the 550–1600 nm excitation wavelength range. *Optics Express* **16**, 4029–4047. <https://www.osapublishing.org/oe/abstract.cfm?uri=oe-16-6-4029> (2021) (Mar. 2008).
41. Albota, M. A., Xu, C. & Webb, W. W. Two-photon fluorescence excitation cross sections of biomolecular probes from 690 to 960 nm. *Applied Optics*

- 37, 7352–7356. <https://www.osapublishing.org/ao/abstract.cfm?uri=ao-37-31-7352> (2019) (Nov. 1998).
42. Szoke, S., He, M., Hickam, B. P. & Cushing, S. K. Designing high-power, octave spanning entangled photon sources for quantum spectroscopy. *The Journal of Chemical Physics* **154**, 244201. <https://aip.scitation.org/doi/10.1063/5.0053688> (2021) (June 2021).
43. Burdick, R. K. *et al.* Predicting and Controlling Entangled Two-Photon Absorption in Diatomic Molecules. *The Journal of Physical Chemistry A* **122**, 8198–8212. <https://doi.org/10.1021/acs.jpca.8b07466> (2018) (Oct. 2018).
44. Kang, G. *et al.* Efficient Modeling of Organic Chromophores for Entangled Two-Photon Absorption. *Journal of the American Chemical Society* **142**, 10446–10458. <https://doi.org/10.1021/jacs.0c02808> (2020) (June 2020).
45. Fischer, M. & Georges, J. Fluorescence quantum yield of rhodamine 6G in ethanol as a function of concentration using thermal lens spectrometry. *Chemical Physics Letters* **260**, 115–118. <https://www.sciencedirect.com/science/article/pii/000926149600838X> (2022) (Sept. 1996).
46. Zehentbauer, F. M. *et al.* Fluorescence spectroscopy of Rhodamine 6G: Concentration and solvent effects. *Spectrochimica Acta Part A: Molecular and Biomolecular Spectroscopy* **121**, 147–151. <https://www.sciencedirect.com/science/article/pii/S1386142513012195> (2021) (Mar. 2014).
47. Lavoie, J. *et al.* Phase-Modulated Interferometry, Spectroscopy, and Refractometry using Entangled Photon Pairs. *Advanced Quantum Technologies* **3**, 1900114. <https://onlinelibrary.wiley.com/doi/abs/10.1002/qute.201900114> (2022) (2020).
48. Lopez-Mago, D. & Novotny, L. Coherence measurements with the two-photon Michelson interferometer. *Physical Review A* **86**, 023820. <https://link.aps.org/doi/10.1103/PhysRevA.86.023820> (2020) (Aug. 2012).
49. Shoji, I., Kondo, T., Kitamoto, A., Shirane, M. & Ito, R. Absolute scale of second-order nonlinear-optical coefficients. *Journal of the Optical Society of America B* **14**, 2268. <https://opg.optica.org/abstract.cfm?URI=josab-14-9-2268> (2022) (Sept. 1997).
50. Varnavski, O., Pinsky, B. & Goodson, T. Entangled Photon Excited Fluorescence in Organic Materials: An Ultrafast Coincidence Detector. *The Journal of Physical Chemistry Letters* **8**, 388–393. <https://doi.org/10.1021/acs.jpcllett.6b02378> (2020) (Jan. 2017).

51. Gu, B., Keefer, D. & Mukamel, S. Wave Packet Control and Simulation Protocol for Entangled Two-Photon Absorption of Molecules. *Journal of Chemical Theory and Computation* **18**, 406–414. <https://doi.org/10.1021/acs.jctc.1c00949> (2022) (Jan. 2022).
52. Mikhaylov, A. *et al.* Hot-Band Absorption Can Mimic Entangled Two-Photon Absorption. *The Journal of Physical Chemistry Letters* **13**, 1489–1493. <https://doi.org/10.1021/acs.jpcllett.1c03751> (2023) (Feb. 2022).

Chapter 5

ENTANGLED PHOTON CORRELATIONS ALLOW A
CONTINUOUS-WAVE LASER DIODE TO MEASURE SINGLE
PHOTON, TIME-RESOLVED FLUORESCENCE

ABSTRACT

Fluorescence lifetime experiments are a standard approach for measuring excited state dynamics and local environment effects. Here, we show that entangled photon pairs produced from a continuous-wave (CW) laser diode can replicate pulsed laser experiments without phase modulation. As a proof of principle, picosecond fluorescence lifetimes of indocyanine green are measured in multiple environments. The use of entangled photons has three unique advantages. First, low power CW laser diodes and entangled photon source design lead to straightforward on-chip integration for a direct path to distributable fluorescence lifetime measurements. Second, the entangled pair wavelength is easily tuned by adjusting the temperature or electric field, allowing a single source to cover octave bandwidths. Third, femtosecond temporal resolutions can be reached without requiring major advances in source technology or external phase modulation. Entangled photons could therefore provide increased accessibility to time-resolved fluorescence while also opening new scientific avenues in photosensitive and inherently quantum systems.

Most of this chapter has been reproduced with permission from:

Harper, N. *et al.* Entangled Photon Correlations Allow a Continuous-Wave Laser Diode to Measure Single-Photon, Time-Resolved Fluorescence. *The Journal of Physical Chemistry Letters*. Publisher: American Chemical Society, 5805–5811. <https://doi.org/10.1021/acs.jpcllett.3c01266> (2023) (June 2023).

5.1 Introduction

Time-resolved fluorescence spectroscopy is routinely used in laboratory and clinical settings to measure excited state dynamics and, just as importantly, how changes to the lifetime provide information about the local environment surrounding the fluorophore [1, 2]. The advent of inexpensive pulsed laser diodes has led to a proliferation of time-domain fluorescence lifetime techniques in biosensing and microscopy beyond initial physical chemistry applications. Measured lifetimes are intrinsically fluorophore-specific and depend on variations in the surrounding chemical environment, such as temperature [3], pH [4], neighboring fluorophores [5], and the quantum state [6–9]. This specificity, alongside developments in highly fluorescent tagging proteins and molecular markers, has also enabled fluorescence lifetime imaging microscopy (FLIM) to become a ubiquitous technique to visualize and understand complex biological samples [10, 11]. Autofluorescence endogenous to cellular environments has permitted label-free FLIM medical imaging applications, including clinical cancer diagnosis [12–14].

The next logical frontier for time-resolved fluorescence is highly distributable, wearable devices [15, 16]. At these spatial scales and cost targets, the same pulsed lasers that enabled proliferation of laboratory measurements become a barrier. While on-chip pulsed lasers are being developed, most still require an external power source for the diode or pulse generation [17]. Further, the short on-chip cavity lengths lead to GHz repetition rates that do not give sufficient time for fluorophores to fully relax between pulses [18]. To date, on-chip pulses are mostly in the picosecond range, although recent publications have shown pulses as short as 350 fs [19]. These integrated pulsed lasers typically have a narrow wavelength tuning range, which can make measurements of multiple fluorescent probes or dynamics from multiple local environments difficult [20].

An intriguing alternative to pulsed lasers is to leverage the inherent quantum correlations between entangled photons in a pair. When one high-energy pump photon splits into a pair of two lower-energy entangled photons through spontaneous parametric down-conversion (SPDC), the two single photons are deterministically correlated in time [21]. Thus, if one photon is used to excite a fluorophore, coincidence detection of the resulting fluorescence with the other entangled photon provides a measurement of the time-resolved fluorescence [22]. The uncertainty in the temporal width of the photon pair wave packet can range from tens [23–25] to hundreds [21] of femtoseconds, enabling time-resolved measurements comparable

to those made with tabletop classical pulsed lasers. It is also key to note that, unlike continuous-wave (CW) phase modulation spectroscopy [26], a high frequency modulator is not needed for this technique due to its utilization of the inherent correlations between two entangled photons.

Given that classical time-resolved fluorescence instruments are also limited by detector bandwidths and timing circuits, CW entangled photon sources provide comparable experiments but with a few interesting technological advantages. First, it is straightforward to fabricate on-chip entangled photon sources that require only microwatts of power from a CW laser diode [27, 28]. Second, the wavelengths of the SPDC photons can be tuned across the transparency range of the down-conversion crystal, usually from UV to near-IR, by varying the phase matching conditions, either by heating the crystal or by tuning the pump wavelength, enabling a range of biosensing and physical chemistry experiments [29]. Finally, femtosecond temporal resolutions can be reached without requiring major advances in external phase modulation or detection technology. Scientifically, given that the entangled photon measurements are natively performed in a single-photon-per-measurement regime, the technique is also interesting for measuring photosensitive samples [30], studying quantum systems [31], or exploring scaling behaviors of various properties against incidence flux [32, 33].

Despite early theoretical interest in utilizing entangled pairs to perform lifetime measurements [22, 34, 35], an experimental demonstration using a CW laser has not yet been published¹. We therefore provide a proof-of-principle experiment by measuring the fluorescence lifetime of indocyanine green (ICG). The correlation time of the entangled photon source is < 30 fs [25], but the detector used limits temporal resolution to 50 ps and minimum measurable lifetime to 365 ps [36]. The excited-state lifetimes of ICG in three solvents are measured to check the accuracy of the technique against previously published work [37]. Through a statistical analysis we show that, even though limited by the MHz detector maximum count rates and bandwidth, integration times in the minutes range provide sufficient signal for accurate lifetime determination using this configuration. Our results demonstrate that measuring time-resolved fluorescence from entangled photons is possible with properties approaching pulsed lasers, providing the proof of principle for new modalities of compact time-resolved fluorescence spectroscopy and experiments in a single-photon excitation and single-photon detection limit. Periodically poled

¹At the time of this publication, we became aware of Ted Laurence's unpublished work using a similar method for microscopy.

entangled photon sources routinely approach THz pair generation rates, so commercially available picosecond detectors with GHz count rates can improve these measurements to femtosecond temporal resolution and seconds integration time. Future developments could also perform highly multiplexed measurements using the additional correlated properties of SPDC such as the momentum or angular degree of freedom, as proposed in Ref. [22].

5.2 Experimental overview

The experimental configuration for performing fluorescence lifetime measurements with entangled photon pairs is shown in Fig. 5.1, and a detailed description of all components is provided in the Experimental Details section. Briefly, 2 mW of power from a 402.5 nm CW laser diode pumps a periodically poled, Type-0 SPDC crystal to generate entangled photon pairs spanning 720 nm to 913 nm. Here, the pump laser power is significantly reduced using neutral density filters to avoid saturating the single photon counting detectors. The periodically poled bulk source used here produces free-space pairs, adding down-stream losses due to collimation and fiber coupling. A waveguided equivalent would enable the same studies to be performed on-chip and with μ W pump powers.

The energies of the photons in the entangled pair sum to that of the pump laser. For the entangled photon source used, one photon has a wavelength between 720 – 805 nm with a simultaneously produced conjugate photon between 805 – 913 nm. The resulting correlation time from this bandwidth is ~ 30 fs, comparable to the pulse width of state-of-the-art mode locked lasers [38]. The detectors used in this experiment have a larger timing jitter (3.65 ns) than the temporal characteristics of the source and ultimately determine the experimental temporal resolution, as explained later in more detail.

The entangled photon pairs are then deterministically split using a short-pass dichroic filter tuned to 805 nm. The reflected lower energy photon heralds the measurement when it is detected by a single photon counting avalanche detector (SPAD), starting the timer for a time-correlated single-photon-counting (TCSPC) circuit. The higher energy photon is sent to the sample, where it excites a single molecule that then emits a single fluorescence photon with some delay. The fluorescence photon is collected in an epifluorescence scheme and then detected by another SPAD, which stops the timer on the TCSPC board. The time delay between the heralding and fluorescence photon detections is recorded over multiple measure-

ments to create a histogram of such time differences, from which the fluorescence lifetime can be extracted.

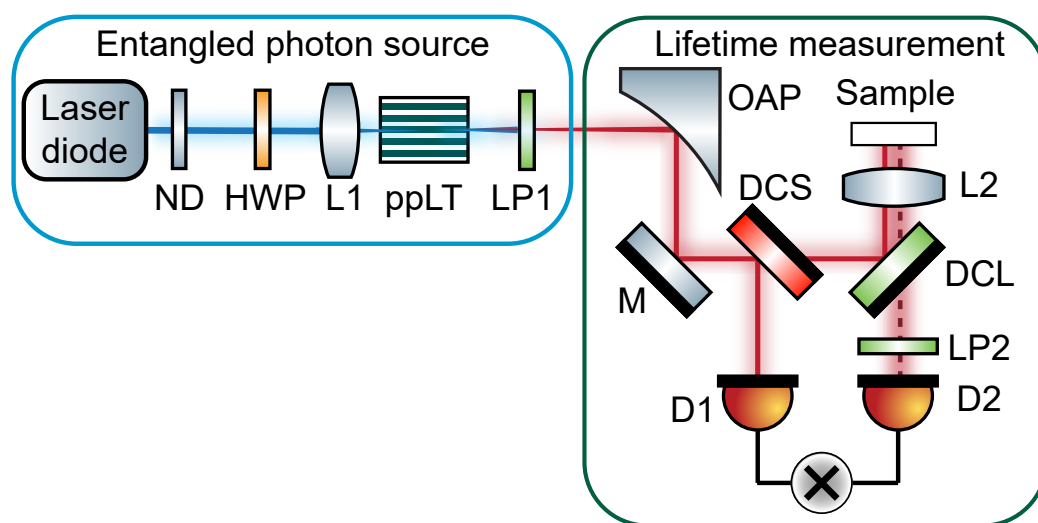


Figure 5.1: Experimental configuration for measuring fluorescence lifetimes with energy-time entangled photon pairs. The broadband entangled photon source consists of a 402.5 nm laser diode that is focused into a periodically poled lithium tantalate crystal. The resulting entangled photons (solid red lines) are collimated with an off-axis parabolic mirror and then separated by wavelength with a dichroic mirror. One photon from the entangled pair is directed to a detector to herald the measurement while the other is focused onto a molecular sample with a high numerical aperture (NA) aspheric lens. The lens collects the backwards emission from the sample's fluorescence (dashed red line) which is then directed through a series of long-pass filters onto a second detector. A coincidence circuit generates histograms of the arrival times between the reference and fluorescence photons. Abbreviations: ND: neutral density filters, HWP: half-wave plate, L1: UVFS focusing lens, ppLT: periodically poled lithium tantalate grating, LP1: 500 nm long-pass filter, OAP: off-axis parabolic mirror, M: mirror, DCS: dichroic short-pass mirror with cut-on wavelength 805 nm, DCL: dichroic short-pass mirror with cut-on wavelength 810 nm, L2: high-NA aspheric lens, LP2: 808 nm long-pass filter, D1 and D2: multi-mode fiber coupled single photon avalanche photodiodes connected to a coincidence circuit.

The molecular dye indocyanine green (ICG) is used as a proof of principle since it is commonly utilized to perform fluorescence imaging in biological and clinical settings [39, 40]. ICG also has appropriate spectral properties relative to the entangled photon source and a well-characterized lifetime dependence on the solvent environment [37]. Methanol, ethanol, and dimethylsulfoxide (DMSO) were selected

as solvents due to their variation of the ICG lifetime by hundreds of picoseconds. The absorption wavelength, emission wavelength, and quantum yield change only slightly across the three solvents (Table C.1). The spectrum of the SPDC was tuned through the phase matching temperature to maximize spectral overlap with the sample (Fig. 5.2a). The resulting ICG fluorescence (Fig. 5.2b) is separated from the excitation beam with a long-pass dichroic mirror and further filtered with an OD6 long-pass interference filter. The instrument response function (IRF, Fig. 5.2b), which characterizes the response that would be measured by a sample with an infinitely short lifetime, was obtained by replacing the sample with a mirror and removing the final long-pass OD6 filter to allow part of the excitation flux to reach the second detector. The IRF spectrum is altered from the excitation spectrum because it has been filtered by the dichroic mirror, but this alteration has minimal impact on the time-domain response due to the minimal wavelength sensitivity of the SPADs used here.

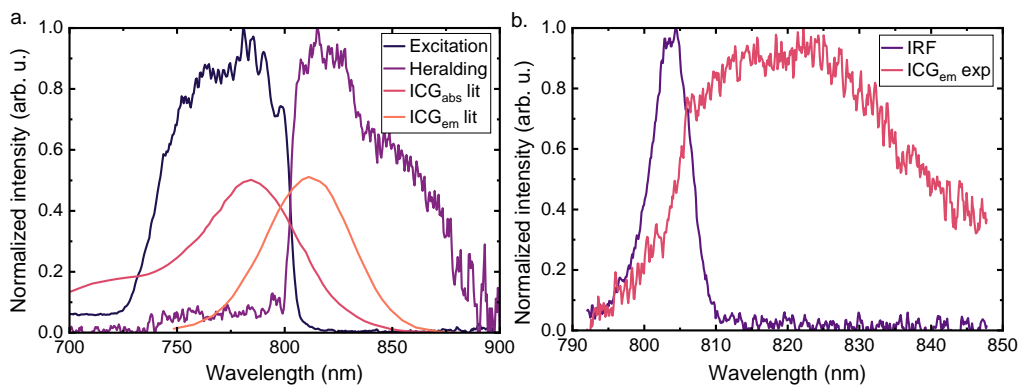


Figure 5.2: Spectral properties of the entangled photons and indocyanine green. (a) Normalized spectra of the entangled photons used for the heralding and excitation photons compared to the normalized absorption/emission spectra for ICG in methanol from Ref. [37]. The ICG spectra have been further scaled by 50% to distinguish them from the entangled photon spectra. (b) Normalized fluorescence signal from $100\mu\text{M}$ ICG in methanol following entangled photon excitation compared to the portion of entangled photon flux that is used to characterize the instrument response function.

The timing uncertainty broadens the detection of the fluorescence photons by the total IRF. The current temporal resolution of the experiment is limited by the timing uncertainty of the detection electronics, just as with most pulsed laser experiments.

The measured histograms $R(t)$ are described by a convolution of the sample's temporal response $S(t)$ with the IRF:

$$R(t) = IRF(t) * S(t) = \int_{-\infty}^t IRF(t - t')S(t')dt'. \quad (5.1)$$

After a measurement, the fluorophore lifetime is fit by the sample response function that will give the best match to the measured experimental data. Here, that is a single exponential, but a more complex function could be used if a mixture of lifetimes is present and sufficiently fast detectors are used. Therefore, conceptually, the data produced is analogous to TCSPC with a pulsed laser.

From previous theoretical analysis, the minimum fluorescence lifetime that can be measured before deviation in the fit lifetime occurs is approximately 10% of the IRF width [36]. The IRF width in this experiment is approximately 3.65 ns, limiting our instrument to lifetime measurements greater than 365 ps. The counting circuit used here has a minimum time bin width of 4 ps with a 12 ps electrical time resolution; thus the primary factor in the 3.65 ns IRF width is the SPAD timing jitter. It should be noted that detectors with picosecond timing jitter and GHz count rates are commercially available but were not available to our lab at the time of this experiment. The central moment of the IRF drifts over time, in this case with a 50 ps standard deviation over 20 minutes; therefore, all lifetimes measured using this approach are reported with this level of uncertainty. The relevant characteristic timescales for this experiment are summarized in Table 5.1.

Experiment timescale	SPAD dead time	IRF width ²	Minimum measurable lifetime ³	IRF drift (20 minute interval) ⁴	Standard error of lifetime fit
Time (ns)	43	3.65	0.365	0.050	0.003

Table 5.1: Summary of relevant experimental timescales from instrument parameters.

²This IRF width is mainly due to SPAD jitter.

³Based on calculations from Ref. [36] that the minimum measurable lifetime is $\sim 10\%$ of the IRF width.

⁴Detector drift results in a small variation of the IRF center value that ultimately limits the temporal resolution of the measurements. The reported fluorescence lifetimes are reported with this value as the standard deviation.

5.3 Results: TCSPC histograms and lifetimes

The TCSPC histograms for ICG in three solvents, the IRFs, and the fits of the fluorescence lifetime are shown in Fig. 5.3abc. The measured TCSPC histograms for ICG in different solvents are shifted and broadened due to the nonzero lifetime. This broadening is more pronounced in DMSO compared to methanol and ethanol because of the longer ICG lifetime in this solvent. The ICG excited state lifetimes from fitting are presented in Table 5.2 and the exponential decays corresponding to these lifetimes are shown in Fig. 5.3d. The measured lifetimes agree with previously reported values [37] within error. The near-unity χ^2 values and uncorrelated weighted residuals Fig. C.4) indicate a satisfactory fit. The standard deviation of the measurements for all experiments are reported as 50 ps due to detector drift, which is larger than the 3 ps standard errors from the fit. The curves in Fig. 5.3abc are normalized and background subtracted for clarity. The raw experimental data plotted on a logarithmic scale are also available in Fig. C.3. An experiment where the sample is replaced by a blank cuvette of methanol does not yield a measurable coincidence peak Fig. C.1.

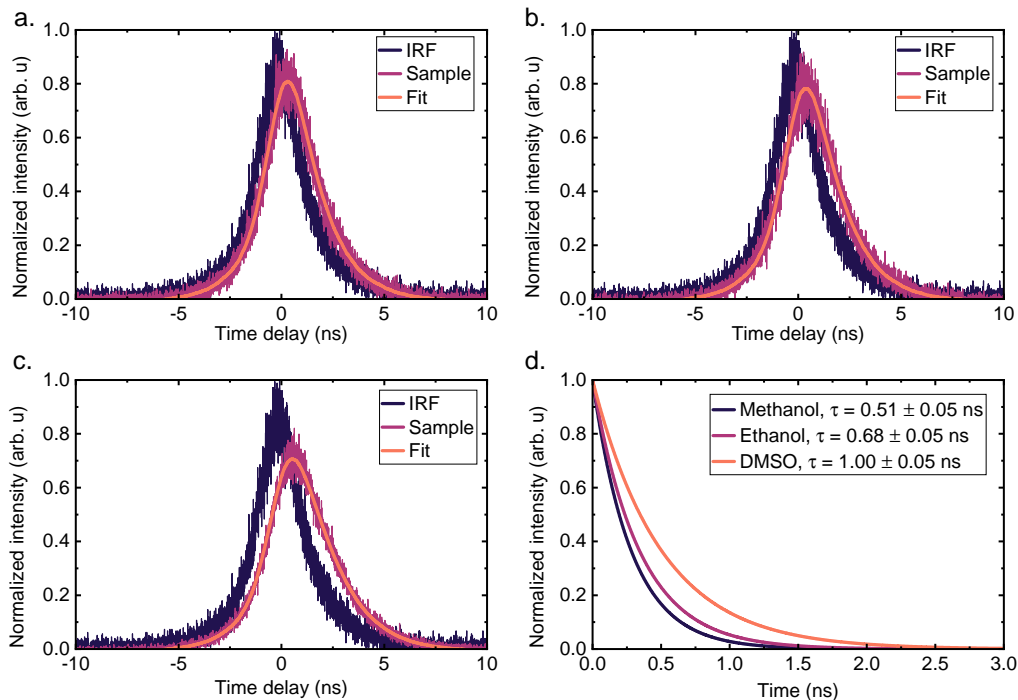


Figure 5.3: Normalized instrument response, TCSPC histogram, and fit of the histogram for ICG in methanol (a), ethanol (b), and DMSO (c). (d) Normalized fluorescence lifetime decays of ICG in each solvent reconstructed from the TCSPC fit lifetime and a single-exponential model.

Solvent	Reported lifetime (ns)	Measured lifetime(ns)	χ^2 statistic
Methanol	0.51	0.56 ± 0.05	1.003
Ethanol	0.62	0.68 ± 0.05	0.975
DMSO	0.97	1.00 ± 0.05	1.019

Table 5.2: Fluorescence lifetimes for ICG in solutions of methanol, ethanol, and DMSO previously characterized in Ref. [37], as well as the lifetimes measured in this work and the fitting statistic.

5.4 Results: Measurement statistics

The practicality of entangled photons for fluorescence lifetime measurements should also be quantified. Due to the Poissonian statistics of photon counting, the signal-to-noise ratio is expected to scale according to \sqrt{N} , where N is the number of true coincident photon events recorded. The number of coincidences can be increased either by increasing the SPDC flux or by increasing the integration time of each

histogram. To verify the noise statistics, the fit procedure was repeated on one-minute subsets of a 14 hour DMSO dataset (Fig. 5.4). As expected, the uncertainty in the fitted lifetime in DMSO scales proportionally to $N^{-0.53 \pm 0.01}$, close to the expected $N^{-1/2}$ (Fig. 5.4). For each sampling interval, the dataset was binned and a fit was performed on each of the resulting histograms. The resulting standard deviation of the inferred lifetimes was recorded. The increasing uncertainty in the standard deviation at long integration times originates from the smaller sample sizes.

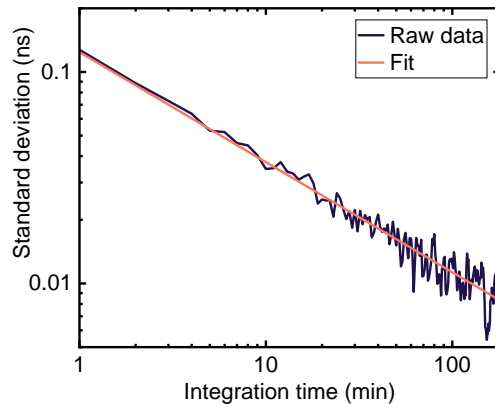


Figure 5.4: Standard deviation of the fit lifetime with respect to integration time for ICG in DMSO.

Figure 5.4 suggest that integration times on the order of several minutes would be sufficient for lifetime determination with a 10% uncertainty, based on the detectors used here that saturate at 10^6 photons/s fluxes. The integration time could be reduced to < 1 minute by using higher count rate detectors, such as those that can reach 10^9 photon/s, given that the pair rate of the experimental entangled source could have been increased by over two orders of magnitude. Theoretically, only ~ 200 coincidences are necessary for single exponential decay lifetimes to be determined with 10% uncertainty when the IRF is shorter than the molecular lifetime [41], potentially further lowering the experimental integration time to below 1 second, closer to current microscopic techniques. Using coincidence counting also leads to rejection of background, classical photons on the order of 1,000 : 1, making the scheme feasible even in sun-lit and room-lit conditions [42].

The proposed technique is therefore aptly timed with the rapidly evolving world of photon counting detector technology [43–45], especially given that THz flux entangled photon sources are already feasible. Figure 5.4 provides evidence that

the use of GHz bandwidth detectors coupled with high efficiency (10^{-6}) entangled photon sources would allow for reasonable integration times even with $\sim \mu\text{W}$ power CW laser diodes. Thus, the technique presented here has multiple interesting outlooks compared to conventional pulsed laser TCSPC or CW-modulated fluorescence lifetime measurements, whether it is used for on-chip technology advances, investigation of dynamics in the single-photon excitation limit, or exploration of the ability of quantum systems and molecules to preserve incident quantum states of light.

It is important to note, however, that this method is fundamentally limited by the need to time every heralding photon, regardless of whether a fluorescence photon is detected. Practically, this means that the maximum SPDC rate is limited to the inverse of the detector dead time or molecular lifetime, whichever is larger, and the flux that contributes to the measurement will be reduced by the detector inefficiency. As a result, the count rate of fluorescence events will be restricted by the maximum SPDC flux and the probability of converting excitation photons to fluorescence detection events, which is a function of both molecular and instrumental parameters. Currently, entangled photon pair rates in the THz range can be produced, whereas state of the art photon counting detectors and molecular lifetimes imply sub-GHz pair rates are necessary. Regardless of technology advancements, this upper limit could be surpassed by multiplexing on an EMICCD or SPAD array as proposed in Ref. [22], which would allow the full potential of THz-rate entangled sources to be used.

5.5 Conclusion

In conclusion, we have demonstrated that molecular excited state lifetimes can be measured using the temporal correlations of entangled photons produced from a CW laser. The solvent-dependent lifetime of indocyanine green was measured in methanol, ethanol, and DMSO in agreement with previous reports using pulsed lasers. The low pump flux needed for SPDC provides a direct route to time-resolved fluorescence measurements using on-chip, CMOS compatible photonics. Multiple waveguides and temperature tuning of phase matching can be used in the future to quickly measure a wide range of fluorophores from a single SPDC source and a photonic circuit. Overall, using a CW laser diode as a pump source opens new horizons for performing complex spectroscopic and microscopic studies with quantum light sources.

5.6 Experimental details

Broadband entangled pairs are generated in a periodically poled crystal whose design and characterization, as well as its use in studying entangled light-matter interactions, has been reported previously [25, 46]. In short, photon pairs are generated by Type-0 spontaneous parametric down-conversion in a third-order periodically poled 8% MgO-doped congruent lithium tantalate (CLT) bulk crystal (HC Photonics). The crystal is pumped with a continuous wave diode laser with a maximum power of 400 mW at 402.5 nm and FWHM linewidth of 1 nm (Coherent OBIS). The pump polarization is conditioned with a polarizing beamsplitter (Thorlabs PBSW-405) and half-wave plate (Thorlabs WPH10M-405) before being focused through the SPDC crystal with a 40 cm focal length UV-fused silica lens (Eksma Optics). The temperature of the crystal and subsequent entangled photon bandwidth and spectrum is set and maintained using a chip heater and PID loop with an accuracy of 10mK (Covesion). For measurements of indocyanine green (ICG, Sigma Aldrich) the crystal was heated to 75.0°C to tune the SPDC to a nondegenerate spectrum where the low-wavelength photons overlap with the ICG absorption curve. A series of 500nm OD 4 long-pass (Edmund Optics #84-706) and spatial filters (irises) remove any remaining pump photons and select the entangled photon pairs that are collinear with the pump beam.

Following the filters, the entangled photons are collimated with an off-axis parabolic mirror (Thorlabs) and directed to a short-pass dichroic mirror with a nominal cut-on wavelength of 800 nm (Edmund Optics #69-196). The incidence angle of the dichroic mirror is fine-tuned with a rotation mount (Thorlabs RP005) to increase the cut-on wavelength to 805 nm, the degenerate wavelength of the pairs, as measured with a grating spectrometer (Princeton Instruments IsoPlane SCT-320, 150 gr/mm grating with 800 nm blaze) and electron multiplying intensified charge-coupled device (EMICCD, Princeton Instruments PIMAX4). The reflected flux (805 nm – 913 nm) is fiber-coupled into a multimode fiber (105 μ m core, 0.22 NA, M43L01) using two mirrors and a 4.51 mm focal length aspheric lens (Thorlabs C230TMD-B) and serves as the herald for the experiment. The transmitted flux is directed to a long-pass dichroic mirror with a nominal cut-on wavelength of 800 nm (Edmund Optics #69-883) and serves as the excitation for the sample. The angle of this dichroic mirror is also fine-tuned with a rotation mount (Thorlabs RP005) such that the transmission is > 810 nm so that the passband does not overlap with that of the first dichroic mirror. A high-NA 4.51 mm focal length aspheric lens (Thorlabs C230TMD-B) focuses the excitation photons into a 1 mm path length quartz cuvette

(Helma/Millipore Sigma) containing $\sim 300\mu\text{L}$ of $100\mu\text{M}$ ICG in solution. The cuvette is mounted onto a micrometer-driven linear stage to precisely control the position of the sample relative to the focus of the excitation beam. The resulting fluorescence is collected through the long-pass dichroic and coupled into a second SPAD using with two mirrors, a 9.2 mm diameter, 4.51 mm focal length aspheric lens (Thorlabs C230TMD-B), and a multimode fiber ($105\mu\text{m}$ core, 0.22 NA, M43L01). An OD6 808 nm long-pass filter (Semrock LP02-808RE-25) following the dichroic mirror filters any remaining SPDC photons and/or scatter from the fluorescence signal. For the IRF measurements, the sample cuvette was replaced with a mirror, which was positioned so the excitation beam was focused at the surface of the mirror. Differences in pathlength due to the missing glass of the cuvette are estimated to introduce a 5 ps error, which is below the resolution of this experiment. Black cardboard boxes are positioned to block the sample from any pump scatter and minimize background.

Spectral measurements of the heralding and fluorescence photons were performed by collimating the output of the fibers and directing the image onto the spectrometer/EMICCD. The spectrum of the excitation photons was measured similarly by replacing the sample with a multimode fiber with a micrometer-driven x/y translation mount. This same scheme was used with coincidence counting to estimate the number of heralded excitation photons arriving at the sample.

Lifetime measurements were performed by connecting the multimode fibers to SPADs (Laser Components Count) and a coincidence counting circuit (PicoQuant PicoHarp 300). For these experiments, the SPDC between 805 and 912 nm served as the heralding trigger, and the SPAD output was connected to the sync channel of the counting circuit in a forward start-stop mode. The detection events of the fluorescence SPAD served as the stop signal for the experiment, and the SPAD output was connected to the CH1 input of the counting circuit. An electronic delay of 30 ns between the arms was implemented through the counting circuit. This offset is subtracted from the time axis of Figure 5.3(abc) for clarity but is not removed from the raw data in the supplementary information. Neutral density filters were used to decrease pump power and resulting SPDC flux to minimize lost heralding events due to the dead-time of the detectors (43 ns). For lifetime measurements, the number of singles in the heralding arm was approximately $1 * 10^5$ counts/s, and the number of singles in the fluorescence arm was approximately 600 counts/s. Data collection consists of repeatedly collecting histograms for 60 seconds, with a

series of 10 measurements of the singles rates in each channel measured between each histogram to monitor drift in the alignment. For the methanol, ethanol, and DMSO scans, 840, 840, and 960 histograms were collected, resulting in a total experiment time of 14, 14, and 16 hours, respectively. The instrument response function was measured over 240 coincidence histograms for a total of 6 hours. A custom MATLAB fitting routine is used to determine the characteristic excited state lifetime using the iterative reconvolution approach [47]. In this technique, the single-exponential sample response function is varied so that its convolution with the IRF best matches the measured histograms by minimizing the sum of squared errors.

References

1. Cundall, R. *Time-Resolved Fluorescence Spectroscopy in Biochemistry and Biology* ISBN: 978-1-4757-1634-4 (Springer Science & Business Media, Nov. 2013).
2. Bright, F. V. & Munson, C. A. Time-resolved fluorescence spectroscopy for illuminating complex systems. *Analytica Chimica Acta* **500**, 71–104. <https://www.sciencedirect.com/science/article/pii/S0003267003007232> (2023) (Dec. 2003).
3. Sumitani, M., Nakashima, N., Yoshihara, K. & Nagakura, S. Temperature dependence of fluorescence lifetimes of trans-stilbene. *Chemical Physics Letters* **51**, 183–185. <https://www.sciencedirect.com/science/article/pii/0009261477853815> (2023) (Oct. 1977).
4. Islam, M. S., Honma, M., Nakabayashi, T., Kinjo, M. & Ohta, N. pH Dependence of the Fluorescence Lifetime of FAD in Solution and in Cells. *International Journal of Molecular Sciences* **14**, 1952–1963. <https://www.mdpi.com/1422-0067/14/1/1952> (2023) (Jan. 2013).
5. Sekar, R. B. & Periasamy, A. Fluorescence resonance energy transfer (FRET) microscopy imaging of live cell protein localizations. *The Journal of Cell Biology* **160**, 629–633. <https://www.ncbi.nlm.nih.gov/pmc/articles/PMC2173363/> (2023) (Mar. 2003).
6. Frimmer, M., Chen, Y. & Koenderink, A. F. Scanning Emitter Lifetime Imaging Microscopy for Spontaneous Emission Control. *Physical Review Letters* **107**, 123602. <https://link.aps.org/doi/10.1103/PhysRevLett.107.123602> (2023) (Sept. 2011).
7. Schell, A. W. *et al.* Scanning Single Quantum Emitter Fluorescence Lifetime Imaging: Quantitative Analysis of the Local Density of Photonic States. *Nano Letters* **14**, 2623–2627. <https://doi.org/10.1021/nl500460c> (2023) (May 2014).

8. Inam, F. A. *et al.* Emission and Nonradiative Decay of Nanodiamond NV Centers in a Low Refractive Index Environment. *ACS Nano* **7**, 3833–3843. <https://doi.org/10.1021/nn304202g> (2023) (May 2013).
9. Dunn, T. J., Walmsley, I. A. & Mukamel, S. Experimental Determination of the Quantum-Mechanical State of a Molecular Vibrational Mode Using Fluorescence Tomography. *Physical Review Letters* **74**, 884–887. <https://link.aps.org/doi/10.1103/PhysRevLett.74.884> (2023) (Feb. 1995).
10. Datta, R., Heaster, T. M., Sharick, J. T., Gillette, A. A. & Skala, M. C. Fluorescence lifetime imaging microscopy: Fundamentals and advances in instrumentation, analysis, and applications. *Journal of Biomedical Optics* **25**, 071203. <https://www.spiedigitallibrary.org/journals/journal-of-biomedical-optics/volume-25/issue-7/071203/Fluorescence-lifetime-imaging-microscopy--fundamentals-and-advances-in-instrumentation/10.1117/1.JBO.25.7.071203.full> (2023) (May 2020).
11. Becker, W. Fluorescence lifetime imaging – techniques and applications. *Journal of Microscopy* **247**, 119–136. <https://onlinelibrary.wiley.com/doi/abs/10.1111/j.1365-2818.2012.03618.x> (2023) (2012).
12. Wang, Z. *et al.* Applications of fluorescence lifetime imaging in clinical medicine. *Journal of Innovative Optical Health Sciences* **11**, 1830001. <https://www.worldscientific.com/doi/10.1142/S179354581830001X> (2023) (Jan. 2018).
13. Blondel, W. *et al.* Spatially-Resolved Multiply-Excited Autofluorescence and Diffuse Reflectance Spectroscopy: SpectroLive Medical Device for Skin In Vivo Optical Biopsy. *Electronics* **10**, 243. <https://www.mdpi.com/2079-9292/10/3/243> (2023) (Jan. 2021).
14. Ouyang, Y., Liu, Y., Wang, Z. M., Liu, Z. & Wu, M. FLIM as a Promising Tool for Cancer Diagnosis and Treatment Monitoring. *Nano-Micro Letters* **13**, 133. <https://doi.org/10.1007/s40820-021-00653-z> (2023) (June 2021).
15. Elson, D. S., Jo, J. A. & Marcu, L. Miniaturized side-viewing imaging probe for fluorescence lifetime imaging (FLIM): Validation with fluorescence dyes, tissue structural proteins and tissue specimens. *New Journal of Physics* **9**, 127. <https://www.ncbi.nlm.nih.gov/pmc/articles/PMC2691608/> (2023) (2007).
16. Paterson, A. S. *et al.* A low-cost smartphone-based platform for highly sensitive point-of-care testing with persistent luminescent phosphors. *Lab on a Chip* **17**, 1051–1059. <https://pubs.rsc.org/en/content/articlelanding/2017/lc/c6lc01167e> (2023) (Mar. 2017).

17. Davenport, M. L., Liu, S. & Bowers, J. E. Integrated heterogeneous silicon/III–V mode-locked lasers. *Photonics Research* **6**, 468–478. <https://opg.optica.org/prj/abstract.cfm?uri=prj-6-5-468> (2023) (May 2018).
18. Turgeman, L. & Fixler, D. Photon Efficiency Optimization in Time-Correlated Single Photon Counting Technique for Fluorescence Lifetime Imaging Systems. *IEEE Transactions on Biomedical Engineering* **60**, 1571–1579 (June 2013).
19. Lu, Z. G. *et al.* 312-fs pulse generation from a passive C-band InAs/InP quantum dot mode-locked laser. *Optics Express* **16**, 10835–10840. <https://opg.optica.org/oe/abstract.cfm?uri=oe-16-14-10835> (2023) (July 2008).
20. Valeur, B. & Berberan-Santos, M. N. in *Molecular fluorescence* 285–325 (John Wiley & Sons, Ltd, 2012). ISBN: 978-3-527-65000-2. <https://onlinelibrary.wiley.com/doi/abs/10.1002/9783527650002.ch10>.
21. MacLean, J.-P. W., Donohue, J. M. & Resch, K. J. Direct Characterization of Ultrafast Energy-Time Entangled Photon Pairs. *Physical Review Letters* **120**, 053601. <https://link.aps.org/doi/10.1103/PhysRevLett.120.053601> (2023) (Jan. 2018).
22. Scarcelli, G. & Yun, S. H. Entangled-photon coincidence fluorescence imaging. *Optics Express* **16**, 16189–16194. <https://www.osapublishing.org/oe/abstract.cfm?uri=oe-16-20-16189> (2019) (Sept. 2008).
23. Nasr, M. B. *et al.* Ultrabroadband Biphotons Generated via Chirped Quasi-Phase-Matched Optical Parametric Down-Conversion. *Physical Review Letters* **100**, 183601. <https://link.aps.org/doi/10.1103/PhysRevLett.100.183601> (2019) (May 2008).
24. Hendrych, M., Shi, X., Valencia, A. & Torres, J. P. Broadening the bandwidth of entangled photons: A step towards the generation of extremely short biphotons. *Physical Review A* **79**, 023817. <https://link.aps.org/doi/10.1103/PhysRevA.79.023817> (2019) (Feb. 2009).
25. Szoke, S., He, M., Hickam, B. P. & Cushing, S. K. Designing high-power, octave spanning entangled photon sources for quantum spectroscopy. *The Journal of Chemical Physics* **154**, 244201. <https://aip.scitation.org/doi/10.1063/5.0053688> (2021) (June 2021).
26. Menzel, E. R. & Popovic, Z. D. Picosecond-resolution fluorescence lifetime measuring system with a CW laser and a radio. *Review of Scientific Instruments* **49**, 39–44. <https://doi.org/10.1063/1.1135248> (2023) (Aug. 2008).

27. Zhao, J., Ma, C., Rüsing, M. & Mookherjea, S. High Quality Entangled Photon Pair Generation in Periodically Poled Thin-Film Lithium Niobate Waveguides. *Physical Review Letters* **124**, 163603. <https://link.aps.org/doi/10.1103/PhysRevLett.124.163603> (2023) (Apr. 2020).
28. Javid, U. A. *et al.* Ultrabroadband Entangled Photons on a Nanophotonic Chip. *Physical Review Letters* **127**, 183601. <https://link.aps.org/doi/10.1103/PhysRevLett.127.183601> (2022) (Oct. 2021).
29. Kumar, R., Ong, J. R., Savanier, M. & Mookherjea, S. Controlling the spectrum of photons generated on a silicon nanophotonic chip. *Nature Communications* **5**, 5489. <https://www.nature.com/articles/ncomms6489> (2023) (Nov. 2014).
30. Brumer, P. & Shapiro, M. Molecular response in one-photon absorption via natural thermal light vs. pulsed laser excitation. *Proceedings of the National Academy of Sciences* **109**, 19575–19578. <https://www.pnas.org/doi/10.1073/pnas.1211209109> (2023) (Nov. 2012).
31. Zavatta, A., Viciani, S. & Bellini, M. Single-photon excitation of a coherent state: Catching the elementary step of stimulated light emission. *Physical Review A* **72**, 023820. <https://link.aps.org/doi/10.1103/PhysRevA.72.023820> (2023) (Aug. 2005).
32. Freitag, M. *et al.* Dye-sensitized solar cells for efficient power generation under ambient lighting. *Nature Photonics* **11**, 372–378. <https://www.nature.com/articles/nphoton.2017.60> (2023) (June 2017).
33. Reich, N. H., van Sark, W. G. J. H. M. & Turkenburg, W. C. Charge yield potential of indoor-operated solar cells incorporated into Product Integrated Photovoltaic (PIPV). *Renewable Energy* **36**, 642–647. <https://www.sciencedirect.com/science/article/pii/S0960148110003423> (2023) (Feb. 2011).
34. Asban, S., Dorfman, K. E. & Mukamel, S. Interferometric spectroscopy with quantum light: Revealing out-of-time-ordering correlators. *The Journal of Chemical Physics* **154**, 210901. <https://doi.org/10.1063/5.0047776> (2023) (June 2021).
35. Oka, H. Real-time analysis of two-photon excitation by correlated photons: Pulse-width dependence of excitation efficiency. *Physical Review A* **81**, 053837. <https://link.aps.org/doi/10.1103/PhysRevA.81.053837> (2023) (May 2010).
36. Becker, W. *Advanced Time-Correlated Single Photon Counting Techniques* (eds Castleman, A. W., Toennies, J. & Zinth, W.) ISBN: 978-3-540-26047-9 978-3-540-28882-4. <http://link.springer.com/10.1007/3-540-28882-1> (2023) (Springer, Berlin, Heidelberg, 2005).

37. Berezin, M. Y., Lee, H., Akers, W. & Achilefu, S. Near Infrared Dyes as Lifetime Solvatochromic Probes for Micropolarity Measurements of Biological Systems. *Biophysical Journal* **93**, 2892–2899. <https://www.ncbi.nlm.nih.gov/pmc/articles/PMC1989699/> (2023) (Oct. 2007).
38. Dorfman, K. E., Schlawin, F. & Mukamel, S. Nonlinear optical signals and spectroscopy with quantum light. *Reviews of Modern Physics* **88**, 045008. <https://link.aps.org/doi/10.1103/RevModPhys.88.045008> (2018) (Dec. 2016).
39. Alander, J. T. *et al.* A review of indocyanine green fluorescent imaging in surgery. *Journal of Biomedical Imaging* **2012**, 7:7. <https://dl.acm.org/doi/10.1155/2012/940585> (2023) (Jan. 2012).
40. Reinhart, M. B., Huntington, C. R., Blair, L. J., Heniford, B. T. & Augenstein, V. A. Indocyanine Green: Historical Context, Current Applications, and Future Considerations. *Surgical Innovation* **23**, 166–175. <https://doi.org/10.1177/1553350615604053> (2023) (Apr. 2016).
41. Köllner, M. & Wolfrum, J. How many photons are necessary for fluorescence-lifetime measurements? *Chemical Physics Letters* **200**, 199–204. <https://www.sciencedirect.com/science/article/pii/000926149287068Z> (2023) (Nov. 1992).
42. Beer, M., Haase, J. F., Ruskowski, J. & Kokozinski, R. Background Light Rejection in SPAD-Based LiDAR Sensors by Adaptive Photon Coincidence Detection. *Sensors* **18**, 4338. <https://www.mdpi.com/1424-8220/18/12/4338> (2023) (Dec. 2018).
43. Shen, B., Bose, S. & Johnston, M. L. On-chip high-voltage SPAD bias generation using a dual-mode, closed-loop charge pump. *2017 IEEE International Symposium on Circuits and Systems (ISCAS)*, 1–4 (May 2017).
44. Tisa, S., Zappa, F. & Labanca, I. On-chip detection and counting of single-photons. *IEEE International Electron Devices Meeting, 2005. IEDM Technical Digest.*, 815–818 (Dec. 2005).
45. Maruyama, Y. & Charbon, E. An all-digital, time-gated 128X128 spad array for on-chip, filter-less fluorescence detection. *2011 16th International Solid-State Sensors, Actuators and Microsystems Conference*, 1180–1183 (June 2011).
46. Hickam, B. P., He, M., Harper, N., Szoke, S. & Cushing, S. K. Single-Photon Scattering Can Account for the Discrepancies among Entangled Two-Photon Measurement Techniques. *The Journal of Physical Chemistry Letters*, 4934–4940. <https://pubs.acs.org/doi/10.1021/acs.jpcllett.2c00865> (2022) (May 2022).
47. Grinvald, A. & Steinberg, I. Z. On the analysis of fluorescence decay kinetics by the method of least-squares. *Analytical Biochemistry* **59**, 583–598 (June 1974).

Chapter 6

CONCLUSIONS AND FUTURE DIRECTIONS

The preceding chapters include discussions of future research directions within the field of entangled photon spectroscopy. This chapter provides a brief review of a few intriguing possibilities within this growing field. Thanks to the efforts of members of the entangled photon subgroup of the Cushing lab, several of these research directions are entirely feasible in the near future.

In the context of entangled photon sources, several key developments would greatly advance and expand the field of entangled photon spectroscopy, including the use of entangled photons spanning other wavelength regimes and spectrometer miniaturization. Much of this work has depended on an entangled photon source produced via spontaneous parametric down conversion of a ~ 406 nm laser diode. With this configuration, the resultant entangled photon spectrum is centered at the “degenerate” wavelength, 812 nm. While the broadband entangled pairs span ~ 200 nm of bandwidth, experimental studies of the higher-energy atomic and molecular electronic states cannot be performed with this source. Higher energy entangled photon sources that are capable of optically addressing the electronic states in material systems thus represent a major milestone to expand the field of entangled photon spectroscopy. Several groups, including our own, have focused on achieving this goal, with some preliminary successes. Sub-shot-noise measurements of dye concentration have recently been performed using entangled photons spanning 400 nm to 650 nm produced by a 266 nm laser [1]. Further, experimental and theoretical work has demonstrated the possibility of entangled photon pairs at x-ray and extreme ultraviolet energies [2–5]. Other intriguing possibilities include developing highly non-degenerate entangled photon sources spanning frequency regimes, which could allow optical properties to be measured with widely-available detectors. For instance, non-degenerate entangled photon pairs have enabled IR optical coefficients to be measured with visible detectors [6].

The research described in this thesis has relied on a free-space entangled photon source. As alluded to throughout this work, entangled photons can be generated and manipulated in an entirely much smaller scales, including compact setups and on-chip platforms through the use of nanophotonic waveguides and integrated op-

tics. Compact entangled photon sources and detectors have been sent to space, highlighting their low-power and alignment-free capabilities [7, 8]. Combined with the ability of entangled photons to replicate classical laser signals, this characteristic could potentially represent a significant step in expanding the general availability of spectroscopy to broader populations. Handheld entangled photon spectrometers powered by batteries and operated by non-specialized users could potentially perform complex measurements and characterization.

Given the wide range of current spectroscopic techniques, there is ample opportunity to explore the ability of entangled photon pairs to enhance and replicate classical spectroscopic measurements. In the context of entangled two-photon interactions, experimental examinations of entangled two-photon interactions have exclusively focused on entangled two-photon absorption pathways. While these examinations have produced groundbreaking preliminary results, much knowledge about the nature of entangled two-photon light-matter interactions is still lacking. Chapter 4 highlights the debate surrounding the actual interaction cross section of the entangled two-photon absorption process. Other work has highlighted the role of an intermediate state during the entangled two-photon excitation [9–11]. To date, the experimental entangled photon spectroscopic work has focused exclusively on the two-photon absorption pathway. On the other hand, theoretical work has suggested that entangled photons are capable of enhancing and selecting stimulated Raman scattering pathways [12–15]. Given that two-photon absorption and stimulated Raman pathways are intimately intertwined, experimental studies of entangled photon stimulated Raman could elucidate underlying fundamental dynamics in the entangled light-matter interaction and provide a new means of optically controlling matter [16]. Furthermore, despite several theoretical examinations, pump-probe measurements with an entangled photon source have not yet been experimentally demonstrated. For these measurements, a broadband entangled photon source such as the one presented here is preferable due to the femtosecond correlation times that could allow atomic and molecular landscapes to be reconstructed.

Understanding entangled one-photon light-matter interactions also represents a significant thrust within entangled spectroscopy. Several spectroscopic techniques have been developed around the interaction of one entangled photon with a sample, as outlined in Chapter 4. An intriguing open question within the field revolves around the pathways in matter that are capable of preserving or destroying photon entanglement following a light-matter event. Previous work has indicated that photon

entanglement can survive even as the photons are converted to plasmons [17]. These results hint at new modalities of quantum computing with optical entangled photon sources or the improvement of quantum communication networks.

References

1. Matsuzaki, K. & Tahara, T. Superresolution concentration measurement realized by sub-shot-noise absorption spectroscopy. *Nature Communications* **13**, 953. <https://www.nature.com/articles/s41467-022-28617-w> (2023) (Feb. 2022).
2. Freund, I. & Levine, B. F. Parametric Conversion of X Rays. *Physical Review Letters*, 4 (1969).
3. Tamasaku, K. & Ishikawa, T. Interference between Compton Scattering and X-Ray Parametric Down-Conversion. *Physical Review Letters* **98**, 244801. <https://link.aps.org/doi/10.1103/PhysRevLett.98.244801> (2020) (June 2007).
4. Shwartz, S. & Harris, S. E. Polarization Entangled Photons at X-Ray Energies. *Physical Review Letters* **106**, 080501. <https://link.aps.org/doi/10.1103/PhysRevLett.106.080501> (2020) (Feb. 2011).
5. Shwartz, S. *et al.* X-Ray Parametric Down-Conversion in the Langevin Regime. *Physical Review Letters* **109**, 013602. <https://link.aps.org/doi/10.1103/PhysRevLett.109.013602> (2020) (July 2012).
6. Kalashnikov, D. A., Paterova, A. V., Kulik, S. P. & Krivitsky, L. A. Infrared spectroscopy with visible light. *Nature Photonics* **10**, 98–101. <https://www.nature.com/articles/nphoton.2015.252> (2018) (Feb. 2016).
7. Anwar, A., Perumangatt, C., Villar, A., Lohrmann, A. & Ling, A. Development of compact entangled photon-pair sources for satellites. *Applied Physics Letters* **121**, 220503. <https://aip.scitation.org/doi/full/10.1063/5.0109702> (2022) (Nov. 2022).
8. Tang, Z. *et al.* The photon pair source that survived a rocket explosion. *Scientific Reports* **6**, 25603. <https://www.nature.com/articles/srep25603> (2021) (May 2016).
9. Burdick, R. K. *et al.* Predicting and Controlling Entangled Two-Photon Absorption in Diatomic Molecules. *The Journal of Physical Chemistry A* **122**, 8198–8212. <https://doi.org/10.1021/acs.jpca.8b07466> (2018) (Oct. 2018).
10. Kang, G. *et al.* Efficient Modeling of Organic Chromophores for Entangled Two-Photon Absorption. *Journal of the American Chemical Society* **142**, 10446–10458. <https://doi.org/10.1021/jacs.0c02808> (2020) (June 2020).

11. Gu, B., Keefer, D. & Mukamel, S. Wave Packet Control and Simulation Protocol for Entangled Two-Photon Absorption of Molecules. *Journal of Chemical Theory and Computation* **18**, 406–414. <https://doi.org/10.1021/acs.jctc.1c00949> (2022) (Jan. 2022).
12. Munkhbaatar, P. & Myung-Whun, K. Selection of stimulated Raman scattering signal by entangled photons. *Optics Communications* **383**, 581–585. <http://www.sciencedirect.com/science/article/pii/S0030401816308586> (2019) (Jan. 2017).
13. Roslyak, O., Marx, C. A. & Mukamel, S. Nonlinear spectroscopy with entangled photons: Manipulating quantum pathways of matter. *Physical Review A* **79**, 033832. <https://link.aps.org/doi/10.1103/PhysRevA.79.033832> (2018) (Mar. 2009).
14. Svidzinsky, A. *et al.* Enhancing stimulated Raman excitation and two-photon absorption using entangled states of light. *Physical Review Research* **3**, 043029. <https://link.aps.org/doi/10.1103/PhysRevResearch.3.043029> (2023) (Oct. 2021).
15. Dorfman, K. E., Schlawin, F. & Mukamel, S. Stimulated Raman Spectroscopy with Entangled Light: Enhanced Resolution and Pathway Selection. *The Journal of Physical Chemistry Letters* **5**, 2843–2849. <https://doi.org/10.1021/jz501124a> (2019) (Aug. 2014).
16. Akbari, K., Di Giulio, V. & García de Abajo, F. J. Optical manipulation of matter waves. *Science Advances* **8**, eabq2659. <https://www.science.org/doi/10.1126/sciadv.abq2659> (2023) (Oct. 2022).
17. Fakonas, J. S., Mitskovets, A. & Atwater, H. A. Path entanglement of surface plasmons. *New Journal of Physics* **17**, 023002. <http://stacks.iop.org/1367-2630/17/i=2/a=023002> (2018) (2015).

Appendix A

SUPPLEMENTARY INFORMATION FOR DESIGNING HIGH-POWER, OCTAVE SPANNING ENTANGLED PHOTON SOURCES FOR QUANTUM SPECTROSCOPY

A.1 CLT refractive indices

The Sellmeier equations [1] describing the frequency and temperature dependent refractive indices of the material are plotted in Fig. A.1.

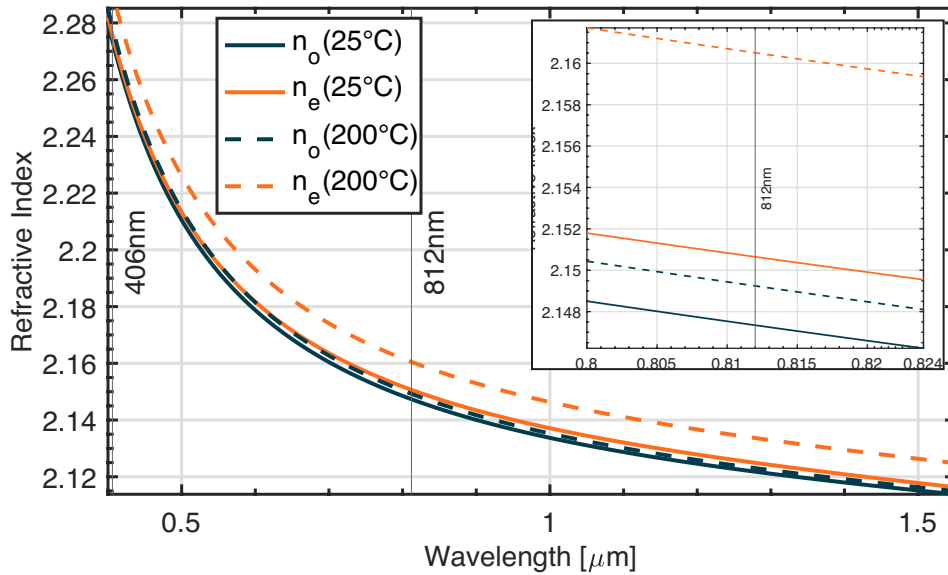


Figure A.1: Congruent lithium tantalate refractive indices for ordinary and extraordinary polarizations at two different temperatures.

A.2 Quasi-phase-matching

Based upon these values, the poling periodicity was calculated for a collinear 3rd-order Type-0 QPM configuration with a degenerate wavelength of 812nm.

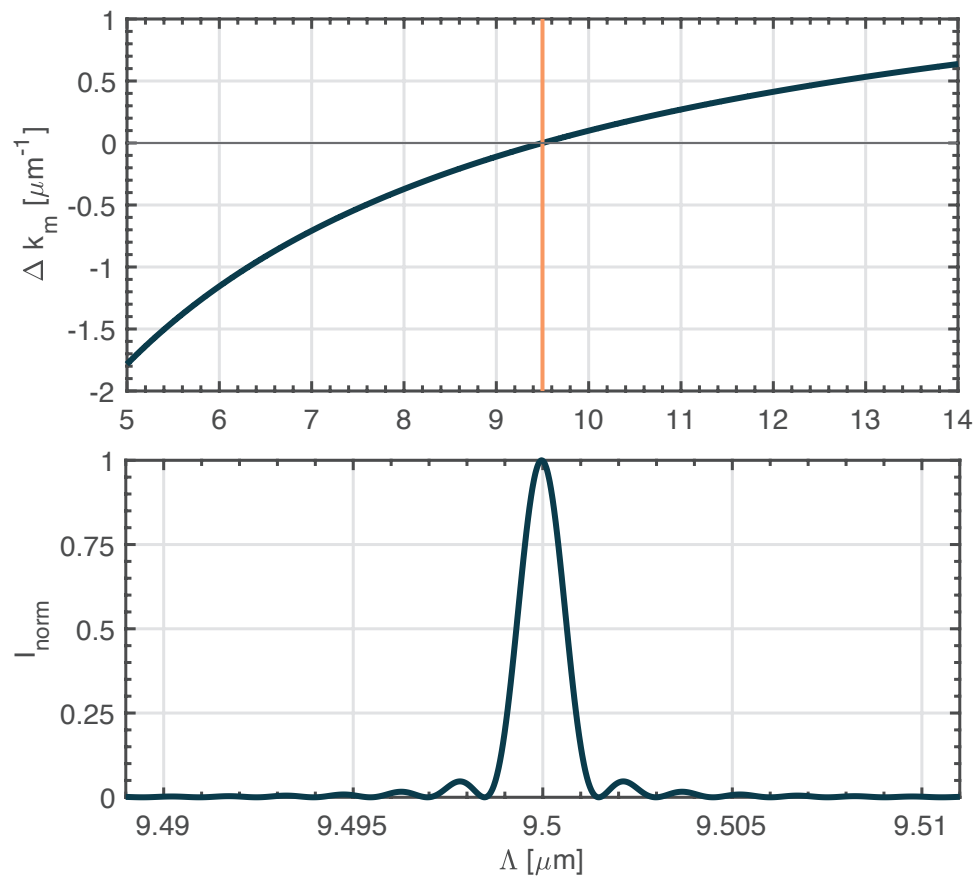


Figure A.2: Calculated poling period for 406nm-812nm at 133°C — CLT.

A.3 Phase-matching amplitude

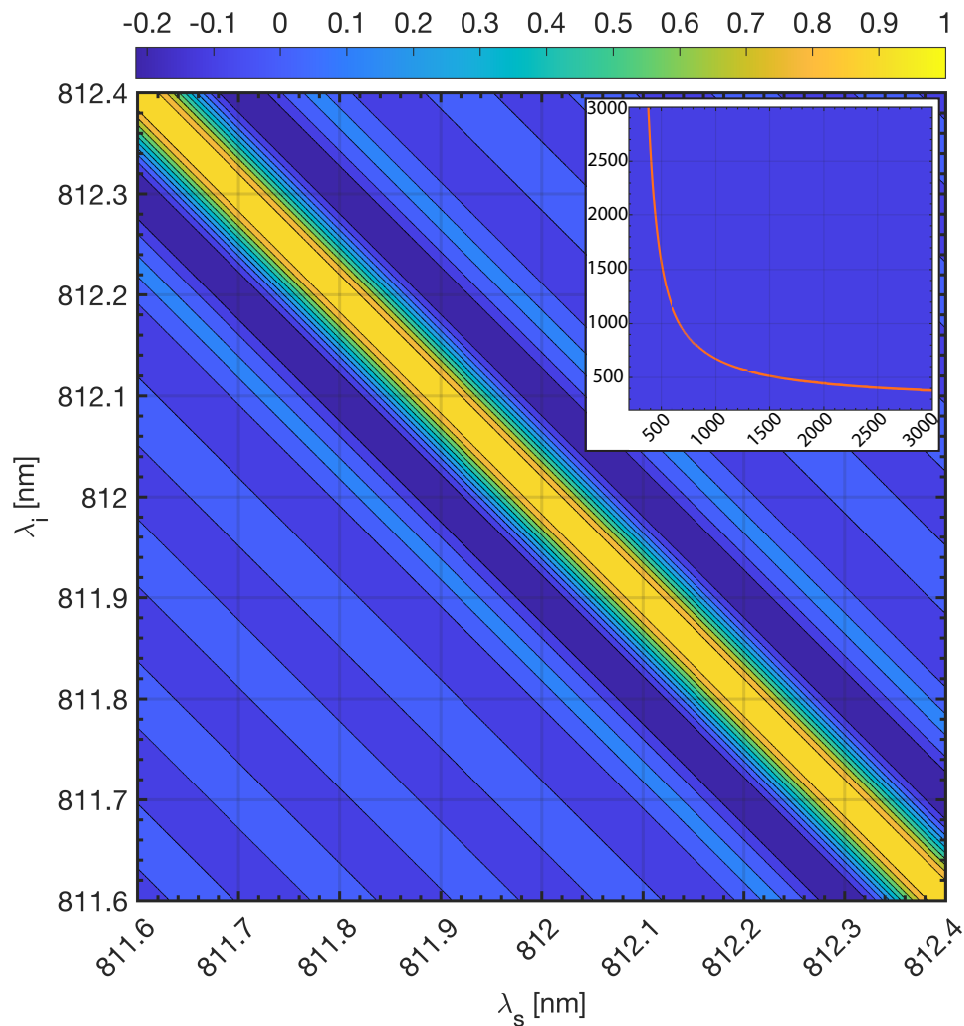


Figure A.3: Phase matching amplitude contour plot for a 20 mm long ppCLT grating with a $9.5 \mu\text{m}$ poling period at 133°C . The inset shows the wide range phase matching curve across a larger wavelength range for the Type-0 phase matching configuration.

Once the required poling period for our specific crystal and configuration has been determined, the two-dimensional phase-matching amplitude can be calculated by again evaluating Eq. 3.5 and Eq. 3.7 in the main text for a wide range of wavelength combinations. The result is the contour plot in Fig. A.3, which shows the downconversion intensity for photon pairs near the 812 nm degeneracy point. The inset of Fig. A.3 is a wide-range plot displaying the characteristic shape of the phase-matching curve for a Type-0 process. The contour provides some important

information regarding the resultant output of the SPDC process. Mathematically, the output state of the downconversion process can be described as:

$$|\Psi\rangle = \int \int \gamma(\omega_s, \omega_i) d\omega_s d\omega_i a_s^\dagger a_i^\dagger |0\rangle \quad (\text{A.1})$$

whereby the joint spectral amplitude (JSA), $\gamma(\omega_s, \omega_i)$ is the product of two terms, the pump-envelope function $\mu(\omega_s, \omega_i)$ and the phase-matching amplitude $\phi(\omega_s, \omega_i)$ [2]. Here the phase-matching amplitude function is solely determined by the crystal and the desired downconversion configuration. The pump-envelope function on the other hand is dictated by, as the name implies, the spectral characteristic of the pump beam. Obviously due to conservation of energy, μ will be diagonal in its orientation if plotted as a function of the signal and idler wavelengths.

The strongly diagonal direction of ϕ is advantageous as its overlap with the pump-envelope along the diagonal allows for a wide range of anti-correlated signal and idler photon pairs to be phase-matched. This is of particular importance in experiments where this anti-correlation is necessary for achieving two-photon absorption processes which occur via an intermediate energy level transition [3]. This can be viewed in contrast to applications where highly spectrally pure photon states are desired, such as in single photon sources. Here, obtaining a lack of frequency correlations by designing an anti-diagonal direction of ϕ is of primary concern.

A.4 Entanglement and purity

Given the output state as defined in Eq. A.1, the joint spectral amplitude allows for the prediction of the SPDC spectrum obtained for a given configuration of μ and ϕ by carrying out an integral across all signal/idler wavelengths with respect to a corresponding idler/signal wavelength held constant. For our specific 20 mm long ppCLT grating with a 9.5 μm poling period, the pump bandwidth has a distinct effect on not only the resulting emission spectrum's bandwidth, but also more profoundly on the entanglement of the photonic state. This is characterized by the purity,

$$P = \frac{1}{K} \quad (\text{A.2})$$

with

$$K = \frac{1}{\sum_i \lambda_i^2} \quad (\text{A.3})$$

being the Schmidt number equal to the rank of the reduced single particle density matrix. This value can be interpreted as a weighted measure (weights being the eigenvalues λ_i) of the number of modes required to represent the mixed state, and

therefore how entangled it is [4]. The eigenvalues themselves are obtained via a singular value decomposition of the joint spectral amplitude matrix. As shown in Fig. A.4 (top), the SPDC spectrum trivially narrows as the pump bandwidth is decreased up to a limiting point. Below this value, the intersection of the pump envelope μ with the phase matching amplitude ϕ no longer causes a decrease in the spectral width which is being carved out by μ . Fig. A.4 (bottom) shows the calculated FWHM of the SPDC spectrum as a function of the pump bandwidth, as well as the corresponding purity of the output state. As is evident, the purity of the state decreases with increasing pump bandwidths, and therefore conversely the entanglement of the overall state increases. While this is advantageous from the perspective of producing a state which displays more/stronger anti-correlations between photon pairs, the significant drawback is that the spectral resolution with which optical atomic and molecular transitions are able to be addressed is directly determined by the bandwidth of the pump laser driving the SPDC process. Thus, for highly spectrally resolved measurements, the figure of merit will be dictated by the pump laser.

A.5 Broadband HOM interference

The temporal properties and the degree of entanglement of the SPDC flux can be assessed by measuring the fourth-order interference in a two-photon Michelson (or Mach-Zehnder) interferometer. In such an interferometer, six beamsplitter ports are involved. See diagram below (Fig. A.5).

The interferometer input wavefunction for entangled pairs entering BS1 via port a is

$$|\Psi\rangle \propto \iint d\omega_s d\omega_i \psi(\omega_s, \omega_i) \hat{a}_s^\dagger(\omega_s) \hat{a}_i^\dagger(\omega_i) |0, 0\rangle \quad (\text{A.4})$$

where $\psi(\omega_s, \omega_i)$ is the joint spectral amplitude of the entangled photons as defined in previous sections.

After the first pass through BS1,

$$\hat{a}_s^\dagger(\omega_s) \hat{a}_i^\dagger(\omega_i) = \frac{1}{2} [\hat{c}_s^\dagger(\omega_s) \hat{c}_i^\dagger(\omega_i) - \hat{d}_s^\dagger(\omega_s) \hat{d}_i^\dagger(\omega_i) + i \hat{c}_s^\dagger(\omega_s) \hat{d}_i^\dagger(\omega_i) + i \hat{d}_s^\dagger(\omega_s) \hat{c}_i^\dagger(\omega_i)]. \quad (\text{A.5})$$

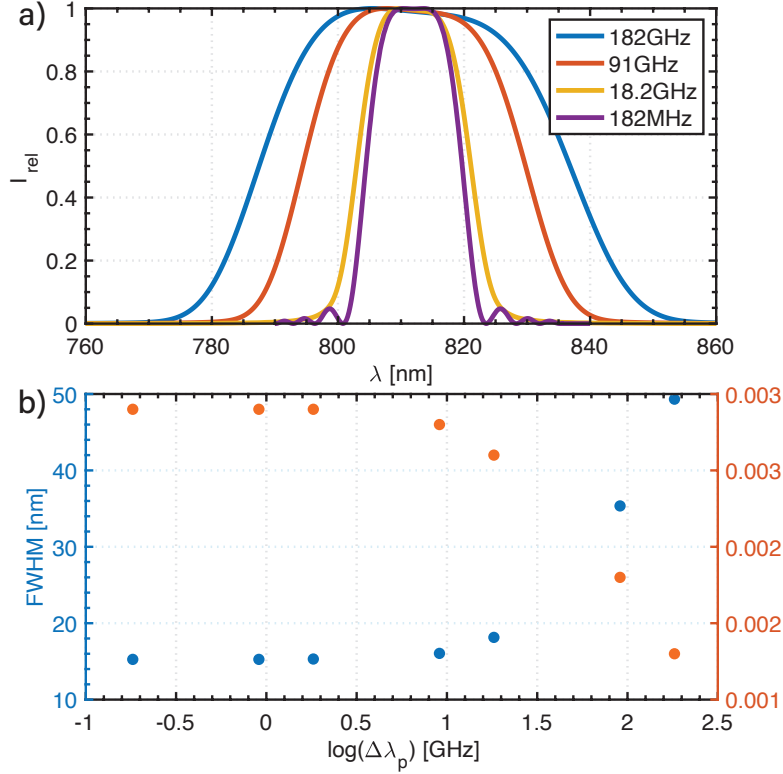


Figure A.4: SPDC emission spectrum as a function of the pump bandwidth. The corresponding broadening of the spectrum at larger bandwidths carries with it a degradation of the photon state purity which is of advantage where strong (anti-) correlation between photon pairs is desired.

After the second pass

$$\begin{aligned}
\hat{a}_s^\dagger(\omega_s)\hat{a}_i^\dagger(\omega_i) &= \frac{1}{4} [1 + e^{i\omega_p\tau} - e^{i\omega_i\tau} - e^{i\omega_s\tau}] \hat{e}_s^\dagger(\omega_s)\hat{e}_i^\dagger(\omega_i) \\
&+ \frac{i}{4} [1 - e^{i\omega_p\tau} + e^{i\omega_i\tau} - e^{i\omega_s\tau}] \hat{e}_s^\dagger(\omega_s)\hat{f}_i^\dagger(\omega_i) \\
&+ \frac{i}{4} [1 - e^{i\omega_p\tau} - e^{i\omega_i\tau} + e^{i\omega_s\tau}] \hat{f}_s^\dagger(\omega_s)\hat{e}_i^\dagger(\omega_i) \\
&- \frac{1}{4} [1 + e^{i\omega_p\tau} + e^{i\omega_i\tau} + e^{i\omega_s\tau}] \hat{f}_s^\dagger(\omega_s)\hat{f}_i^\dagger(\omega_i).
\end{aligned} \tag{A.6}$$

Since the coincidences are detected after port f , the last term of the above expression is relevant. Using the fact that $\omega_i = \omega_p - \omega_s$, the ff component of the entangled two photon wavefunction becomes

$$\begin{aligned}
|\Psi\rangle_{ff} &\propto -\frac{1}{4} \iint d\omega_s d\omega_i \psi(\omega_s, \omega_i) [1 + e^{i\omega_p\tau} (1 + e^{-i\omega_s\tau}) + e^{i\omega_s\tau}] \hat{f}_s^\dagger(\omega_s)\hat{f}_i^\dagger(\omega_i) |0, 0\rangle \\
&= -\sqrt{2} \int d\omega_s \psi(\omega_s, \omega_p - \omega_s) [1 + \cos((\omega_p - \omega_s)\tau)] [1 + \cos(\omega_s\tau)] |0, 2\rangle.
\end{aligned} \tag{A.7}$$

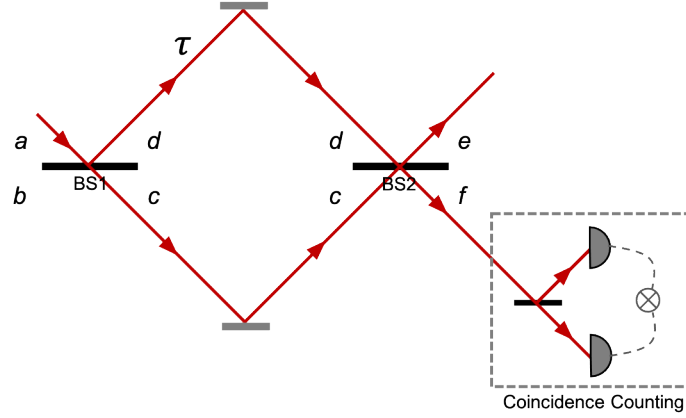


Figure A.5: Schematics of a two-photon Michelson or Mach-Zehnder interferometer.

Note that here it was assumed that ω_p is constant and the pump laser has an infinitely narrow line width. Therefore, the probability of detecting coincidences after port f is

$$P \propto 2 \int d\omega_s |\psi(\omega_s, \omega_p - \omega_s)|^2 [1 + \cos((\omega_p - \omega_s)\tau)]^2 [1 + \cos(\omega_s\tau)]^2 \quad (\text{A.8})$$

where $|\psi(\omega_s, \omega_p - \omega_s)|^2$ is the joint spectral density of the entangled photons. Thus the interference pattern at port f can be plotted out (Fig. A.6 and A.7). The interference pattern is the result of contributions from both classical and quantum (HOM) interferences. The effect of HOM is manifested by the main peak at zero time delay. As the bandwidth of the entangled photons change, either by varying phase matching conditions or simply placing a bandpass filter before the photon counting detectors, the width of the interference peak, proportional to the coherence length of the flux, changes accordingly.

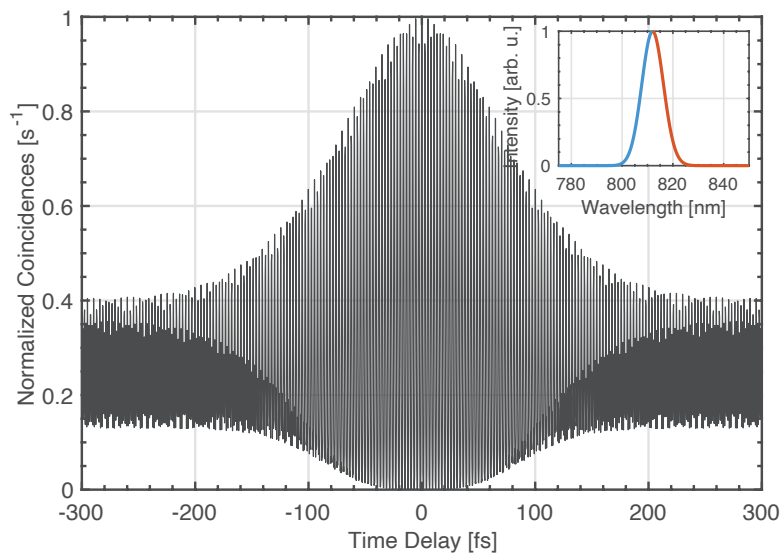


Figure A.6: Simulated normalized narrowband Michelson interference corresponding to the Gaussian SPDC spectrum filtered by 10 nm bandpass filter centered at 812 nm. Sampling step 0.32 fs.

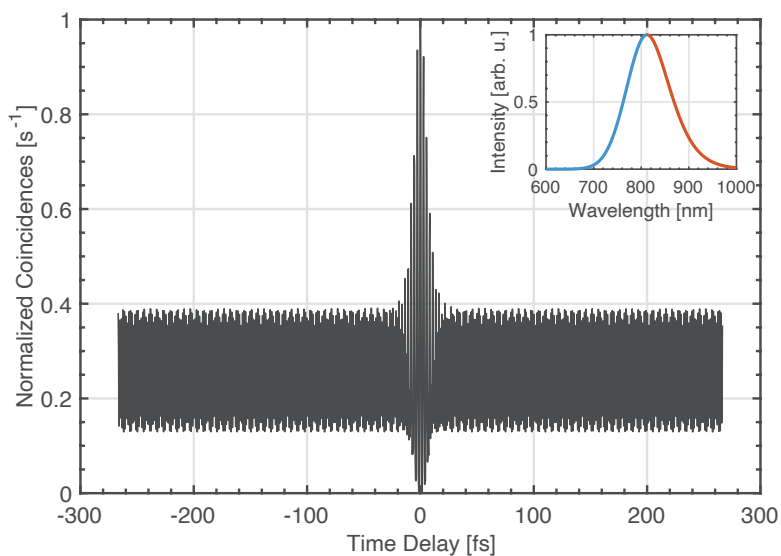


Figure A.7: Simulated normalized broadband Michelson interference corresponding to the Gaussian SPDC spectrum filtered by 125 nm bandpass filter centered at 812 nm. Sampling step 0.32 fs.

Additional experimental data

Figs. A.8, A.9, A.10, A.11 provide additional characterization on the relationship between interference measurements and the pump.

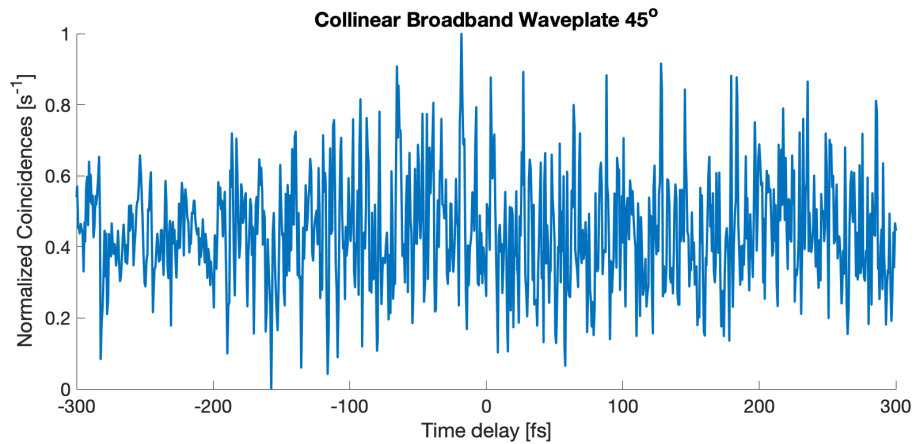


Figure A.8: Measured collinear broadband two-photon interference when the arms of the Michelson interferometer are perpendicularly polarized. No distinguishable interference pattern is observed, and the coincidences follow pump and noise fluctuations.

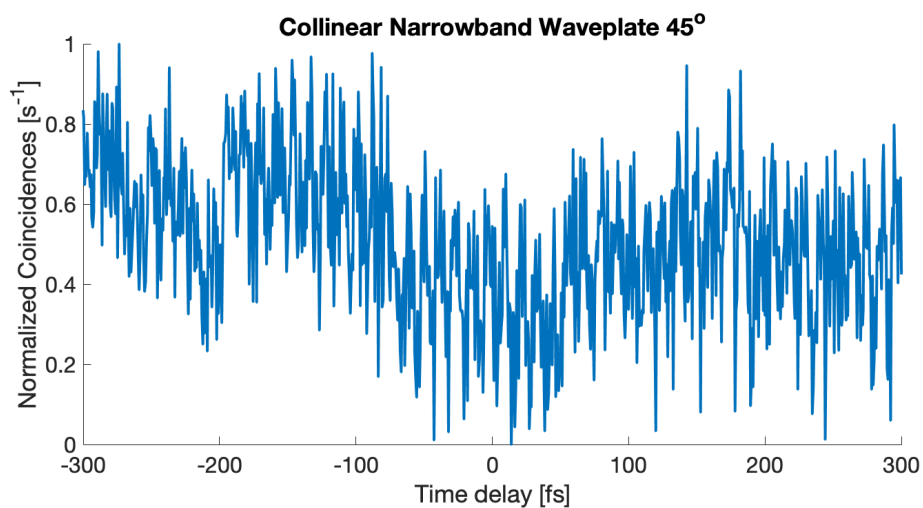


Figure A.9: Measured collinear narrowband two-photon interference when the arms of the Michelson interferometer are perpendicularly polarized. No distinguishable interference pattern is observed, and the coincidences follow pump and noise fluctuations.

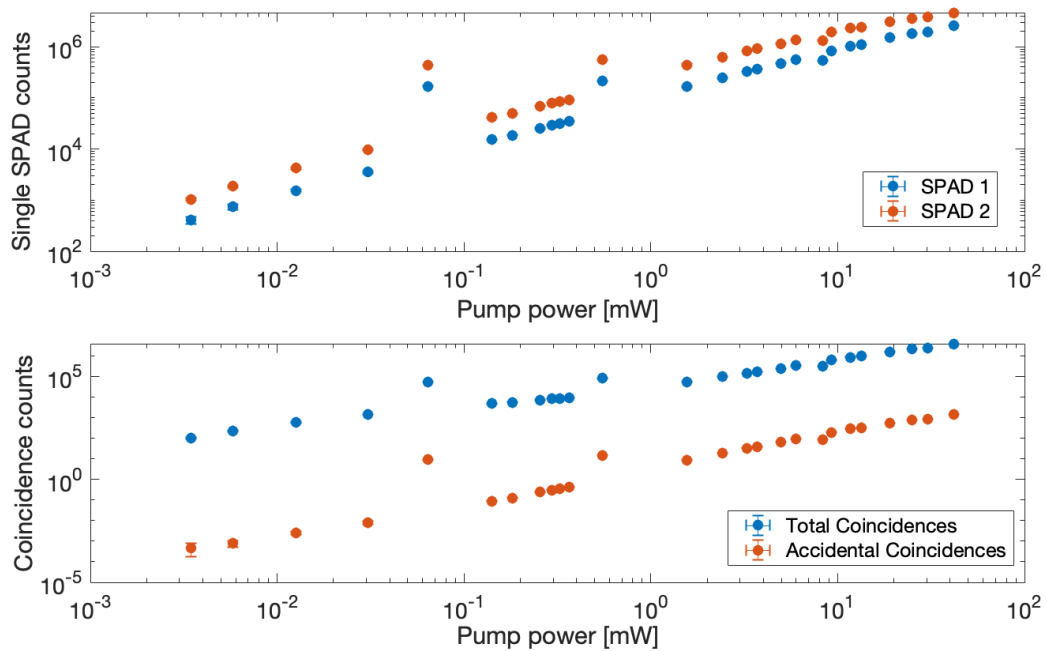


Figure A.10: Measured SPAD counts and coincidences vs. pump power in the collinear broadband case. Top: single SPAD channel counts in 15s. Bottom: total and accidental coincidences in 15s.

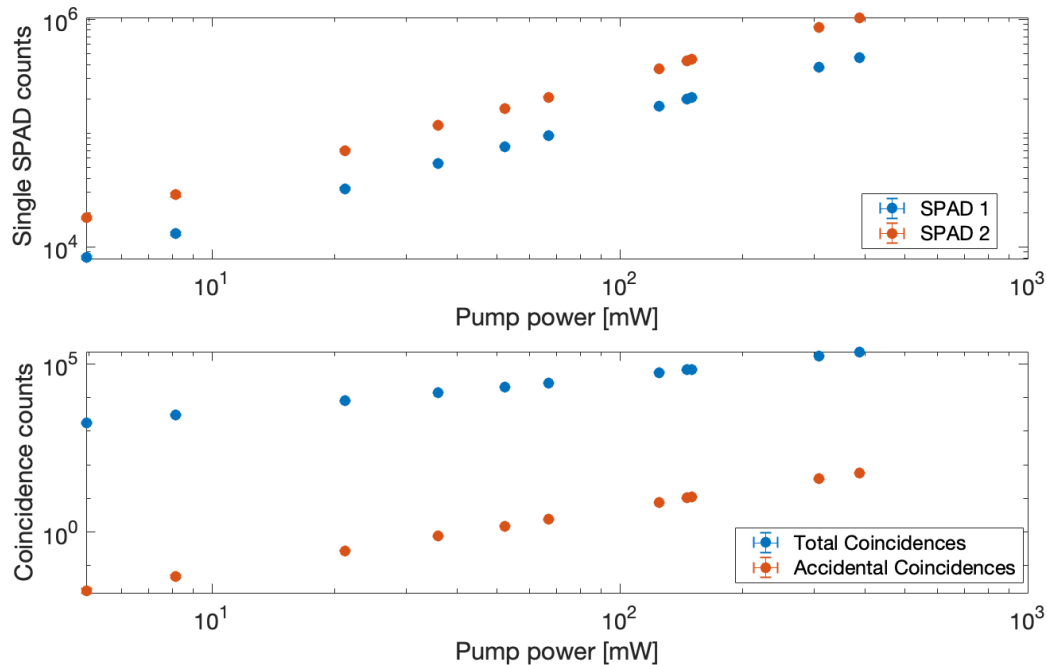


Figure A.11: Measured SPAD counts and coincidences vs. pump power in the collinear narrowband case. Top: single SPAD channel counts in 15s. Bottom: total and accidental coincidences in 15s.

References

1. Moutzouris, K., Hloupis, G., Stavrakas, I., Triantis, D. & Chou, M.-H. Temperature-dependent visible to near-infrared optical properties of 8 mol% Mg-doped lithium tantalate. *Optical Materials Express* **1**, 458–465. <https://www.osapublishing.org/ome/abstract.cfm?uri=ome-1-3-458> (2020) (July 2011).
2. Zielnicki, K. *et al.* Joint Spectral Characterization of Photon-Pair Sources. *Journal of Modern Optics* **65**, 1141–1160. <http://arxiv.org/abs/1801.01195> (2019) (June 2018).
3. Saleh, B. E. A., Jost, B. M., Fei, H.-B. & Teich, M. C. Entangled-Photon Virtual-State Spectroscopy. *Physical Review Letters* **80**, 3483–3486. <https://link.aps.org/doi/10.1103/PhysRevLett.80.3483> (2019) (Apr. 1998).
4. Ekert, A. & Knight, P. L. Entangled quantum systems and the Schmidt decomposition. *American Journal of Physics* **63**, 415–423. <https://doi.org/10.1119/1.17904> (2023) (May 1995).

Appendix B

SUPPLEMENTARY INFORMATION FOR SINGLE PHOTON
SCATTERING CAN ACCOUNT FOR THE DISCREPANCIES
BETWEEN ENTANGLED TWO-PHOTON MEASUREMENT
TECHNIQUES

B.1 Linear absorption measurement

In previous experimental protocols, the ETPA cross section was quantified by measuring the attenuation of entangled photon pairs transmitted through a molecular sample [1–7]. Here, we perform a similar study on a solution of 5 mM R6G in water by directly focusing the output of the ppLT chip into a sample cuvette and monitoring the transmitted photon counts with a spectrometer/EMICCD as the pump power is varied. The process is repeated for a blank water standard. The absorption cross section reported in Figure 4.5 is calculated from a plot of the transmitted photon rate vs. the input photon rate using the following steps:

$$A = \epsilon l c \quad (\text{B.1})$$

$$\epsilon = \frac{N_A}{\ln 10} \sigma \quad (\text{B.2})$$

$$T = \frac{I_{\text{sample}}}{I_{\text{solvent}}} = 10^{-A} \quad (\text{B.3})$$

$$\log_{10} \frac{I_{\text{sample}}}{I_{\text{solvent}}} = \log_{10} 10^{-A} = -A \quad (\text{B.4})$$

$$\log_{10} \frac{I_{\text{sample}}}{I_{\text{solvent}}} = \epsilon (1\text{cm})(5\text{mM}) \quad (\text{B.5})$$

$$\log_{10} \frac{I_{\text{sample}}}{I_{\text{solvent}}} = \frac{6.02 * 10^{23} \frac{\text{molecule}}{\text{mole}}}{\ln 10} * \sigma * (1\text{cm}) * \left(\frac{0.005\text{mole}}{1000\text{cm}^3} \right) \quad (\text{B.6})$$

$$\log_{10} \frac{I_{\text{sample}}}{I_{\text{solvent}}} = 2.8759 * 10^{19} \frac{\text{molecule}}{\text{cm}^2} * \sigma \quad (\text{B.7})$$

$$\sigma = -\frac{1}{2.8759 * 10^{19} \frac{\text{molecule}}{\text{cm}^2}} \log_{10} \frac{I_{\text{sample}}}{I_{\text{solvent}}} \quad (\text{B.8})$$

$$\sigma = -\frac{1}{2.8759 * 10^{19} \frac{\text{molecule}}{\text{cm}^2}} \log_{10} (0.9725) \quad (\text{B.9})$$

$$\sigma = 4 * 10^{-21} \frac{\text{cm}^2}{\text{molecule}}. \quad (\text{B.10})$$

In other experimental protocols, the sample with solvent counts are subtracted from the solvent counts to yield an absorbed photon rate, which is plotted against the input photon rate. The ETPA cross section is then calculated from the slope of the linear fit using the following equation:

$$\sigma_E = \frac{m}{lcN_A} \quad (\text{B.11})$$

where σ_E is the ETPA cross section, m is the slope of the linear fit, l is the path length of the cuvette, c is the sample concentration, and N_A is Avogadro's number. A cross section of $8(\pm 1) * 10^{-21} \text{ cm}^2/\text{molecule}$ was measured using this linear transmission method.

It is important to note that for an entangled photon pair, when performing coincidence counting, if one photon is lost then the entangled state is broken. In other words, the losses scale as the intensity squared because if one photon is lost neither of the two photons is measured by the coincidence detection. Squaring the measured scattering amplitude gives good agreement with the linear measurement, further confirming that for the measured virtual state molecules, any entangled enhancement is less than the scattering process. It should also be noted that a one photon scattering will lead to a linear slope just as the proposed linearization of the two-photon process.

B.2 Interferogram simulation

To simulate the interferograms shown in the right panel of Fig. B.2, the measured interferograms (left) are first Fourier transformed to reveal the different frequency components, shown below in Fig. B.1. The 1f peaks, which possess the same frequencies as the original interfering photons, are fitted with double or single Gaussian peaks (solid lines, Fig. B.1). For entangled two-photon Michelson cases (Fig. B.1a,b), the fitted peaks follow the distribution of entangled joint spectral amplitudes (JSA), and are then used as the input JSA for entangled fourth-order interference simulation (see section "Broadband fourth-order interference"). For example, for the single peaks, the JSA takes the form of

$$\phi(\lambda_s, \lambda_p) = \frac{1}{\sigma_{SPDC}\sqrt{2}} \exp\left\{-\frac{(\lambda_s - 2\lambda_p)^2}{2\sigma_{SPDC}^2}\right\} \quad (\text{B.12})$$

where λ_s is the wavelength of the signal, λ_p is the center wavelength of the pump, $\sigma_{SPDC} = \frac{FWHM}{2\sqrt{2\ln 2}}$ where $FWHM$ is the full width half maximum of the fitted peaks.

For the case of single-photon Michelson (Fig. B.1c), the fitted peak is a single Gaussian representing single-photon scatter, which is then used as the input spec-

trum for classical single-photon Michelson simulation. The resultant simulated interferograms are shown in Fig. B.2 right panel.

Fourier transform of measured interferograms

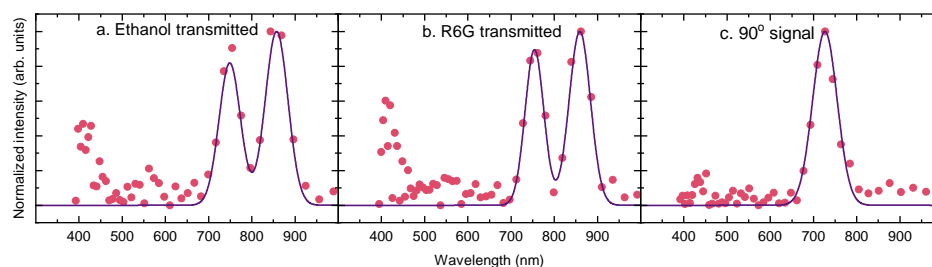


Figure B.1: Fourier transform of measured interferograms (pink scatter points) showing $1f$ and $2f$ components, which correspond to the interfering photon and the SPDC pump frequencies, respectively. Note that the $2f$ components in the left and middle panels are the result of interference between the pathways of unseparated entangled photon pairs, not single photons at the pump frequency. To obtain input spectra/JSA for interference simulation, the $1f$ components are fitted into Gaussian peaks (purple solid lines).

Comparison of experimental and simulated interferograms of transmitted coincidence

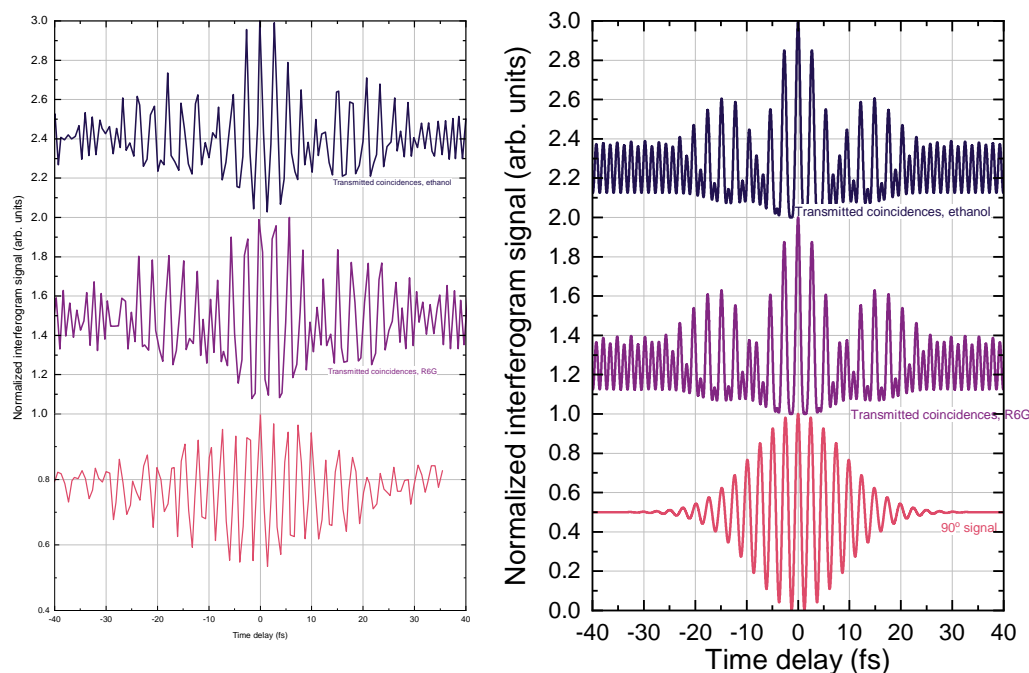


Figure B.2: Photon counts scaled to 1 vs time delay for non-degenerate bandwidth entangled photons traveling through a two-photon Michelson interferometer. Parameters from Gaussian fits of spectra obtained by Fourier-transforming the experimental interferograms (left) are used to simulate the two-photon Michelson interferograms (right). For more details on simulation method, see previous section “Interferogram simulation.” No modulation of the quantum state is observed when ethanol is replaced with an R6G/ethanol solution and the resulting 90-degree signal follows a one photon process.

B.3 Broadband fourth-order interference

Characterization of the temporal properties and visibility of the entangled state measured through the fourth-order interference with a two-photon Michelson interferometer. This setup has been previously theoretically modeled and experimentally verified [8, 9]. The two-photon Michelson interferometer consists of six beamsplitter ports, as shown in Fig. B.3.

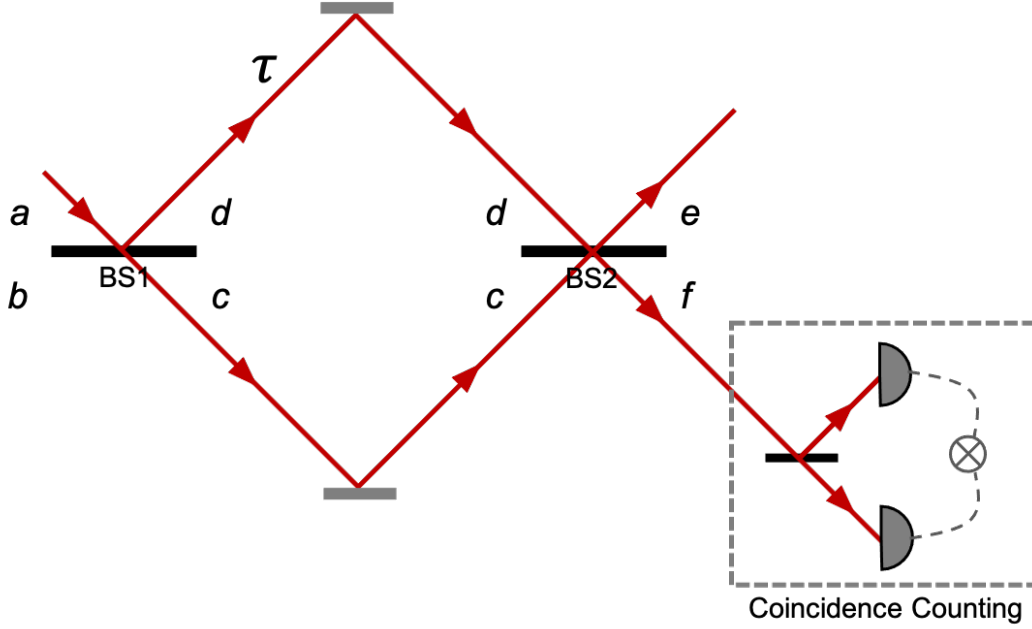


Figure B.3: Schematics of a two-photon Michelson or Mach-Zehnder interferometer.

The theoretical derivation of the interferogram we expect to observe is as follows:

Spontaneous parametric down conversion (SPDC) of a pump photon with frequency ω_p generates an entangled photon pair with signal and idler frequencies ω_s and ω_i , respectively, described by the wavefunction

$$|\Psi\rangle \propto \iint d\omega_s d\omega_i \phi(\omega_s, \omega_i) \hat{a}_s^\dagger(\omega_s) \hat{a}_i^\dagger(\omega_i) |0, 0\rangle \quad (\text{B.13})$$

where $\phi(\omega_s, \omega_i)$ is the joint spectral amplitude (JSA) of the entangled photons, and the vacuum component of $|\Psi\rangle$ is omitted. The JSA is normalized such that $\iint d\omega_s d\omega_i |\phi(\omega_s, \omega_i)|^2 = 1$, and is symmetrized such that $\phi(\omega_s, \omega_i) = \phi(\omega_i, \omega_s)$ because the signal and idler are indistinguishable in a type-0 SPDC source.

Upon first pass of BS1, the operators assume the form

$$\hat{a}_s^\dagger(\omega_s) \hat{a}_i^\dagger(\omega_i) \xrightarrow{\hat{U}_{BS1}} \frac{1}{2} [\hat{c}_s^\dagger(\omega_s) \hat{c}_i^\dagger(\omega_i) - \hat{d}_s^\dagger(\omega_s) \hat{d}_i^\dagger(\omega_i) + i\hat{c}_s^\dagger(\omega_s) \hat{d}_i^\dagger(\omega_i) + i\hat{d}_s^\dagger(\omega_s) \hat{c}_i^\dagger(\omega_i)] \quad (\text{B.14})$$

where it is assumed that the beam splitter has an equal transmittivity and reflectivity of 50% and no frequency dependence.

Following a time delay, τ , introduced in port d and a second pass through BS1, the operators transform as:

$$\begin{aligned}
\hat{a}_s^\dagger(\omega_s)\hat{a}_i^\dagger(\omega_i) \rightarrow & \frac{1}{4}[1 + e^{i\omega_p\tau} - e^{i\omega_i\tau} - e^{i\omega_s\tau}]\hat{e}_s^\dagger(\omega_s)\hat{e}_i^\dagger(\omega_i) \\
& + \frac{i}{4}[1 - e^{i\omega_p\tau} + e^{i\omega_i\tau} - e^{i\omega_s\tau}]\hat{e}_s^\dagger(\omega_s)\hat{f}_i^\dagger(\omega_i) \\
& + \frac{i}{4}[1 - e^{i\omega_p\tau} - e^{i\omega_i\tau} + e^{i\omega_s\tau}]\hat{f}_s^\dagger(\omega_s)\hat{e}_i^\dagger(\omega_i) \\
& - \frac{1}{4}[1 + e^{i\omega_p\tau} + e^{i\omega_i\tau} + e^{i\omega_s\tau}]\hat{f}_s^\dagger(\omega_s)\hat{f}_i^\dagger(\omega_i).
\end{aligned} \tag{B.15}$$

The rate of coincidence counts in port f , R_{ff} is obtained by projecting the wavefunction onto the response of two single-photon detectors with the projector P_{ff} . We assume that the photodetectors have a flat frequency response over the bandwidth of the SPDC, and that the integration time of the detectors is significantly longer than the coherence time of the pairs:

$$\begin{aligned}
R_{ff} \propto \langle \Psi | P_{ff} | \Psi \rangle & \approx \iint d\omega_1 d\omega_2 \langle \Psi | \hat{f}^\dagger(\omega_1)\hat{f}^\dagger(\omega_2) | 0 \rangle \langle 0 | \hat{f}^\dagger(\omega_1)\hat{f}^\dagger(\omega_2) | \Psi \rangle \\
& = \iint d\omega_1 d\omega_2 | \langle 0 | \hat{f}(\omega_1)\hat{f}(\omega_2) | \Psi \rangle |^2.
\end{aligned} \tag{B.16}$$

The effect of this projection operator is that only the component of $|\Psi\rangle$ with both photons in port f contributes to the observed coincidences. Inserting equations 2 and 4 yields a four-dimensional integral, which is then simplified using the identity $\langle 0 | \hat{f}(\omega_a)\hat{f}(\omega_b) | \Psi \rangle = \delta(\omega_a - \omega_b)$ to a two-dimensional integral:

$$R_{ff} \propto \iint d\omega_s d\omega_i | 1 + e^{i(\omega_s+\omega_i)\tau} + e^{i\omega_s\tau} + e^{i\omega_i\tau} |^2 |\phi(\omega_s, \omega_i)|^2. \tag{B.17}$$

To further simplify equation B.17, we approximate the JSA from our source as follows. Due to energy conservation, $\phi(\omega_s, \omega_i)$ will be proportional to the amplitude of the pump beam at the sum of the pair frequency, $\alpha(\omega_s + \omega_i)$, and will also be proportional to the phase-matching amplitude of the crystal, $\Phi(\omega_s, \omega_i)$, which is symmetric about $\omega_s = \omega_i$:

$$\phi(\omega_s, \omega_i) \propto \alpha(\omega_s + \omega_i)\Phi(\omega_s, \omega_i). \tag{B.18}$$

Due to the narrow bandwidth of the pump laser, we approximate the pump amplitude function as a delta function at $\lambda = 406$ nm. The joint spectral intensity (the square of the JSA) becomes

$$|\phi(\omega_s, \omega_i)|^2 = \delta(\omega_p - \omega_s - \omega_i)S(\omega_s) \quad (\text{B.19})$$

where $S(\omega_s)$ is the spectral density of the SPDC (the spectrum of the pairs as measured by a spectrometer) and is symmetric about $\omega_s = \omega_p/2$. Inserting equation B.19 into equation B.17 reduces the two-dimensional integral to a single-dimensional integral, which is then simplified further using standard trigonometric identities:

$$R_{ff} \propto \int d\omega_s |1 + e^{i(\omega_s + \omega_i)\tau} + e^{i\omega_s\tau} + e^{i(\omega_p - \omega_s)\tau}|^2 S(\omega_s) \quad (\text{B.20})$$

$$\propto \int d\omega_s [1 + \cos((\omega_p - \omega_s)\tau)][1 + \cos(\omega_s\tau)] S(\omega_s). \quad (\text{B.21})$$

The quality of the Michelson interferogram can be inferred from its visibility, calculated as

$$V = \frac{R_{\text{maximum}} - R_{\text{minimum}}}{R_{\text{maximum}} + R_{\text{minimum}}}. \quad (\text{B.22})$$

B.4 Entangled photon spectra

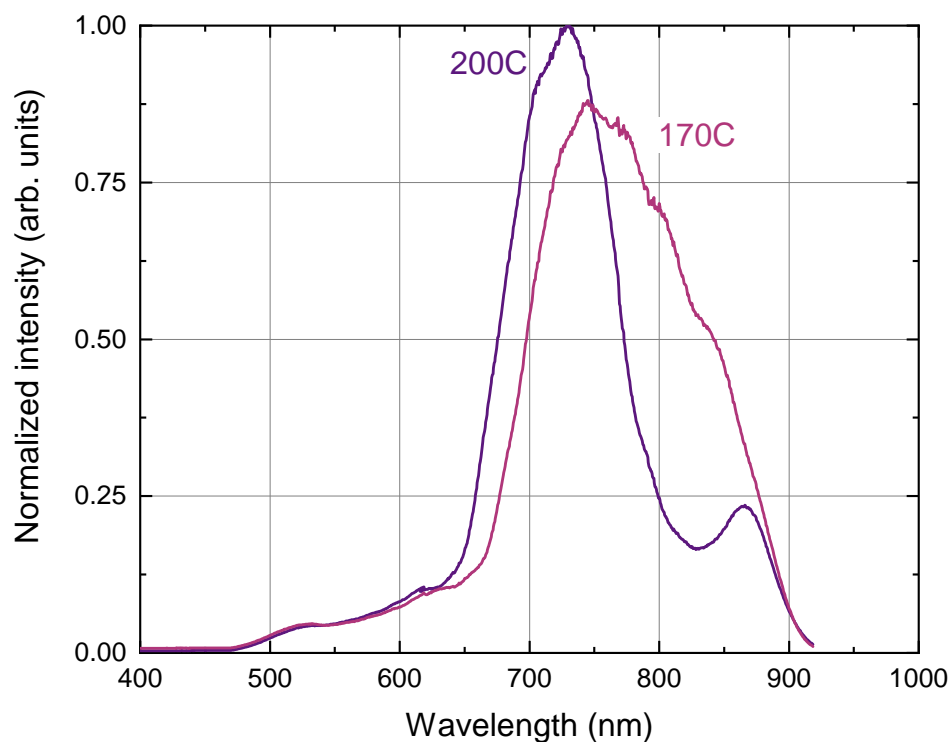


Figure B.4: Normalized spectra of the entangled photons for two ppLT crystal temperatures (changing the phase matching parameters). The 200°C entangled photons (purple trace) are described as the nondegenerate spectrum while the 170°C entangled photons (pink trace) are described as the degenerate spectrum. Note that the EMICCD has a quantum efficiency that tails to ~ 900 nm, giving the high wavelength cutoff slope seen for both spectra.

B.5 Absorption spectra of studied compounds

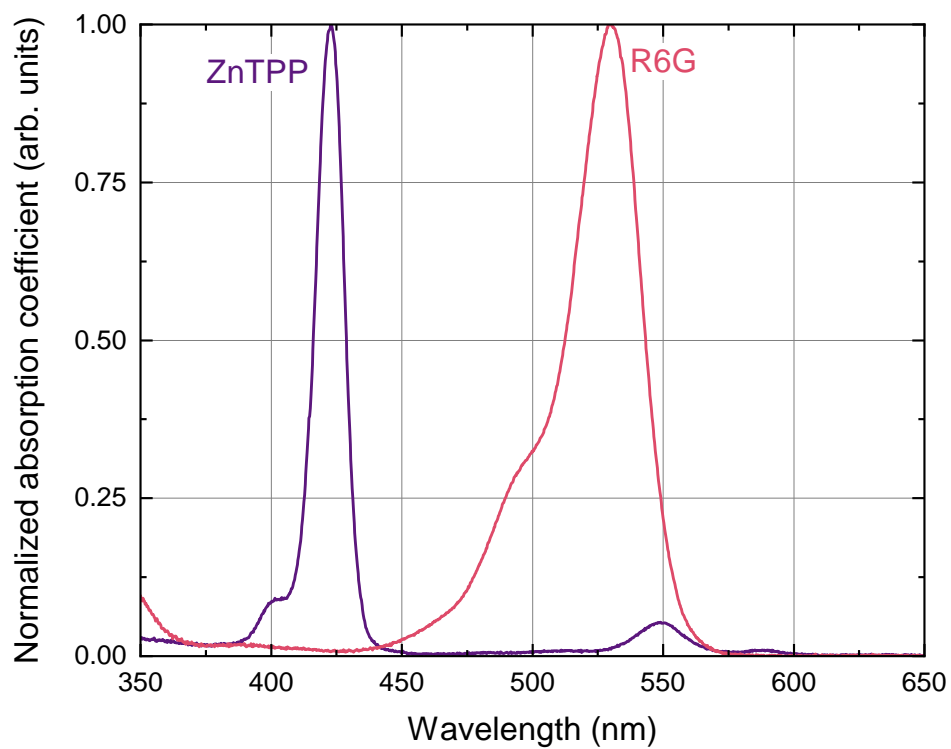


Figure B.5: Normalized absorption spectra of zinc tetraphenylporphyrin (ZnTPP, purple trace) and Rhodamine 6G (R6G, pink trace) [10].

B.6 Degenerate entangled photons

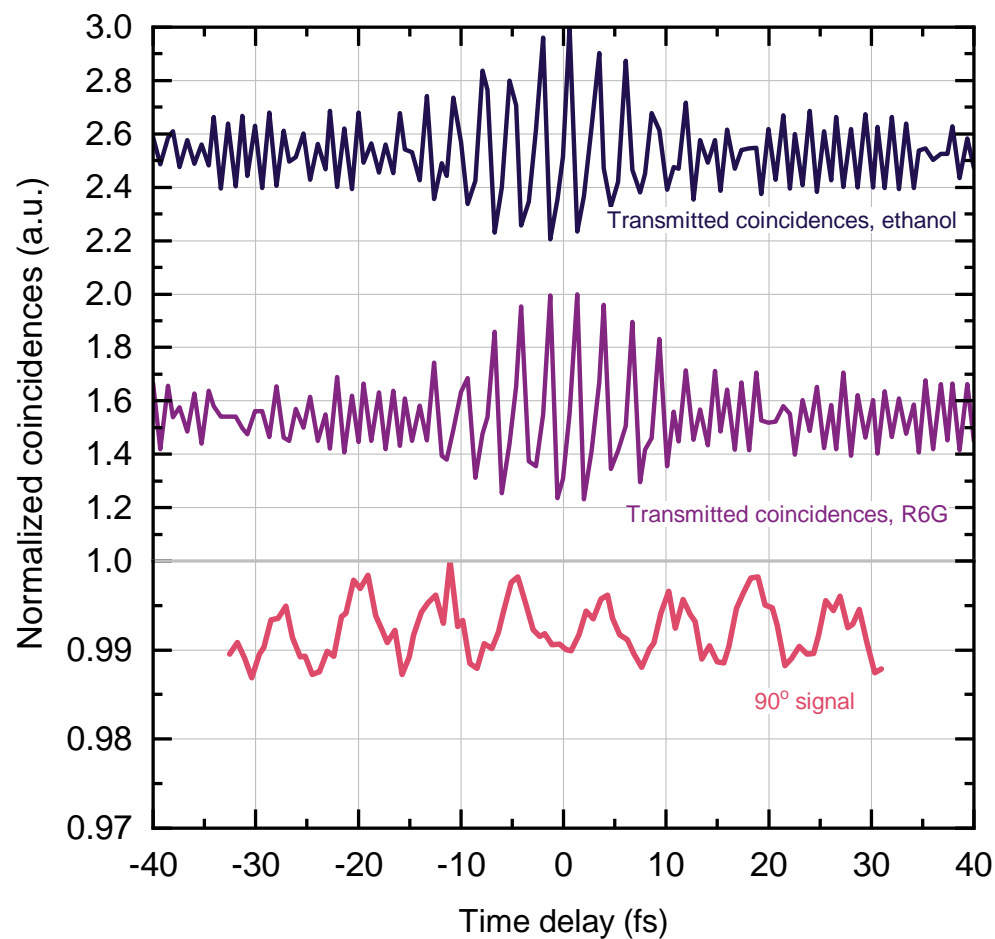


Figure B.6: Photon counts scaled to 1 vs time delay for degenerate bandwidth entangled photons traveling through a two-photon Michelson interferometer. The top trace is coincidence counts with solvent, the middle trace is transmitted coincidence counts with R6G, and the bottom trace is summed CCD counts of the 90-degree signal. Note that the scale of the y axis is shifted below values of 1 so that the bottom trace can be better visualized.

B.7 Zinc tetraphenylporphyrin

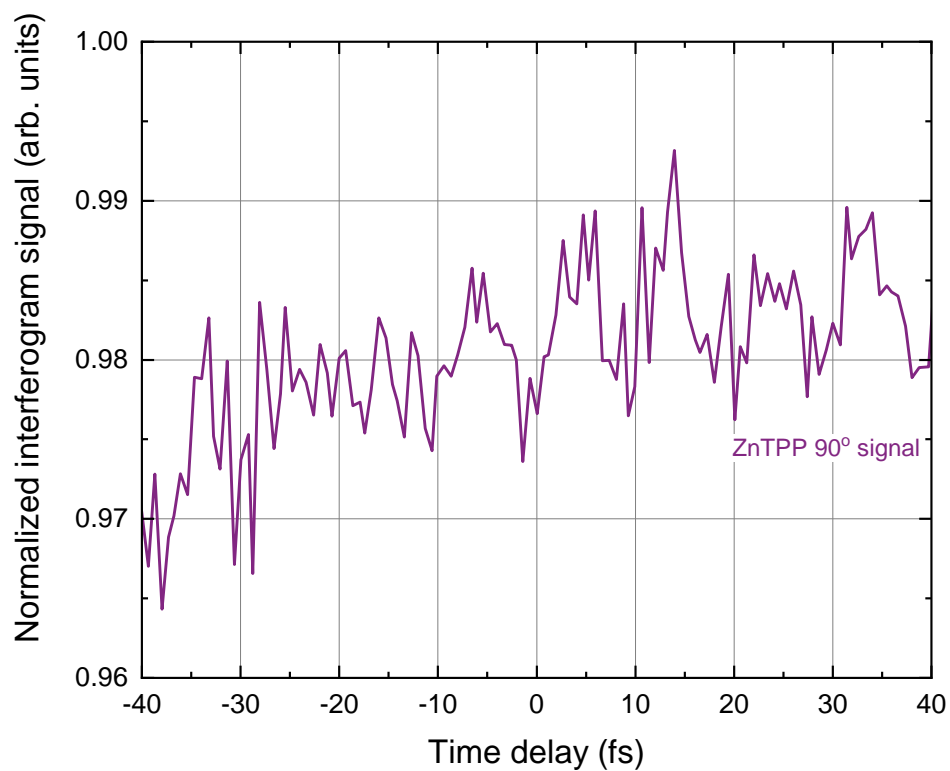


Figure B.7: Normalized 90-degree summed EMICCD counts versus time delay of broadband entangled photons focused into a solution of zinc tetraphenylporphyrin (ZnTPP). The signal here is purely a result of the noise of the EMICCD camera.

B.8 Destruction of entanglement with a quarter-wave plate

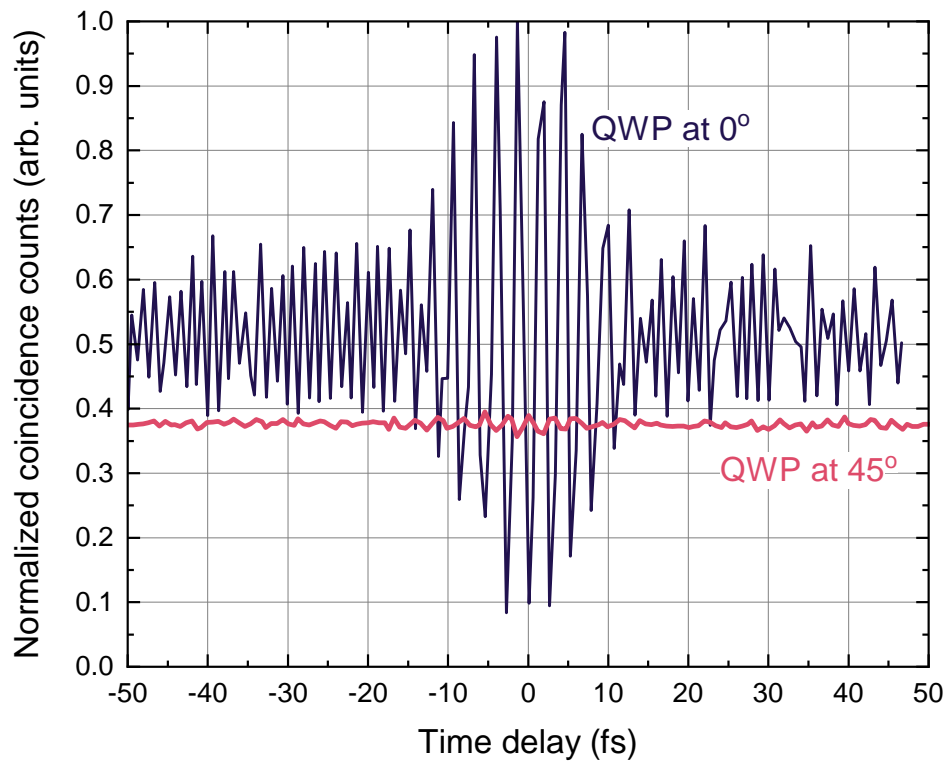


Figure B.8: Normalized coincidences when the quarter-wave plate (QWP) in one of the arms of the two-photon Michelson interferometer is adjusted from 0° (purple line) to 45° (pink line) to polarize the entangled photons 90° with respect to each other. The baseline of the resulting interferogram (pink line) has been corrected with a multiplication factor to account for the deviation from the ideal 50 : 50 beam splitter ratio as the polarization state is varied. This non-ideal ratio also contributes to the low visibility (< 0.04) oscillations around time zero.

B.9 Absorbed photon rate vs. input photon rate

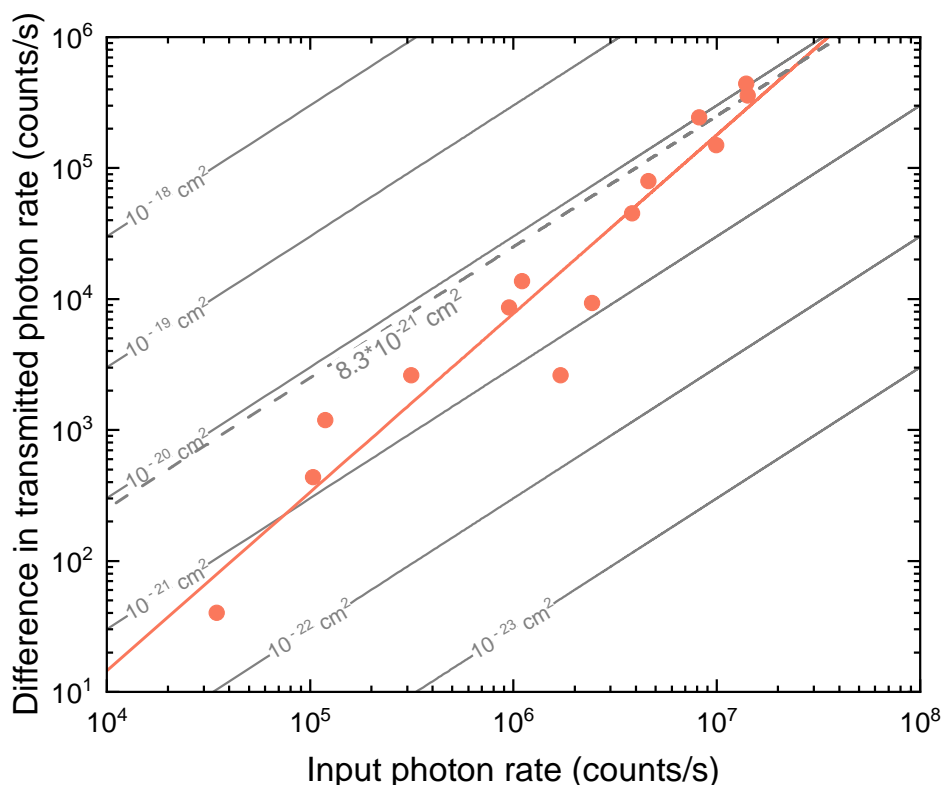


Figure B.9: Measured absorbed photon rate (orange data points, calculated from: $R_{\text{solvent}} - R_{\text{sample}}$, a popular method used literature) and fit (orange solid line) vs input photon rate for 5 mM Rhodamine 6G in water. The slope of the line of best fit for this data is 1.3. Using the method standard in literature, the ETPA cross section from the measured absorption rate would be $8(\pm 1) * 10^{-21} \text{ cm}^2/\text{molecule}$. In this manuscript, the linear relationship is determined to not be from ETPA, but rather from a single photon scattering process. Note that the error bars for each data point are on the order of the graph point size.

References

1. Lee, D.-I. & Goodson, T. Entangled Photon Absorption in an Organic Porphyrin Dendrimer. *The Journal of Physical Chemistry B* **110**, 25582–25585. <https://doi.org/10.1021/jp066767g> (2018) (Dec. 2006).
2. Harpham, M. R., Süzer, Ö., Ma, C.-Q., Bäuerle, P. & Goodson, T. Thiophene Dendrimers as Entangled Photon Sensor Materials. *Journal of the American Chemical Society* **131**, 973–979. <https://doi.org/10.1021/ja803268s> (2019) (Jan. 2009).

3. Guzman, A. R., Harpham, M. R., Süzer, Ö., Haley, M. M. & Goodson, T. G. Spatial Control of Entangled Two-Photon Absorption with Organic Chromophores. *Journal of the American Chemical Society* **132**, 7840–7841. <https://doi.org/10.1021/ja1016816> (2019) (June 2010).
4. Upton, L. *et al.* Optically Excited Entangled States in Organic Molecules Illuminate the Dark. *The Journal of Physical Chemistry Letters* **4**, 2046–2052. <https://pubs.acs.org/doi/10.1021/jz400851d> (2020) (June 2013).
5. Villabona-Monsalve, J. P., Calderón-Losada, O., Nuñez Portela, M. & Valencia, A. Entangled Two Photon Absorption Cross Section on the 808 nm Region for the Common Dyes Zinc Tetraphenylporphyrin and Rhodamine B. *The Journal of Physical Chemistry A* **121**, 7869–7875. <https://doi.org/10.1021/acs.jpca.7b06450> (2018) (Oct. 2017).
6. Villabona-Monsalve, J. P., Varnavski, O., Palfey, B. A. & Goodson, T. Two-Photon Excitation of Flavins and Flavoproteins with Classical and Quantum Light. *Journal of the American Chemical Society* **140**, 14562–14566. <https://doi.org/10.1021/jacs.8b08515> (2018) (Nov. 2018).
7. Villabona-Monsalve, J. P., Burdick, R. K. & Goodson, T. Measurements of Entangled Two-Photon Absorption in Organic Molecules with CW-Pumped Type-I Spontaneous Parametric Down-Conversion. *The Journal of Physical Chemistry C*, [acs.jpcc.0c08678](https://pubs.acs.org/doi/10.1021/acs.jpcc.0c08678). <https://pubs.acs.org/doi/10.1021/acs.jpcc.0c08678> (2020) (Oct. 2020).
8. Lopez-Mago, D. & Novotny, L. Coherence measurements with the two-photon Michelson interferometer. *Physical Review A* **86**, 023820. <https://link.aps.org/doi/10.1103/PhysRevA.86.023820> (2020) (Aug. 2012).
9. Lavoie, J. *et al.* Phase-Modulated Interferometry, Spectroscopy, and Refractometry using Entangled Photon Pairs. *Advanced Quantum Technologies* **3**, 1900114. <https://onlinelibrary.wiley.com/doi/abs/10.1002/qute.201900114> (2022) (2020).
10. Taniguchi, M. & Lindsey, J. S. Database of Absorption and Fluorescence Spectra of >300 Common Compounds for use in PhotochemCAD. *Photochemistry and Photobiology* **94**, 290–327. <https://onlinelibrary.wiley.com/doi/abs/10.1111/php.12860> (2022) (2018).

Appendix C

SUPPLEMENTARY INFORMATION FOR ENTANGLED
PHOTON CORRELATIONS ALLOW A CONTINUOUS-WAVE
LASER DIODE TO MEASURE SINGLE PHOTON,
TIME-RESOLVED FLUORESCENCE

C.1 Select optical properties of ICG

Solvent	Peak absorption/emission wavelength (nm)	$\epsilon \text{ cm}^{-1} \text{ mol}^{-1}$ at λ_{max}	Φ
Methanol	784/809	221,000	0.09
Ethanol	787/811	167,000	0.11
DMSO	794/817	170,000	0.12

Table C.1: Select optical properties of ICG in methanol, ethanol, and DMSO from Ref. [1].

C.2 Confirmation of fluorescence

While the results presented in the main text of the chapter suggest that the coincidences observed with the sample present originate from fluorescence due to the good agreement between the observed histograms and fits, a control experiment as additional evidence was performed to rule out the role of scatter from the excitation beam. Additionally, a blank scan was performed, where the dye solution was replaced with only methanol. Figure C.1 displays this histogram, as well as a side-by-side comparison of the histograms observed with and without the dye. The lack of an obvious coincidence peak suggests that the SPDC flux is sufficiently filtered from the fluorescence detector, and that the coincidences observed in the experiment originated from fluorescence of the sample.

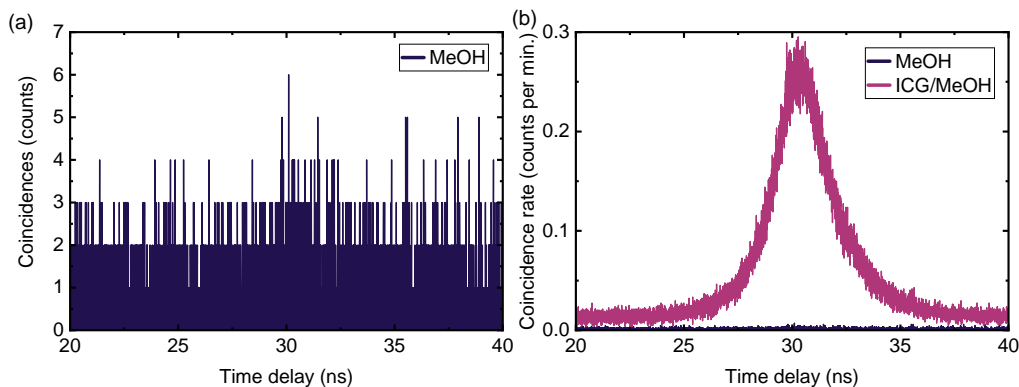


Figure C.1: Coincidence histograms of pure methanol and methanol/indocyanine solutions. (a) Coincidence histogram from methanol blank experiment. (b) Coincidence rates for blank methanol and ICG/methanol solutions.

C.3 Experimental stability and background

Over the course of the 14-16 hour scans presented in Fig. 5.3, minimal drift or sample degradation were observed. Figure C.2 shows the singles and coincidence count rates over the course of the experiment. Coincidence count rates were obtained by summing all coincidence counts between 24 and 34 nanoseconds and subtracting the product of accidentals per bin and the number of bins in this window. The accidental rate per bin was obtained by averaging the number of coincidences observed from 50 to 70 ns, far from the coincidence peak. While a slight decrease in the heralding channel (Channel 0) is observed in the DMSO data over time likely due to drift in the alignment, this change in intensity is about 1% of the original value. The singles rate in the fluorescence arm (Channel 1) as well as the coincidence rate appear to remain steady over time. While ICG is known to exhibit degradation over time due to a number of factors, we do not observe a loss in coincidence counts likely because the sample is exposed to low light levels, and the sealed cuvette containing the dye had minimal headspace. The observed fluctuations in the coincidence data is not due to technical noise, but rather the Poissonian statistics of a shot-noise limited system, as the variance of the observed rates is nearly equivalent to the mean of the rate (Table C.2).

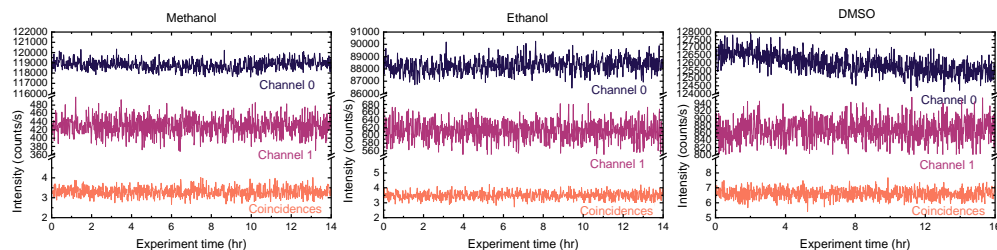


Figure C.2: Count rates in Channel 0 (reference photons), Channel 1 (fluorescence photons), and coincidences from $100\mu\text{M}$ ICG in methanol, ethanol, and DMSO experiment over the course of the scan.

Parameter	Mean rate (counts per second)	Rate variance (counts/second) ²
Heralding singles	12600	39300
Fluorescent singles	870	880
Raw coincidences	8.3	8.0
Accidental coincidences	0.78	0.77
True coincidences	7.5	8.7

Table C.2: Count rate means and variances demonstrating nearly shot-noise limited statistics.

The background of the experiments presented here are low, but some stray light is likely still present. From the blank experiment, the singles rate at the fluorescence detector was 28 ± 5 counts per second, slightly higher than the specified dark count rate of the detectors at 10 counts per second. Regardless, the fluorescence counts observed during experiments with dye are substantially higher, suggesting that these counts are mostly fluorescence and not background.

C.4 Lifetime fits with residuals

Fits of the raw histograms are shown in Fig. C.3 on a logarithmic scale to show the accuracy of the fit extending to the tails of the coincidence peaks over several decades of intensity.

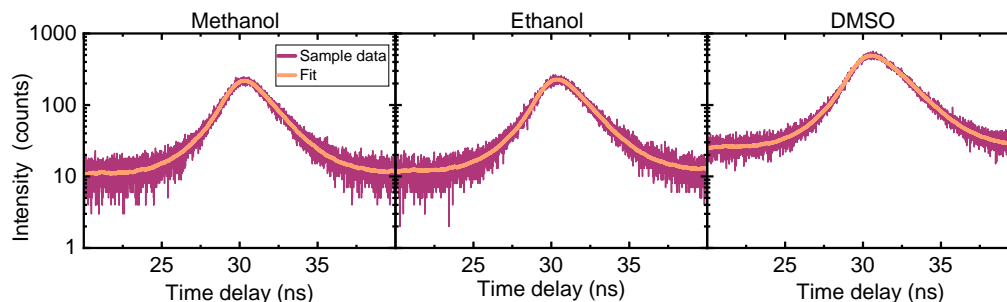


Figure C.3: Raw coincidence data and fits for ICG in methanol (left), ethanol (center), and DMSO (right) on a logarithmic scale.

The weighted residuals are shown in Fig. C.4, the lack of obvious trends in the data suggest that the model used for fitting the data is reasonable. Here, the residuals are weighted by the inverse square of the fit value at each timepoint, as the uncertainty of the counts is proportional to this value for Poissonian data.

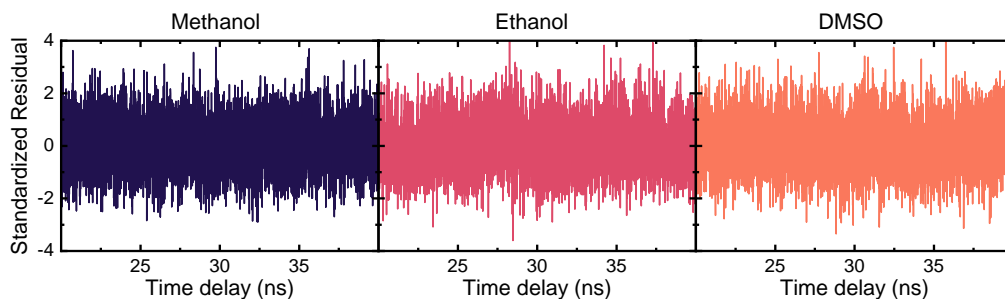


Figure C.4: Weighted residuals of the fits from Fig. C.3.

C.5 Fitting algorithm

The fits presented in this work were performed in a custom Matlab program using the iterative reconvolution technique. First, the accidentals present in the IRF, as obtained by averaging the histogram coincidence counts from 50-70 ns, were subtracted from the raw data, and the data were truncated to a 20-40 ns window to reduce the amount of baseline present in the fit. The resulting true coincidence curve was then scaled so that the sum of counts over the IRF was unity. The experimental data from each sample were also truncated to a 20-40 ns window. The accidental counts were not subtracted from the sample coincidence curve, as these were treated

as a fit parameter. The accidental data was also normalized so that the sum of counts was equal to unity. The sample response model functions were of the form:

$$R(t_i) = c(e^{-t_i/\tau} + A) \quad (\text{C.1})$$

where τ , the fluorescence lifetime, and A , a factor accounting for accidentals, are the fit parameters. The constant c is used to normalize the area of the sample response to unity. The normalization in all three cases is necessary because the convolved response of two functions has an area equal to the product of the areas of the original functions. The experiment response function was calculated as a discrete convolution of the sample response and the IRF, truncated to the length of the experimental data, and normalized to an area of one. Then, a trust-region nonlinear regression algorithm was performed to estimate the parameters τ and A that minimize the sum of squared errors between the experimental data and the fit.

References

1. Berezin, M. Y., Lee, H., Akers, W. & Achilefu, S. Near Infrared Dyes as Lifetime Solvatochromic Probes for Micropolarity Measurements of Biological Systems. *Biophysical Journal* **93**, 2892–2899. <https://www.ncbi.nlm.nih.gov/pmc/articles/PMC1989699/> (2023) (Oct. 2007).

*Appendix D***ENTANGLED TWO-PHOTON MICHELSON
INTERFEROMETER ALIGNMENT GUIDE**

The purpose of this guide is to provide a step-by-step alignment procedure for an entangled two-photon Michelson interferometer using a ppLT chip and 401 nm OBIS alignment diode found in the Cushing lab. The wavelengths that are referred to throughout this guide correspond to this particular setup, but the general procedure should apply to other experimental setups, such as those in the visible/UV regions. The following alignment procedure roughly follows this procedure. It is helpful to read this procedure before beginning the alignment guide.

As of the writing of this guide, the output of the OBIS is passed through a series of beam conditioning optics that enable precise control of several key parameters. A variable ND wheel is placed immediately following the OBIS output such that the optical power of the OBIS can be precisely tuned. This control is helpful in the context of the alignment procedure because maximum pump power is required for the beam camera to measure the SPDC, but the pump power can be dimmed for steps involving alignment with the pump. Note that the optical power can also be changed using the Coherent control software, but this also shifts the emission wavelength slightly, which can affect the SPDC emission. Following this ND wheel, a polarizing beam splitter is utilized to ensure that the pump beam has one polarization and then a half-wave plate is utilized to rotate its polarization before coupling into the ppLT chip.

Before following this procedure, first ensure that the pump beam is straight along a reference line and that the ppLT chip is straight along the same reference line. For this step, is it helpful to have 2 irises positioned before and after the chip along a row of reference holes such that a 2 mirror alignment can be performed. Alternatively, both irises can be placed before the chip. Also recommended is an iris immediately after the chip output. It can be tricky getting this iris placed correctly and close enough to the chip to not interfere with collimation optics, but a contraption with 90° optical adapters usually suffices to hold the iris. This iris can also be mounted to fine x/y/z translation stages to further fine tune the placement.

(Optional and recommended) After aligning the pump beam to the irises, insert a focusing lens and move the lens so that the focus is approximately at the center of the chip AND is centered on the irises.

Place a 500 nm longpass pump beam filter after the chip as close as possible. Next, sweep the chip temperature while monitoring the narrowband beam image immediately following the output of the chip. For this step, place a 10 nm bandpass filter centered at 810 nm onto the beam camera. Try to get the entangled photon emission roughly collinear with the pump beam by tuning the temperature, as this will make collimation easier in the future. Fine tune any chip parameters (goniometer tilt, x/y position) as well as the polarization of the pump beam to ensure that the resulting entangled photon image is balanced and visible on the camera.

Insert the collimation optic following the chip and pump filter. As of 06/2023, for the 401 nm entangled photon setup, we have found a short focal length off-axis parabolic (OAP) and long focal length cylindrical lens to be the best combination for collimating the entangled photon pairs. Alternatively, an OAP can be used. The OAP should be mounted atop a set of translation stages such that its x/y position relative to the chip can be adjusted. Coarsely move the OAP while monitoring the beam image with a beam camera such that the beam image remains roughly the same as the camera is moved down the table.

We have found that it is easiest to collimate the beam by referencing the image to a row of holes on the table. To accomplish this step, mount the long linear stage to the table and mount the beam camera to the stage such that the camera can be easily moved back and forth in a straight line. Checking the short and long range beam image, iterate the OAP x/y position and tip/tilt to get the entangled photon beam image straight and roughly the same size across a range that matches the Michelson interferometer path length. In this step, it is easiest to draw a box in the beam camera software to visually confirm that the beam is straight and collimated. For the 401 nm setup, the approximate path length is 30-50 cm. Additionally, for the 401 nm setup, try to get a beam image that has the same vertical dimension across the length. The divergence in the horizontal dimension can be corrected with a cylindrical lens. After collimating with the OAP, insert the cylindrical lens and move it until the beam image is at the same location on the camera. Again, it is helpful to draw a box in the beam camera software. Check that the beam is straight and remains the same size over the desired path length. You might have to remove the cylindrical

lens, repeat the OAP alignment, and then reinsert the cylindrical lens to achieve the best beam profile!

When the entangled photon beam is collimated and straight, align the interferometer:

- Set the linear stage that will be used for the time delay to approximately half its range, mount it to the table, and then mount a mirror to the stage.
- Dim the pump power such that you can still see the pump but that it is not too bright to look at on a card.
- Remove the pump beam filter following the chip and make sure that the pump beam is centered on the mirror mounted on the time delay stage. Move the mirror if this is not the case.
- Place an iris after the OAP/cylindrical lens such that the pump beam is centered on the iris.
- Adjust the tip/tilt of the mirror mounted to the stage so that the reflected beam is centered on the iris. For this step, it is helpful to use a slim card and move the edge in and out of the beam so that the incoming beam is not completely blocked. Also, we have found that the pump beam often displays ring-like diffraction patterns when it is reflected onto the iris. If this is the case, center the rings on the iris/incoming pump beam image.
- Insert a non-polarizing 50:50 beamsplitter after the iris, making sure that it is properly oriented to reflect and transmit the beam. For these experiments, the thin, dispersion-compensated beamsplitters from Layertec are preferable.
- Measure the distance between the beamsplitter and the front face of the mirror mounted on the linear stage. Mount a mirror in the reflected beam path at approximately this distance.
- Block the time delay arm of the interferometer and then adjust the tip/tilt of the non-time delay arm such that the beam is reflected onto the iris.
- Insert a beam camera following the beamsplitter. Replace the pump filter after the chip and raise the power such that the entangled photon image is visible on the camera.

- Block the non-time delay arm and ensure the beam stays in the same position as the stage is moved back and forth over a small range. Make minor adjustments to the stage mirror if this is not the case.
- Confirm that the time delay and non-time delay arms are overlapped on the beamsplitter. Draw a box in the beam camera software and block each arm to make sure the images are overlapped. **THIS IS CRUCIAL TO SEE INTERFERENCE!**
- Dim the pump power and remove the pump filter, then insert and align the coincidence counting setup. This setup consists of a second beamsplitter followed by 4 mirrors (2 mirrors in each arm) and then 2 free-space to fiber coupling units (1 in each arm). Note the overlap of the time delay and non-time delay arms by blocking each with a card. Align this portion of the beam into the fiber coupling units using the mirrors.
- Insert the pump filter and raise the pump power. Insert any narrowband/longpass filters to ensure that the SPADS don't get saturated. Connect the fiber coupling units to SPADs and maximize the fiber coupling efficiency by tuning the SPAD counts to maximum. This procedure is elaborated in the following section.
- Ensure the counts remain approximately the same as the stage is moved back and forth over a small range (10's of mm).
- Remeasure the distance between each mirror and the beamsplitter and set the stage position such that the two distances are approximately equal.
- Insert quarter-wave plate into the non-time delay arm and ensure that it is set to polarize the photons to 0° .
- Optimize coincidence to accidental ratio (CAR) and pump power that the peak is visible and (ideally) so the scan does not take too long. We have found that approx. 4×10^5 counts/s in each arm allows for 15 second integration time at each stage position.
- Start Matlab code and coarsely scan (step size of 0.005 mm) region of approximately 20 mm around the measured time zero. NOTE: classical Michelson interference can often be seen in the scan (see Fig. D.1). The entangled

Michelson interference can be delineated in that the counts in each arm also have the interference pattern.

- When time zero is found, finely scan the region around the time zero with a step size of 0.0001 mm.

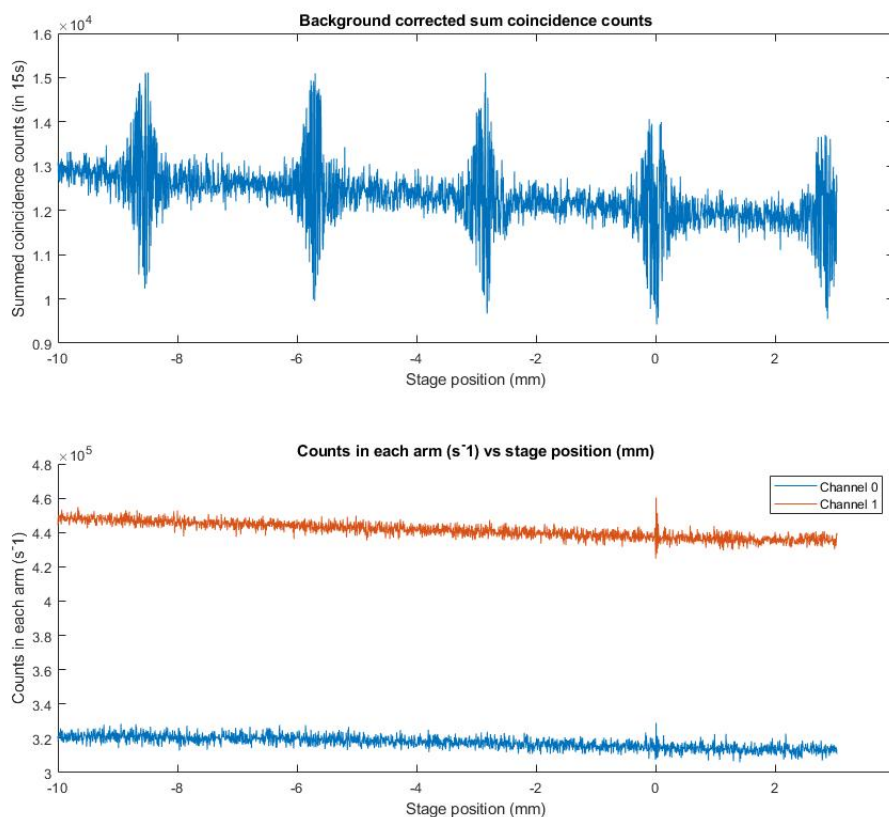


Figure D.1: Data from a coarse scan of the entangled two-photon Michelson interferometer. The top figure is summed and background corrected coincidence counts and shows the Michelson interference arising from the diode. The entangled interference can be distinguished by examining the counts in each arm vs stage position (bottom). From this data, time zero is near 0 mm.

D.1 Fiber coupling guide

Often, free space beams are coupled into fiber optics for ease of use and detection. The following guide highlights some alignment procedures that are helpful for maximizing fiber coupling.

The typical layout for fiber coupling consists of a two mirrors directing the free space beam into a fiber coupling unit. This fiber coupling unit consists of an aspheric lens mounted in an x/y mount that can move the position of the lens relative to the incoming beam. The asphere focuses the beam into a multimode fiber with a $105\ \mu\text{m}$ core that is mounted such that the z position of the tip can be moved relative to the beam. A recommended setup is the Thorlabs KM120 fiber launch system because the cage system inherently aligns several of these components.

If possible, first measure the free space optical power of the beam that needs to be fiber coupled. This will allow precise quantification of any losses.

For multimode fiber coupling follow this alignment procedure:

- Remove the asphere and fiber from the cage system.
- Using the two mirrors, align the beam to the fiber coupling cage system. Irises can be mounted onto the cage system to provide the near/far reference targets for this step.
- Mount the asphere and fiber holder onto the cage system and roughly position the fiber tip at the focus of the asphere as measured with a ruler.
- Monitoring the optical power (on a SPAD, power meter, etc.), tune the x/y position of the lens, z position of the fiber tip until maximum power is achieved.
- Iterate between tip/tilt of the two mirrors and the lens/fiber degrees of freedom until maximum power is achieved.

Multimode fibers are fairly straightforward to couple/align due to their large ($105\ \mu\text{m}$) core. However, single mode fibers are a bit trickier due to their much smaller cores, typically $5\ \mu\text{m}$. To align a single mode fiber, use a back-propagation alignment technique:

- Set up the the cage system with asphere and fiber and two mirrors.
- Ensure that two irises are placed in the optical path of the beam that you are trying to fiber couple.
- Attach the single mode fiber to some output source ie a fiber-coupled diode or a visual fault locator.

- Collimate the beam using the asphere/fiber degrees of freedom.
- Align the beam to the irises using a two-mirror alignment procedure.
- Connect the single mode fiber to the photodiode and further optimize for coupling efficiency.

INDEX

F

figures, 2, 9, 13, 15, 16, 18, 19, 41, 43–45, 47, 51, 54, 57, 67, 70, 71, 73, 74, 88,
89, 92, 93, 106–108, 111–116, 119–121, 124–129, 132–134, 140

T

tables, 49, 55, 90, 92, 131, 133